Andreas Mitterrutzner, BSc

Development and Validation of a Vehicle Model for Real Time Application on a Steer-by-Wire Prototype

Masterarbeit

Eingereicht an der

Technische Universität Graz

Fakultät für Elektrotechnik und Informationstechnik

Institut für Fahrzeugtechnik

Member of Frank Stronach Institute

Institutsvorstand:
Univ.-Prof. Dipl.-Ing. Dr.techn. Peter Fischer

Betreuer:
Dipl.-Ing. Andreas Hackl
Dipl.-Ing. Dr.techn. Cornelia Lex
Dipl.-Ing. Dr.techn. Jürgen Fabian

Betreuer ThyssenKrupp Presta AG:
Kristof Polmans

Graz, November 2015

Restricted access until November 2020

Danksagung

Diese Masterarbeit wurde zwischen Mai und Oktober 2015 in Kooperation mit dem Unternehmen ThyssenKrupp Presta AG erstellt. Für diese Chance und die Unterstützung möchte ich mich vor allem bei meinen Betreuern der TU Graz, Frau Dipl.-Ing. Dr.techn. Cornelia Lex, Herrn Dipl.-Ing. Andreas Hackl und Herrn Dipl.-Ing. Dr.techn. Jürgen Fabian bedanken.

Weiters möchte ich mich bei Kristof Polmans, Markus Dold und dem gesamten Steer-by-Wire Team bedanken, welche mir jederzeit für Fragen zur Verfügung standen.

Abschließend möchte ich mich bei meiner Familie, meinen Freunden und natürlich bei meiner Freundin für die Unterstützung bei meinem Studium in Graz bedanken.

Eidesstattliche Erklärung

Ich erkläre an Eides statt, dass ich die vorliegende Arbeit selbstständig verfasst, andere als die angegebenen Quellen/Hilfsmittel nicht benutzt, und die den benutzten Quellen wörtlich und inhaltlich entnommenen Stellen als solche kenntlich gemacht habe.

Graz, am ....
(Unterschrift)

I declare that I have authored this thesis independently, that I have not used other than the declared sources / resources, and that I have explicitly marked all material which has been quoted either literally or by content from the used sources.

....
(date) (signature)

Zusammenfassung

Diese Masterarbeit beschreibt die Entwicklung eines echtzeitfähigen Fahrzeugmodells für die Online-Simulation in einem Steer-by-Wire Prototypen. Der Modellansatz basiert auf einem linearen und nichtlinearen Einspurmodell. In dieser Masterarbeit werden die Herleitung der verschiedenen Modellgleichungen sowie der aufwändige Validierungsprozess beschrieben. Ziel der Arbeit ist, eine exakte Schätzung der fahrzeugspezifischen Werte für Gierrate und Querbeschleunigung in nicht-kritischen Fahrsituationen zu gewährleisten. Als Eingangsgrößen für das Modell werden der Lenkradwinkel und die Fahrzeuggeschwindigkeit verwendet. In kritischen Fahrsituationen wie Über- oder Untersteuern sollen die geschätzten Werte des Fahrzeugmodells von den real gemessenen Werten abweichen. Ein zusätzlicher Algorithmus soll gewährleisten, dass aufgrund der Abweichungen die kritische Fahrsituation erkannt wird. Diese Funktion zur Erkennung von kritischen Fahrsituationen wurde auf verschiedenen Fahrbahnoberflächen getestet und validiert. Zusätzlich zum Fahrzeugmodell werden Reifenmessungen durchgeführt, um daraus ein detailliertes Reifenmodell für das Testfahrzeug zu erstellen. Dieses Modell ist für die Erzielung eines guten Simulationsergebnisses notwendig. Durch verschiedene Fahrmanöver wird die korrekte Funktion des Fahrzeugmodells mit kombinierter Unter- und Übersteuerdetektion aufgezeigt. Das hier beschriebene Simulationsmodell bildet die Grundlage für die Entwicklung von weiteren Funktionen des Steer-by-Wire Fahrzeugs.

Abstract

This master thesis deals with the development of a real time vehicle model for online simulation in a steer-by-wire prototype. The approach is based on the linear and nonlinear single track model. The derivation of the different model equations is described as well as the validation process of the models. The goal of this thesis is to estimate the yaw rate and the lateral acceleration of the vehicle in non-critical driving situations. As input signals for the simulation the steering wheel angle and the vehicle velocity are used. For critical driving situations like under- and oversteering the model estimation and the real measured vehicle data should diverge. Therefore, an algorithm has to be implemented to detect the critical situation. This algorithm is validated in different driving situations on varying driving surfaces. Additional to the vehicle model, tire measurements were carried out for a tire model parametrization. The tire model is necessary for the vehicle model implementation. The accuracy of the different simulation models should be shown and the functionality of the under- and oversteering detection validated. This master thesis is the base for further function development of a steer-by-wire vehicle.

Contents

Danksagung iii

Eidesstattliche Erklärung v

Zusammenfassung vii

Abstract ix

Table of Contents xii

Symbols xiii

1 Introduction 1
- 1.1 ThyssenKrupp Presta AG . . . 1
- 1.2 Motviation . . . 1
- 1.3 Objective . . . 3
- 1.4 Test Vehicle . . . 4

2 Vehicle Model 5
- 2.1 Coordinate System . . . 5
- 2.2 Comparison of different Vehicle Models . . . 7
  - 2.2.1 Linear Single Track Model . . . 7
  - 2.2.2 Nonlinear Single Track Model . . . 7
  - 2.2.3 Two Track Model . . . 7
  - 2.2.4 Complex Multi-Body System . . . 8
  - 2.2.5 Finite Elements Model . . . 8
- 2.3 Linear Single Track Model . . . 8
  - 2.3.1 Derivation of model equations . . . 9
  - 2.3.2 Tire force . . . 11
  - 2.3.3 Calculation of the tire slip angle . . . 12
  - 2.3.4 Steady state cornering behavior . . . 16
  - 2.3.5 Stability analysis of the linear Single Track model . . . 19
- 2.4 Nonlinear Single Track Model . . . 21
  - 2.4.1 Driving limit due to adhesion . . . 22
- 2.5 Dynamic wheel load transfer . . . 22
  - 2.5.1 Simplified dynamic tire load model. . . . 22
- 2.6 Ackerman Steering Geometry . . . 26

2.7 Steering Geometry Measurement 27
2.8 Parameter Identification 31
2.9 Implementation environment 34

3 Tire Model 35
3.1 Tire Measurement testbench 35
3.2 Measurement Process 37
3.3 Tire data evaluation 40
3.3.1 Lateral tire force characteristic 41
3.3.2 Longitudinal tire force characteristic 52
3.4 Transient tire behavior 54
3.5 Tire Model selection 56
3.5.1 Magic-Formula Tire Model (Pacejka Tire Model) 56
3.5.2 Burckhardt Tire Model 59
3.5.3 TM-Simple Tire Model 59
3.6 Tire Model parametrization 63

4 Model Validation 67
4.1 Constant Radius 68
4.2 Sine input 69
4.3 Swept steer input 75
4.4 Step input 76
4.5 Conclusion 77

5 Understeering/Oversteering detection 79
5.1 Algorithm Structure 79
5.2 Algorithm validation 80

6 Conclusion and next steps 85

Bibliography V

Symbols

Parameters and Constants

m	Vehicle Mass	kg
Θ	Yaw Inertia	kgm^2
h_R	Height above Ground of CoG and roll center	m
l	Wheel base	m
l_{FA}	Distance from CoG to Front Axis	m
l_{RA}	Distance from CoG to Front Axis	m
s_{FA}	Track Width Front	m
s_{RA}	Track Width Rear	m
s	Track Width Average	m
g	Gravitational Constant	m/s^2
c_l	Aerodynamic Lift Coefficient	$-$
c_d	Aerodynamic Drag Coefficient	$-$
R	Corner Radius	m
c	lateral tire stiffness	N/rad

Variables

$\dot{\psi}$	Yaw Rate	rad/s
F	Force	N
α	Tire Slip Angle	rad
M	Moment	N
δ	Steering angle	rad
β	Body Slip Angle	rad
v	Effective Vehicle Speed	m/s
v_x	Longitudinal Speed	m/s
v_y	Lateral Speed	m/s
a_x	Longitudinal Acceleration	m/s^2
a_y	Lateral Acceleration	m/s^2

Vectors

$\boldsymbol{z}$	State Vector for Movement in Space
$\boldsymbol{a}$	State Vector for Acceleration in Space
$\boldsymbol{F}$	Force Vector
$\boldsymbol{x}$	State Vector

Matrix

$\boldsymbol{T}_{0V}$	Tranformation Matrix Inertial to Vehicle fixed Coordinate System
$\boldsymbol{T}_{WC}$	Tranformation Matrix W- to C- Tire fixed Coordinate System
$\boldsymbol{T}_{VT}$	Tranformation Matrix Vehicle fixed to Tire fixed Coordinate System
$\mathbf{A}$	System Matrix

Indices

x	x- direction
y	y- direction
z	z- direction
F	Front
R	Rear
FA	Front axis
RA	Rear axis
FL	Front left
FR	Front right
RL	Rear left
RR	Rear right
T	Tire-fixed Coordinate System
V	Vehicle-fixed Coordinate System
α	Tire Slip Angle
$stat$	Stationary

Abreviations

SbW	Steer-by-wire
TKP	ThyssenKrupp Presta AG
ABS	Antilock Braking System
TKP	Electronic Stability Program
CoG	Center of Gravity
FIR	Finit Impulse Response

1 Introduction

1.1 ThyssenKrupp Presta AG

ThyssenKrupp Presta AG (in the following TKP) is a company with headquarters located in Eschen in Liechtenstein. TKP is a subsidiary company of the ThyssenKrupp group and part of the business area ”Components Technology”. TKP is specialized in cold forging and builds steering systems for the automotive industry. In addition to complete systems, TKP sells system parts individually. Therefore, there is a part from TKP in nearly every newly produced passenger car [1]. TKP employs around 7000 people, of which around people are employed in Eschen, which is also the location of the main research and development department. TKP is a multinational company with 16 business locations distributed all over the world. Amongst others, there are business locations in France, USA and China. As part of the division ”Electric Power Assisted Steering Systems”, a team consisting of ten engineers and two mechanics form the ”Vehicle Dynamics and Testing” department. A team of three engineers of this department is currently involved in a research project to investigate steer-by-wire systems (SbW). In the course of this project, a prototype steer-by-wire system is to be developed and a prototype test vehicle is to be built up.

1.2 Motviation

When introducing steer-by-wire into a passenger car, the mechanical connection between the steering wheel and and steering gear is removed. Steer-by-wire systems therefore offer advantages, such as additional available space, system modularity and many more [18]. The steering input of the driver is measured with sensors and transmitted to a control unit. This control unit then actuates the steering gear. Therefore, it is no longer necessary to transmit the steering input of the driver directly to the wheels. Steer-by-wire introduces the road wheel angle as a possible control input. On the one hand, this simplifies the implementation of systems already commercially available such as automated parking or active lane keeping. There is no need for the steering wheel to rotate when the car performs maneuvers; therefore, the driver does not need to remove his hands. On the other hand, this offers the possibility to introduce new systems which actively suppress or correct safety critical steering inputs of the driver. This way, the driver can be supported while improving safety and performance. However, up to this point, steer-by-wire technology was not attractive for series production. The main reason for this lies within the legal requirements regarding fail safety of the system. The only realizable fallback solutions negate most of the advantages of the ideal steer-by-wire system and at the same time increase the cost as well. In recent years, the idea regained some attractiveness because autonomous driving became a target of many automotive companies. To realize autonomous driving, steer-by-wire is necessary. When introducing steer-by-wire, the last mechanical connection of the driver to the vehicle is removed. With this last step, vehicle dynamics can be fully controlled. On one side, an additional control input can increase performance of the controller. On the other side, certain control strategies are more effective in certain situations. One such scenario is μ-split braking. It describes a braking maneuver which is executed while driving with one side of the vehicle on normal asphalt and with the other side on ice. When braking is initialized, the vehicle will turn into the direction of the asphalt. That happens because the transmitted braking forces are higher on asphalt than on ice. As a result, the vehicle begins to yaw. In extreme cases, this can lead to instability of the vehicle. Anti-lock braking system (ABS) and and the electronic stability program (ESP), which are standard in modern vehicles, cannot prevent this effect satisfactorily [14]. Both systems act solely upon the brakes. ABS reduces brake pressure at each wheel to prevent the wheels from locking, thereby ensuring force transmission. ESP uses a wheel-individual braking input to stabilize yaw movement of the vehicle. Since all tires are operated with maximal force transmission, no additional brake force may be applied. To stabilize the vehicle nevertheless, ESP will reduce brake pressure on the wheels on asphalt, equalizing force transmission on both sides of the vehicle. As a result, braking performance is reduced to a similar behavior as the braking on a pure ice surface. In this scenario, a controller which acts on the road wheel angle in combination with the ESP breaking proves much more effective [9]. The controller can compensate the introduced yaw moment by an active countersteer. This strategy stabilizes the vehicle while, at the same time, improving braking performance. Additionally, a similar system can stabilize the vehicle during unstable cornering. Another aspect in the steer-by-wire technology is the feedback of the steering wheel given to the driver. The steering feel has to be generated with an additional power unit. To produce this steering feel, certain driving situations have to be detected properly. For normal driving situations, the steering feel can be generated depending from the vehicle velocity and the steering wheel angle. If the vehicle gets in a critical driving maneuver, like an understeering, the steering feel has to be adapted to give the driver the information of the situation. The implementation of the safety functions, as well as the feedback function of the steering wheel have one thing in common: the correct detection of the critical situation by the vehicle computing unit.

1.3 Objective

Objective of this master thesis is the development of a real time vehicle model, which estimates the different specific data of a vehicle, mostly the yaw rate and the lateral acceleration. Based on this estimation, a function has to be developed to detect critical situations like under- and oversteering. The principle of this detection should be a comparison of the measured and estimated yaw rate. If this data diverges too much, a critical situation can be supposed. Two different approaches are implemented and validated as simulation models: a linear and a nonlinear single track model. The simulation models have to be well validated for non critical driving situations with lateral accelerations lower than $5\,\mathrm{m/s^2}$.

Another part of this thesis is the development and implementation of a nonlinear tire model, which is required for a nonlinear single track model. For this tire model, tire measurements are done on a benchmark and evaluated afterwards. Different tire models have to be reviewed and evaluated.

Finally, the under- and oversteering detection has to be validated for different critical situations on varying driving surfaces.

1.4 Test Vehicle

The test vehicle for the steer-by-wire project is a Roding Roadster. The vehicle is depicted in figure 1.1. It is a two-seater with middle engine and rear wheel drive. The placing of the engine in the middle leads to the car trunk in the front. Therefore, a lot of space is available. This simplifies installation of the steer-by-wire steering gear and sensor equipment. The vehicle weights about 1250 kg and features a 6-cylinder engine producing 320 HP.

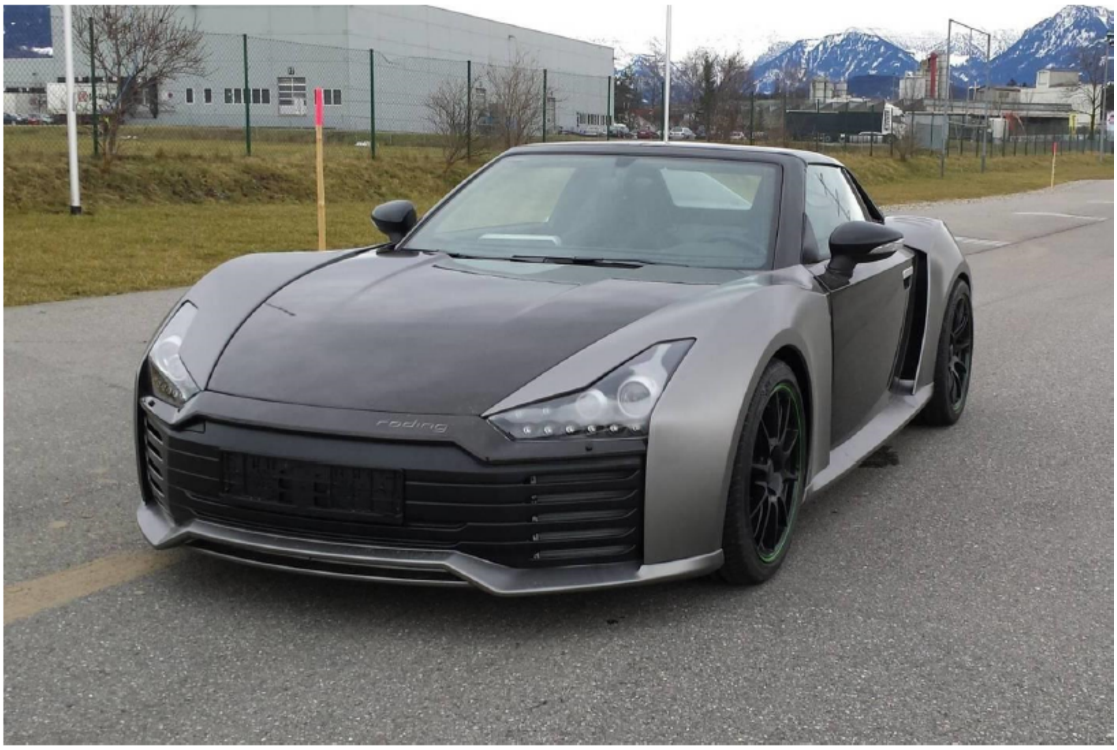

Figure 1.1: Roding Roadster prototype vehicle.

2 Vehicle Model

2.1 Coordinate System

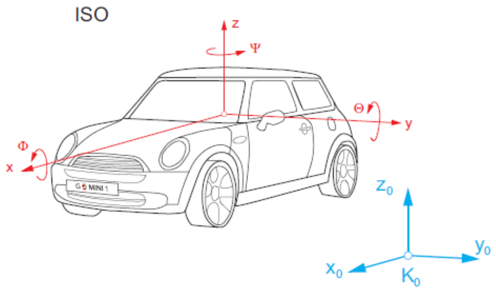

Figure 2.1: DIN 70000 coordinate system [13]

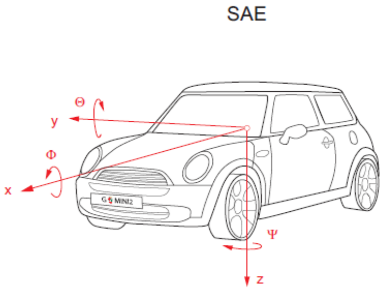

Figure 2.2: SAE J670e coordinate system [13]

In order to describe the vehicle movement in space, it is important to have a well defined coordinate system. Figure 2.1 and 2.2 show two normed coordinate systems. In this master thesis, the ISO DIN 70000 (figure 2.1) is used to describe the movement of the vehicle. This so called "vehicle fixed coordinate system" is placed in the center of gravity (CoG) of the vehicle. The orientation of the axis is shown in figure 2.1. The vehicle fixed coordinate system performs a movement relative to the inertial coordinate system with the yaw angle ψ. The orientation of the inertial coordinate system is shown in blue in figure 2.1. To transform kinematic and kinetic vectors from the vehicle fixed coordinate system into the inertial system, the transformation matrix $\boldsymbol{T}_{0V}$ from (2.1) is used:

$$ {}_0\begin{bmatrix} \dot{x} \\ \dot{y} \\ \dot{z} \end{bmatrix} = \underbrace{\begin{bmatrix} \cos\psi & -\sin\psi & 0 \\ \sin\psi & \cos\psi & 0 \\ 0 & 0 & 1 \end{bmatrix}_V}_{\boldsymbol{T}_{0V}} \begin{bmatrix} v_x \\ v_y \\ v_z \end{bmatrix} \tag{2.1} $$

v_x, v_y, v_z...velocity in x- y- and z- direction of vehicle fixed coordinate system
$\dot{x}, \dot{y}, \dot{z}$...velocity in x- y- and z- direction of inertial coordinate system

The tire fixed coordinate system of figure 2.3 is used to describe forces which act on the tire. The front tire rotates around the z-axis because of the steering angle δ. Therefore,

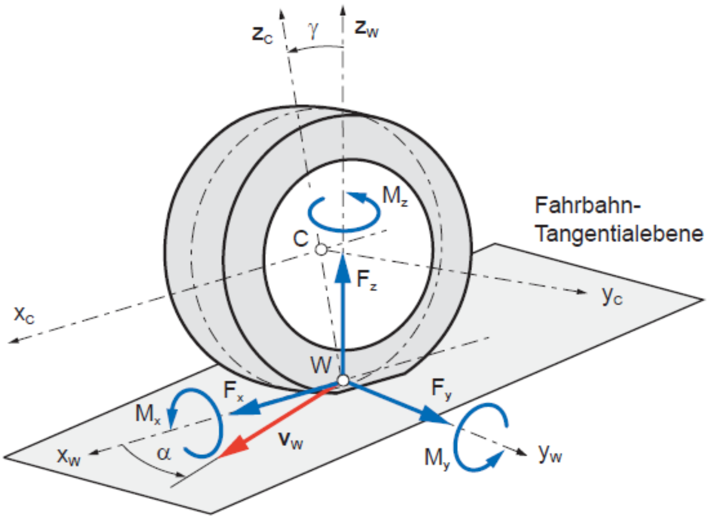

Figure 2.3: ISO 8855 tire fixed coordinate system [13]

the tire fixed coordinate system is introduced to make the description of the acting tire forces easier. To transform the vectors from the tire fixed coordinate system into the vehicle fixed system, the transformation matrix from (2.2) is used.

$$\boldsymbol{T}_{VT} = \begin{bmatrix} \cos\delta & -\sin\delta & 0 \\ \sin\delta & \cos\delta & 0 \\ 0 & 0 & 1 \end{bmatrix} \tag{2.2}$$

Another transformation of the tire forces has to be done, if the tire is mounted with camber γ. In this case the transformation from the W- to C- tire fixed coordinate system (figure 2.3) with the matrix T_{WC} of (2.3) and the equation (2.4) has to be done.

$$\boldsymbol{T}_{WC} = \begin{bmatrix} 1 & 0 & 0 \\ 0 & \cos\gamma & -\sin\gamma \\ 0 & \sin\gamma & \cos\gamma \end{bmatrix} \tag{2.3}$$

$${}_{W}\boldsymbol{F} = \boldsymbol{T}_{WC}^{T} \cdot \boldsymbol{F} + m_w \cdot g \cdot {}_{W}\boldsymbol{e}_z \tag{2.4}$$

m_W...wheel mass
g...gravitational constant
${}_{W}\boldsymbol{e}_z$...unit vector in z-direction of W- Tire fixed coordinate System

2.2 Comparison of different Vehicle Models

First of all, an evaluation of different possible vehicle model implementations has to be done. There are many possibilities to develop and implement vehicle models. Different descriptions of vehicle models from [5] follow now:

- Single Track Model, Linear
- Single Track Model, Nonlinear
- Two Track Model, Linear
- Complex Multi-Body System
- Finite Elements Model

2.2.1 Linear Single Track Model

In the linear single track model, the front and rear tires are summarized to one tire for each axle. Therefore, the degrees of freedom and the number of equations can be reduced. The linear single track model is developed out of the three main vehicle equations, which are simplified up to a certain point. These equations describe the main vehicle movement along the x- and y-axis and the rotation around the z-axis. With the linear single track model, you can describe the lateral dynamic of a vehicle up to a lateral acceleration between $4\,\mathrm{m/s^2}$ and $5\,\mathrm{m/s^2}$. A detailed description of the linear single track model follows in chapter 2.3.

2.2.2 Nonlinear Single Track Model

The main concept of the nonlinear single track model is based on the linear single track model, but the difference between these two models is the supposed tire behavior. In the linear single track model, the tire behavior is described as a linear equation between slip angle and lateral tire force. In the nonlinear single track model, the behavior between slip angle and tire force is described as a nonlinear tire model. To generate this tire model, tire force measurements from test benches are required. In comparison to the linear model, the nonlinear one has the advantage that the simulation result is accurate up to higher lateral accelerations in the range of $10\,\mathrm{m/s^2}$ and $11\,\mathrm{m/s^2}$. A detailed description of the linear single track model follows in chapter 2.4.

2.2.3 Two Track Model

In the two track model, every tire is described individually in all three dimensions of the tire fixed coordinate system. Therefore, the number of equations rises and the influence of tire load dynamic can be considered. The tire load dynamic has big influence at higher lateral accelerations, where the tire slip angle becomes higher than 3 degrees. Parts of the two track model, for example the tire load dynamic, can be extracted and used for the single track models. For a detailed description see to chapter 2.5.

2.2.4 Complex Multi-Body System

A multi body system can be used to describe a mechanical system consisting of different stiff bodys which are connected with bearings and pin-joints. Dependent on the number of bodies in the system, the degrees of freedom in the whole system rises up to a number higher than twenty. This increasing degrees of freedom results in the same high number of equations. Due to this fact, the simulation time increases, and the real time simulation requirement can not be guaranteed. The higher accuracy of the multi body system has fewer advantages than the higher simulation time generates problems.

2.2.5 Finite Elements Model

The finite elements model is mainly used to describe elastic and plastic deformations of bodies in a system. The model consists of different finite elements, whose possible deformations are restricted by the so called trial function. The finite element model results in a number of ordinary differential equations with a high number of freedom degrees. The calculation of this kind of models is generally done offline because of their high calculation time.

The main requirement for this model is to run in real time on an Autobox. Therefore, many of the described different modeling methods are not suitable. Another requirement is an accurate estimation of the vehicle yaw rate in the stable range of the vehicle. As the linear single track model has a simple structure and a good accuracy in the linear range of the vehicle, this kind of model is used to describe the lateral movement of the vehicle in his linear range. Another aspect of the linear vehicle model is that it can be easily extended with a nonlinear tire model and a dynamic tire load model. With this extensions, an accurate estimation of the vehicle yaw rate is possible up to higher levels of lateral accelerations. For the given application, a linear system is not accurate enough. Because of these aspects, this kind of model has been implemented. The model implementation and the results are described in following chapters.

2.3 Linear Single Track Model

The linear single track model, developed from Riekert and Schunk in 1940, is the simplest way to describe the lateral dynamic of a vehicle. It is the standard model to describe vehicle dynamics and is broadly used in specific literature as [5], [15] and [18]. The linear vehicle model holds up to lateral accelerations between 4-5 $\mathrm{m/s^2}$. The main advantages of the model are the intuitive structure and the close relation to physical properties of a vehicle. Adaption of the model to a different vehicle is easily done by adjusting the parameter set of physical properties. With the linear single track model, general statements about the vehicle's driving behavior can be made. Within the modeling, some simplifications has to be done:

- The velocity of the vehicle in the center of gravity is supposed to be constant into the direction of movement.
- Movements along the z-axis, as well as roll- and pitch movements, are neglected.
- The vehicle mass is assumed into the center of gravity.
- The front and rear tires have to be assumed to one tire for each axis.
- The pneumatic trail and the aligning torque have to be neglected.
- The tire load on front and rear axis have to be constant.
- The longitudinal tire forces, resulting out of the assumption of constant velocity, have to be neglected.

Because of the first two simplifications, the degrees of freedom reduce. The two remaining degrees of freedom are the yaw rate $\dot{\psi}$ and the slip angle β, depicted in figure 2.4. The yaw rate $\dot{\psi}$ is the rotation around the z-axis of the vehicle fixed coordinate system. The slip angle β describes the angle between the direction of the effective velocity of the vehicle in the center of gravity and the longitudinal vehicle axis. The input of the model is the angle of the rack input gear. Because of the steer-by-wire configuration of this vehicle, an angle sensor is placed there.

2.3.1 Derivation of model equations

In the following chapters, a detailed derivation of the differential equations of the single track vehicle model, called "bicycle model", is described based on the work of SCHRAMM, HILLER, BARDINI [5] and HIRSCHBERG [12]. All given vectors are related to the vehicle fixed coordinate system directed as shown in figure 2.4.

The vector $\boldsymbol{z}$ in (2.5) includes the three states with which the movement of the vehicle can be described. The states are the velocity in x- and y- direction (v_x and v_y) as well as the rotation around the z-axis ω_z.

$$\boldsymbol{z} = \begin{bmatrix} v_x \\ v_y \\ \omega_z \end{bmatrix} \tag{2.5}$$

The acceleration of the vehicle can be described with the following equation (2.6). It contains a term a_1, resulting out of the translatory movement of the vehicle and a term a_y, resulting out of the rotatory momentum arround the z-axis, which is also called centrifugal force.

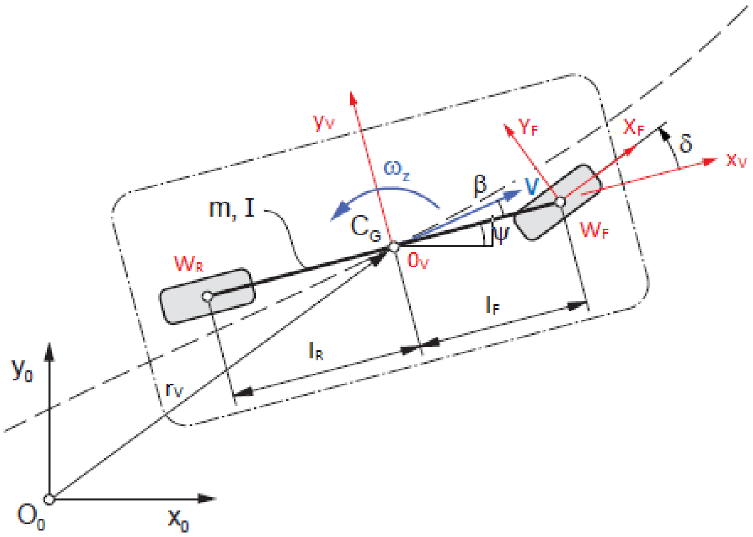

Figure 2.4: Figure with drawn vector orientation from [12]

$$\boldsymbol{a} = \dot{\boldsymbol{v}} + \boldsymbol{\omega} \times \boldsymbol{v} = \underbrace{\begin{bmatrix} \dot{v}_x \\ \dot{v}_y \\ 0 \end{bmatrix}}_{\boldsymbol{a_1}} + \underbrace{\begin{bmatrix} 0 \\ 0 \\ \omega_z \end{bmatrix} \times \begin{bmatrix} v_x \\ v_y \\ 0 \end{bmatrix}}_{\boldsymbol{a_y}} \tag{2.6}$$

$\boldsymbol{a_1}$ results out of the translatory vehicle movement.
$\boldsymbol{a_y}$ results out of the rotatory vehicle movement around the z-axis, which is also called centrifugal force.

For the first two rows of $\boldsymbol{a}$ you get the following equation (2.7):

$$\boldsymbol{a} = \dot{\boldsymbol{v}} + \boldsymbol{\omega} \times \boldsymbol{v} = \begin{bmatrix} \dot{v}_x - \omega_z v_y \\ \dot{v}_y + \omega_z v_x \end{bmatrix} \tag{2.7}$$

The angular velocity around the z-axis of the vehicle fixed coordinate system ω_z is equal to the first order derivation of the yaw angle ψ (2.8)

$$\omega_z = \dot{\psi} \tag{2.8}$$

For the angular acceleration it can be written(2.9):

$$\dot{\omega}_z = \ddot{\psi} \tag{2.9}$$

Out of the linear and angular momentum we get the following differential equations((2.10) and (2.11)) to describe the movement of the vehicle:

$$m\boldsymbol{a} = \boldsymbol{F} = \begin{bmatrix} F_{xF} + F_{xR} \\ F_{yF} + F_{yR} \end{bmatrix} \tag{2.10}$$

$$\Theta\dot{\psi} = F_{yF}l_F - F_{yR}l_R \tag{2.11}$$

Inserting (2.7) in (2.10) and (2.9) in (2.11), results in the following differential equation system (2.12):

$$\underbrace{\begin{bmatrix} m & 0 & 0 \\ 0 & m & 0 \\ 0 & 0 & \Theta \end{bmatrix}}_{\boldsymbol{M}} \underbrace{\begin{bmatrix} \dot{v}_x \\ \dot{v}_y \\ \dot{\omega}_z \end{bmatrix}}_{\dot{\boldsymbol{z}}(\boldsymbol{t})} = m \underbrace{\begin{bmatrix} \dot{\psi}v_y \\ -\dot{\psi}v_x \\ 0 \end{bmatrix}}_{\boldsymbol{k}(\boldsymbol{t})} + \underbrace{\begin{bmatrix} F_{xF} + F_{xR} \\ F_{yF} + F_{yR} \\ F_{yF}l_F - F_{yR}l_R \end{bmatrix}}_{\boldsymbol{q}(\boldsymbol{t})} \tag{2.12}$$

$\boldsymbol{M}$ ... 3×3 - mass matrix

$\dot{\boldsymbol{z}}$ ... 3×1 - general vector of acceleration

$\boldsymbol{k}$ ... 3×1 - vector of gyroscopic- and centrifugal forces

$\boldsymbol{q}$ ... 3×1 -vector of applied forces and moments. In this case, it consists of tire forces and their moments.

2.3.2 Tire force

The biggest influence on the model accuracy has the vector $q(t)$ from equation (2.12), which consists of the tire forces in x- and y- direction. As the main part of this master thesis is to generate a model which describes the lateral vehicle dynamic, the focus is directed towards the lateral tire forces. Also because the influence of the longitudinal tire force into the lateral vehicle dynamic is small compared to the influence of the lateral tire force.

The lateral tire force is a nonlinear dependency of the slip angle α. To identify this relation, complex tire measurements have to be done, as described in chapter 3.1. Furthermore, a more detailed description of the physical tire behavior is described in chapter 3.

A plot of a principle relation between the lateral tire force and the slip angle is depicted in figure 2.5. As it can be seen, the lateral tire force consists of a linear range and a saturation range. Under the precondition of small slip angles α, we can suppose a linear tire force characteristic. This assumption holds if the lateral accelerations are smaller than $4\,\mathrm{m/s^2}$ or $0.4\,\mathrm{g}$. Therefore, we can write for the lateral tire forces ((2.13) and (2.14)):

$$F_{yF} = -c_{\alpha_F}\alpha_F \tag{2.13}$$

$$F_{yR} = -c_{\alpha_R}\alpha_R \tag{2.14}$$

c_{α_F} and c_{α_R} of equation (2.13) and (2.14) are the slopes of the tire force characteristic curve at the linear area for slip angles less than about 3 deg.

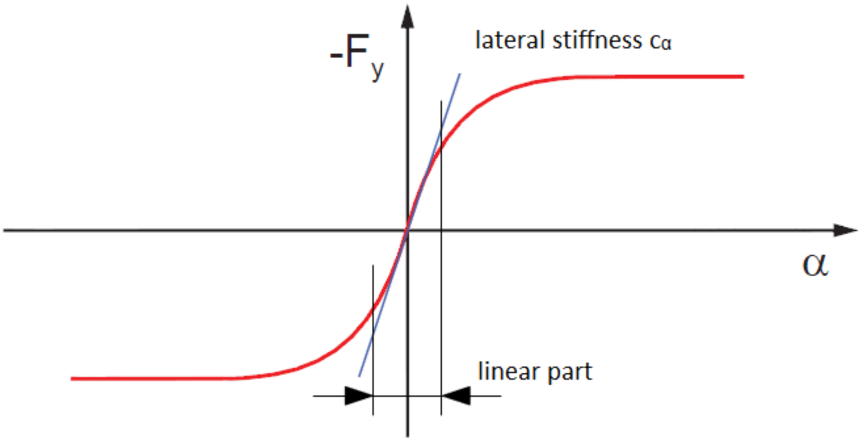

Figure 2.5: Schematic depiction of lateral tire characteristic from [12].

2.3.3 Calculation of the tire slip angle

The slip angle of the tires is defined within equation (2.15), where v_{yT} and v_{xT} are the tire velocity in the tire fixed coordinate system.

$$\alpha = \arctan(\frac{v_{yT}}{v_{xT}}) \tag{2.15}$$

Figure 2.6 shows the vectors for the definition of the slip angles.

For the rear tires, the tire fixed coordinate system has the same direction as the vehicle fixed coordinate system; therefore, no transformations have to be done. The velocity of the rear tires are calculated with the following equation (2.16).

$$\boldsymbol{v}_R = \boldsymbol{v} + \boldsymbol{\omega} \times \boldsymbol{r}_R = \begin{bmatrix} v_x \\ v_y \\ 0 \end{bmatrix} + \begin{bmatrix} 0 \\ 0 \\ \dot{\psi} \end{bmatrix} \times \begin{bmatrix} -l_R \\ 0 \\ 0 \end{bmatrix} = \begin{bmatrix} v_x \\ v_y - \dot{\psi} l_R \\ 0 \end{bmatrix} \tag{2.16}$$

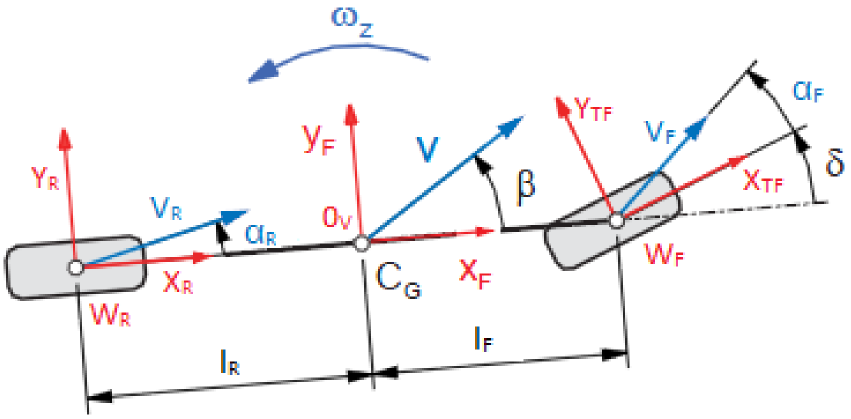

Figure 2.6: Vectors for the calculation of the front wheel force from [12].

The rear slip angle is defined as:

$$\alpha_R = \arctan(\frac{v_{yR}}{v_{xR}}). \tag{2.17}$$

Supposing that the slip angle remains small, it can be written:

$$\alpha_R = \frac{v_{yR}}{v_{xR}}. \tag{2.18}$$

. Entering (2.16) and (2.18) in (2.14) yields in:

$$F_{yR} = -c_{\alpha_R} \frac{v_y - \dot{\psi} l_R}{v_x}. \tag{2.19}$$

There is a difference between the calculation of the rear and front tire force because of the steering angle of the front tires.

The velocity of the front tires in body frame coordinates are given as:

$$\boldsymbol{v}_F = \boldsymbol{v} + \boldsymbol{\omega} \times \boldsymbol{r}_F = \begin{bmatrix} \dot{v}_x \\ \dot{v}_y \\ 0 \end{bmatrix} + \begin{bmatrix} 0 \\ 0 \\ \dot{\psi} \end{bmatrix} \times \begin{bmatrix} l_F \\ 0 \\ 0 \end{bmatrix} = \begin{bmatrix} v_x \\ v_y + \dot{\psi} l_F \\ 0 \end{bmatrix} \tag{2.20}$$

For the calculation the vectors of (2.20) have to be transformed into the tire frame coordinate system. The transformation matrix for this case is given as:

$$\boldsymbol{T} = \begin{bmatrix} \cos\delta & -\sin\delta & 0 \\ \sin\delta & \cos\delta & 0 \\ 0 & 0 & 1 \end{bmatrix}. \tag{2.21}$$

For small wheel angles less than 1 rad we can assume:

$$\boldsymbol{T} \approx \begin{bmatrix} 1 & -\delta & 0 \\ \delta & 1 & 0 \\ 0 & 0 & 1 \end{bmatrix}. \tag{2.22}$$

The tire velocity in tire frame coordinates is:

$${}_T\boldsymbol{v}_F = \boldsymbol{T}^T \boldsymbol{v}_F = \begin{bmatrix} 1 & \delta & 0 \\ -\delta & 1 & 0 \\ 0 & 0 & 1 \end{bmatrix} \begin{bmatrix} v_x \\ v_y + \dot{\psi} l_F \\ 0 \end{bmatrix} = \begin{bmatrix} v_x + \delta(v_y + \dot{\psi} l_F) \\ -\delta v_x + v_y + \dot{\psi} l_F \\ 0 \end{bmatrix} \tag{2.23}$$

The front slip angle is defined as:

$$\alpha_F = arctan(\frac{v_{yF}}{v_{xF}}). \tag{2.24}$$

Supposing that the slip angle remains small, we can write:

$$\alpha_F = \frac{v_{yF}}{v_{xF}}. \tag{2.25}$$

Entering (2.23) and (2.25) in (2.13) yields in:

$${}_T F_{yF} = -c_{\alpha_F} \frac{-\delta v_x + v_y + \dot{\psi} l_F}{v_x + \underbrace{\delta(v_y + \dot{\psi} l_F)}_{\ll v_x, insignificant}}. \tag{2.26}$$

For the back transformation of the front tire forces into the bodyframe coordinate system the following equations are used:

$$\boldsymbol{F_F} = \boldsymbol{T} \cdot {}_T\boldsymbol{F_F} = \begin{bmatrix} 1 & -\delta & 0 \\ \delta & 1 & 0 \\ 0 & 0 & 1 \end{bmatrix} \begin{bmatrix} F_{xF} \\ F_{yF} \\ F_{zF} \end{bmatrix} = \begin{bmatrix} F_{xF} - \delta F_{yF} \\ \delta F_{xF} + F_y F \\ F_{zF} \end{bmatrix} \tag{2.27}$$

$$F_{yF} = \underbrace{\delta F_{xF}}_{\ll F_{yF}} + {}_T F_{yF}. \tag{2.28}$$

The front tire forces yields in:

$${}_T F_{yF} = -c_{\alpha_F} \left(-\delta + \frac{v_y + \dot{\psi} l_F}{v_x} \right). \tag{2.29}$$

Entering the tire forces (2.19) and (2.29) in (2.12) yields in the following system of equations:

$$\begin{bmatrix} m\dot{v}_x \\ m\dot{v}_y \\ \Theta\ddot{\psi}_z \end{bmatrix} = m \begin{bmatrix} \dot{\psi} v_y \\ -\dot{\psi} v_x \\ 0 \end{bmatrix} + \begin{bmatrix} F_{xV} + F_{xH} \\ -c_{\alpha_F}\left(-\delta + \frac{v_y+\dot{\psi} l_F}{v_x}\right) - c_{\alpha_R}\frac{v_y-\dot{\psi} l_R}{v_x} \\ -c_{\alpha_F}\left(-\delta + \frac{v_y+\dot{\psi} l_F}{v_x}\right) l_F + c_{\alpha_R}\frac{v_y-\dot{\psi} l_R}{v_x} l_R \end{bmatrix}. \tag{2.30}$$

The lateral acceleration $\dot{v}_y$ can be written as follows:

$$\dot{v}_y = \frac{d(v\sin\beta)}{dt} = \dot{v}\sin\beta + v\cos\beta\dot{\beta}. \tag{2.31}$$

We assume that the slip angle β is smaller than 1 rad, so we can write $\cos\beta \approx 1$ and $\sin\beta \approx \beta$.

The slip angle β is also defined as follows:

$$\beta = \tan\frac{v_y}{v_x} \approx \frac{v_y}{v_x}. \tag{2.32}$$

For the longitudinal velocity v_x it can be written:

$$v_x = v\cos\beta \approx v. \tag{2.33}$$

Entering (2.31), (2.32) and (2.33) in row two and three of (2.30) yields in the following two equations:

$$mv\dot{\beta} = -m\dot{v}\beta - (mv^2 + c_{\alpha_F} l_F - c_{\alpha_R} l_R)\frac{\dot{\psi}}{v} - (c_{\alpha_F} + c_{\alpha_R})\beta + c_{\alpha_F}\delta \tag{2.34}$$

$$\Theta\ddot{\psi} = -(c_{\alpha_F} l_F^2 + c_{\alpha_R} l_R^2)\frac{\dot{\psi}}{v} - (c_{\alpha_F} l_F - c_{\alpha_R} l_R)\beta + c_{\alpha_F} l_F \delta. \tag{2.35}$$

Θ...vehicle inertia around the z-axis
l_F, l_R...distance from front and rear axle to the CoG

We assume that the vehicle is driving with constant speed v ($\dot{v} = 0$), so equation (2.34) and (2.35) simplifies as follows:

$$\dot{\beta} = \frac{1}{mv}[(-mv^2 - c_{\alpha_F} l_F + c_{\alpha_R} l_R)\frac{\dot{\psi}}{v} - (c_{\alpha_F} + c_{\alpha_R})\beta + c_{\alpha_F}\delta] \tag{2.36}$$

$$\ddot{\psi} = \frac{1}{\Theta}[-(c_{\alpha_F} l_F^2 + c_{\alpha_R} l_R^2)\frac{\dot{\psi}}{v} - (c_{\alpha_F} l_F - c_{\alpha_R} l_R)\beta + c_{\alpha_F} l_F \delta] \tag{2.37}$$

Equation (2.36) and (2.37) can be written as a state space model with the following state variables:

$$\boldsymbol{x} = \begin{bmatrix} x_1 \\ x_2 \end{bmatrix} = \begin{bmatrix} \dot{\psi} \\ \beta \end{bmatrix} \tag{2.38}$$

$$\underbrace{\begin{bmatrix} \dot{x}_1 \\ \dot{x}_2 \end{bmatrix}}_{\dot{\boldsymbol{x}}} = \underbrace{\begin{bmatrix} -\frac{1}{v}\frac{(c_{\alpha_F} l_F^2 + c_{\alpha_R} l_R^2)}{\Theta} & -\frac{c_{\alpha_F} l_F - c_{\alpha_R} l_R}{\Theta} \\ -1 - \frac{1}{v^2}\frac{c_{\alpha_F} l_F - c_{\alpha_R} l_R}{m} & -\frac{1}{v}\frac{c_{\alpha_F} + c_{\alpha_R}}{m} \end{bmatrix}}_{\boldsymbol{A}} \underbrace{\begin{bmatrix} x_1 \\ x_2 \end{bmatrix}}_{\boldsymbol{x}} + \underbrace{\begin{bmatrix} \frac{c_{\alpha_F} l_F}{\Theta} \\ \frac{1}{v}\frac{c_{\alpha_F}}{m} \end{bmatrix}}_{\boldsymbol{B}} \underbrace{\begin{bmatrix} \delta \end{bmatrix}}_{\boldsymbol{u}} . \tag{2.39}$$

The curve radius R of the road is defined as:

$$R = \frac{v}{(\dot{\psi} + \dot{\beta})}. \tag{2.40}$$

On the other hand, the centrifugal force a_y, which is orientated perpendicular to the curve U, is defined as follows:

$$a_y = \frac{v^2}{R}. \tag{2.41}$$

Entering equation (2.40) in (2.41) yields in the equation for the centrifugal force, which depends on the slip angle velocity $\dot{\beta}$, the yaw rate $\dot{\psi}$ and the velocity v.

$$a_y = v(\dot{\psi} + \dot{\beta}). \tag{2.42}$$

2.3.4 Steady state cornering behavior

To describe the steady state cornering behavior, the state space model (2.39) will be analyzed by its steady state equations. Therefore the left side of the state space model is set to zero:

$$\begin{bmatrix} 0 \\ 0 \end{bmatrix} = \begin{bmatrix} -\frac{1}{v}\frac{(c_{\alpha_F} l_V^2 + c_{\alpha_R} l_R^2)}{\Theta} & -\frac{c_{\alpha_F} l_F - c_{\alpha_R} l_R}{\Theta} \\ -1 - \frac{1}{v^2}\frac{c_{\alpha_F} l_F - c_{\alpha_R} l_R}{m} & -\frac{1}{v}\frac{c_{\alpha_F} + c_{\alpha_R}}{m} \end{bmatrix} \begin{bmatrix} x_1 \\ x_2 \end{bmatrix} + \begin{bmatrix} \frac{c_{\alpha_F} l_F}{\Theta} \\ \frac{1}{v}\frac{c_{\alpha_F}}{m} \end{bmatrix} \begin{bmatrix} \delta \end{bmatrix} . \tag{2.43}$$

For the stationary state variables, where $\dot{\psi}$ and $\dot{\beta}$ are set to zero, the following equations hold:

$$\dot{\psi}_{stat} = \frac{v}{l + \frac{l_R c_{\alpha_R} - l_F c_{\alpha_F}}{c_{\alpha_F} c_{\alpha_R}} \frac{m}{l} v^2} \delta_{stat} \tag{2.44}$$

$$\beta_{stat} = \frac{l_R}{R} + \frac{m l_F}{c_{\alpha_R} l} a_y. \tag{2.45}$$

With the equation (2.44) and the fact that for steady state behavior $\dot{\psi}_{stat}$ can be written as $\dot{\psi}_{stat} = a_y/v$, equation (2.46) can be extracted.

$$\delta = \underbrace{\frac{l_F + l_R}{R}}_{\approx \delta_A} + \underbrace{\frac{m}{l_F + l_R}\left(\frac{l_R}{c_{\alpha F}} - \frac{l_F}{c_{\alpha R}}\right)}_{=SG} a_y \tag{2.46}$$

In consideration of equation (2.46), a general statement of the steering angle requirement of the vehicle can be done. The term δ_A is the ackermann steering angle, as being described in chapter 2.6. The term SG is called the "self steering gradient" [5]. The self steering gradient is an indicator of the steering tendency of a vehicle. Dependent of the sign of the self steering gradient and of the lateral acceleration, a higher or lower steering angle has to be applied to keep on the track.

For a positive self steering gradient, the vehicle is understeering. If the self steering gradient is negative, the vehicle is oversteering. If the self steering gradient is equal to zero, the vehicle behavior is neutral. In general, vehicles are build to have an understeering behavior because of aspects of safety concerning the road traffic. A graphical representation of the under- and oversteering behavior of a vehicle is depicted in figure 2.7. For the characteristic velocity v_{ch} of the vehicle, the double steering angle has to be applied to stay in track. The critical velocity v_{cr} is a measure for the stability of an oversteering vehicle. In reference to real vehicles with nonlinear tire behavior, v_{ch} and v_{cr} are only target values. At the lateral acceleration, where these velocities are reached, the vehicle leaves his linear working area, and the linear vehicle model does not hold anymore.

The sign of the self steering gradient can be identified out of equation (2.46):

$c_{\alpha_R} l_R = c_{\alpha_F} l_F$ ... neutral
$c_{\alpha_R} l_R > c_{\alpha_F} l_F$ ... understeer
$c_{\alpha_R} l_R < c_{\alpha_F} l_F$ ... oversteer

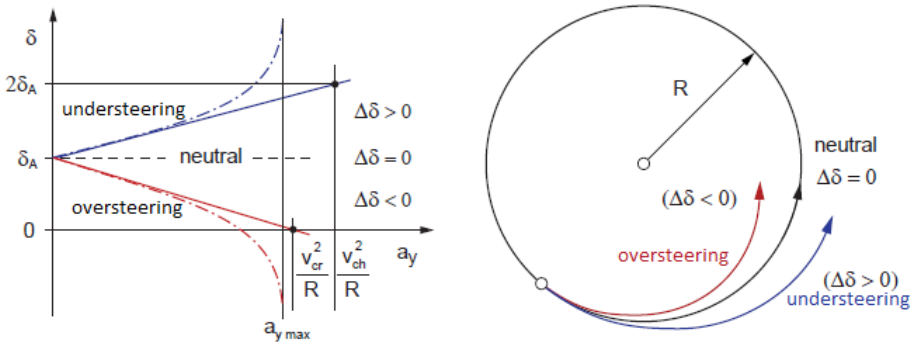

Figure 2.7: Graphical description of vehicle steering tendency from [12].

For the Roding Roadster the self steering gradient can be calculated with the following Parameters:

$m = 1376\,\mathrm{kg}$
$l_F = 1.46\,\mathrm{m}$
$l_R = 1.02\,\mathrm{m}$
$c_{\alpha_R} = 51\,967\,\mathrm{N/rad}$
$c_{\alpha_F} = 84\,629\,\mathrm{N/rad}$

$$SG = \frac{m}{l_F + l_R}\left(\frac{l_R}{c_{\alpha_F}} - \frac{l_F}{c_{\alpha_R}}\right) = 0.0014 \tag{2.47}$$

As it can be seen in equation (2.47), the vehicle has an understeering tendency in his linear range. The linear calculated wheel angle and the real required wheel angle for the Roding Roadster is depicted in figure 2.8. Up to a lateral acceleration of $5\,\mathrm{m/s^2}$, the wheel angle of the real car increases linear. After this point, the wheel angle increases nonlinearly.

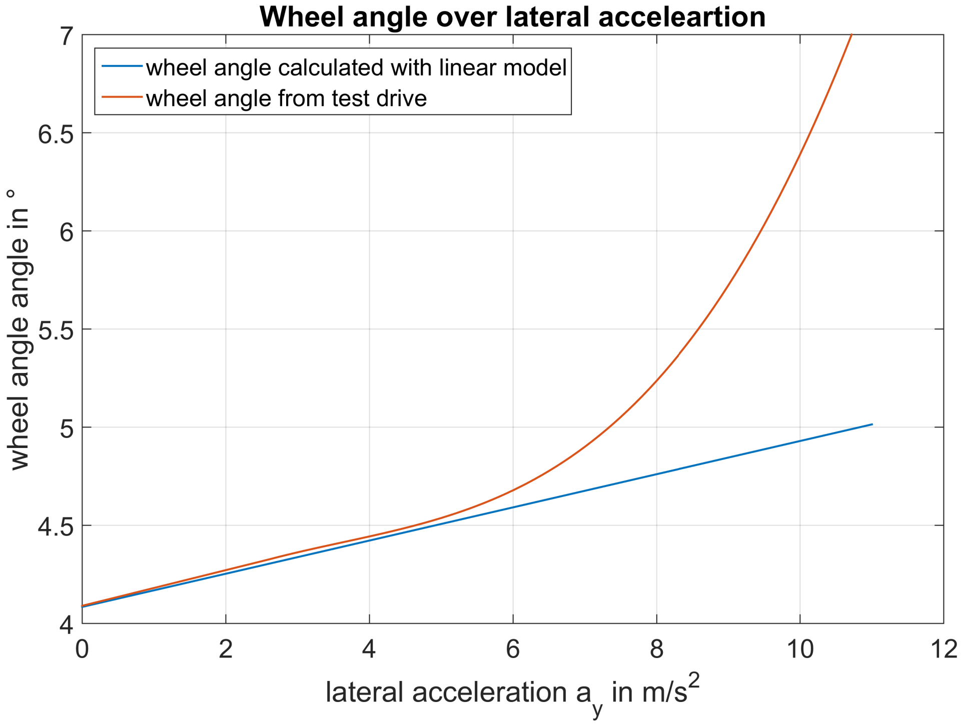

Figure 2.8: Calculated and measured wheel angle to lateral acceleration on a constant radius drive with a radius of 36 m.

Another characteristic vehicle cornering parameter is the yaw rate related to the wheel angle, which is called yaw gain. This parameter is only dependent from the velocity, not from the cornering radius. It describes how sensitive a vehicle reacts to steering wheel angle inputs. The yaw gain is described with the formula (2.48)

$$\frac{\dot{\psi}}{\delta} = \frac{v}{l + SG \cdot v^2} \tag{2.48}$$

As it can be seen in equation (2.48), the yaw gain is small for high (positive) self steering gradients, which holds for understeering vehicles like the Roding. For small (negative) self steering gradients of oversteering vehicles, the yaw gain is high, which means that the vehicle reacts very nervous to steering inputs. Another fact that can be seen in equation (2.48) is that the yaw gain becomes unstable for $v_{cr} = \sqrt{-\frac{l}{SG}}$. This formula has only a real solution for oversteering vehicles. For a more detailed description of the critical velocity v_{cr}, watch chapter 2.3.5.

For positive self steering gradients of understeering vehicles, a characteristic velocity v_{ch} can be calculated, at which the yaw gain reaches his maximum. The characteristic velocity is calculated with the following equation (2.49).

$$v_{ch}^2 = \frac{l}{SG} = \frac{l^2}{m}\left(\frac{c_{\alpha_R} c_{\alpha_F}}{l_R c_{\alpha_R} - l_F c_{\alpha_F}}\right) \tag{2.49}$$

For the Roding, the characteristic velocity lies about $v_{ch} = 42\,\mathrm{m/s}$. This value seems to be high in relation to general vehicles, but it is only a target value. The real value for the vehicle lies much lower because of the non-linearity of the vehicle for higher lateral accelerations.

2.3.5 Stability analysis of the linear Single Track model

Under the precondition of a straight ahead drive of the vehicle with constant speed, a stability analysis of the linear single track model can be done according to [5]. For the autonomous system without input ($\delta = 0$), the differential equation of (2.39) can be written as follows:

$$\underbrace{\begin{bmatrix} \dot{x}_1 \\ \dot{x}_2 \end{bmatrix}}_{\dot{\boldsymbol{x}}} = \underbrace{\begin{bmatrix} -\frac{1}{v}\frac{(c_{\alpha_F} l_F^2 + c_{\alpha_R} l_R^2)}{\Theta} & -\frac{c_{\alpha_F} l_F - c_{\alpha_R} l_R}{\Theta} \\ -1 - \frac{1}{v^2}\frac{c_{\alpha_F} l_F - c_{\alpha_R} l_R}{m} & -\frac{1}{v}\frac{c_{\alpha_F} + c_{\alpha_R}}{m} \end{bmatrix}}_{\boldsymbol{A}} \underbrace{\begin{bmatrix} x_1 \\ x_2 \end{bmatrix}}_{\boldsymbol{x}}. \tag{2.50}$$

For a stable system, the real parts of the eigenvalues of the system matrix $\boldsymbol{A}$ have to be negative. To determine the eigenvalues, equation (2.51) has to be solved.

$$det(s\boldsymbol{E} - \boldsymbol{A}) = 0 \tag{2.51}$$

This equation yields in the following characteristic polynomial of the system (2.52):

$$s^2 - \underbrace{(a_{11} + a_{22})}_{a_1} s + \underbrace{a_{11}a_{22} - a_{12}a_{21}}_{a_0} = 0. \tag{2.52}$$

According to the law of Hurwitz, for a polynomial with degree two, it is sufficient for stability if the constants a_0 and a_1 are strictly positive. The calculation of a_0 and a_1 yields in the following two equations (2.53) and (2.54):

$$a_0 = \frac{c_{\alpha_F} c_{\alpha_R} (l_F + l_R)^2 - mv^2 (c_{\alpha_F} l_F - c_{\alpha_R} l_R)}{m\Theta v^2} > 0 \tag{2.53}$$

$$a_1 = \frac{c_{\alpha F} + c_{\alpha R}}{mv} + \frac{c_{\alpha_F} l_V^2 + c_{\alpha_R} l_R^2}{\Theta v} > 0. \tag{2.54}$$

The equation (2.54) is always fulfilled because all parameters in it are positive. On the equation (2.53) has to be looked in more detail. Concerning this equation, between two cases must be differentiated:

1. The system is asymptotically stable for:

   $$c_{\alpha_F} l_F < c_{\alpha_R} l_R. \tag{2.55}$$

   Concerning figure 2.47 it means, that an understeering vehicle is always stable, even in its linear range.

2. The system is conditionally stable for:

   $$mv^2 (c_{\alpha_F} l_F - c_{\alpha_R} l_R) < c_{\alpha_F} c_{\alpha_R} (l_V + l_H)^2. \tag{2.56}$$

   As all parameters, beside the velocity v, are constant, the stability is only dependent of v. It exists a critical velocity v_{cr}, by which the system becomes unstable. The critical velocity is calculated with the following equation (2.57):

   $$v_{cr}^2 = \frac{c_{\alpha_F} c_{\alpha_R} (l_F + l_R)^2}{m(c_{\alpha_F} l_F - c_{\alpha_R} l_R)}. \tag{2.57}$$

   A critical velocity exists only for oversteering vehicles.

Since the Roding Roadster is an understeering designed vehicle, as shown in chapter (2.3.4), the linear vehicle model is stable for every velocity. But this fact does not mean that the real vehicle is stable for the whole velocity range too, because of the bounded validity of the linear model. For lateral accelerations higher than $4\,\mathrm{m/s^2}$, the stability has to be reviewed with a nonlinear vehicle model.

2.4 Nonlinear Single Track Model

The nonlinear single track model is used to describe the vehicle behavior up to a lateral acceleration of $10\,\mathrm{m/s^2}$. This is only possible if detailed information of the mounted tires are available. This tire data has been measured in a separate measurement process, described in chapter 3.

The general differential equations and assumptions for the nonlinear single track model are the same as for the linear single track model, described in chapter 2.3.

The following equations (2.58), (2.59) and (2.60) are the main equations for the nonlinear single track model, according to [15, pag. 60].

$$mv(\dot{\beta}+\dot{\psi})\sin\beta - m\dot{v}\cos\beta + F_{xR} + F_{xF}\cos\delta_F - F_{air,x} - F_{yF}\sin\delta_F = 0 \tag{2.58}$$

$$mv(\dot{\beta}+\dot{\psi})\cos\beta + m\dot{v}\sin\beta - F_{yR} - F_{air,y} - F_{xF}\sin\delta_F - F_{yF}\cos\delta_F = 0 \tag{2.59}$$

$$\Theta\ddot{\psi} - (F_{yF}\cos\delta_F + F_{xF}\sin\delta_F)l_F + M_{zF} + F_{yR}l_R - M_{zR} - F_{air,y}e_{SP} = 0 \tag{2.60}$$

The vehicle velocity is supposed to be constant; therefore $\dot{v}$ is equal to zero. Also the forces along the x-axis are assumed to be small in reference to the lateral forces. The air resistance is supposed to be small because of the aerodynamic design of the Roding. Also the tire aligning torque is supposed to be small. With these assumptions, the differential equation system can be reduced to the equations (2.61) and (2.62).
As mentioned, the biggest difference between the linear and nonlinear single track model is the expected tire behavior. Another difference to the linear vehicle model is, that wheel angles and slip angles are not supposed to be small anymore. Therefore, cosine, sine and tangent functions can not be simplified by their first order Taylor series expansion.

$$mv(\dot{\beta}+\dot{\psi})\cos\beta - F_{yR} - F_{yF}\cos\delta_F = 0 \tag{2.61}$$

$$\Theta\ddot{\psi} - F_{yF}\cos\delta_F l_F + F_{yR}l_R = 0 \tag{2.62}$$

2.4.1 Driving limit due to adhesion

As the nonlinear tire behavior of figure 3.9 and 3.10 shows, the maximal friction coefficient is at a slip angle of about $\alpha = 5°$. For higher slip angles, the friction coefficient decreases. Thus, if the slip angle gets higher than the maximum slip angle, the tire starts to glide to the lateral side. For the Roding, this adhesion limit lies at a lateral acceleration of about $13\,\mathrm{m/s^2}$, which corresponds to a maximum friction coefficient of $\mu_{max} = 1.3$, due to the following equations (2.63), (2.64) and (2.65).

$$\mu_{max} = \frac{\sum F_{y,max}}{F_z} \tag{2.63}$$

$$m \cdot a_{y,max} = \sum F_{y,max} \tag{2.64}$$

$$F_z = m \cdot g \tag{2.65}$$

2.5 Dynamic wheel load transfer

2.5.1 Simplified dynamic tire load model.

In the linear and nonlinear single track model, the center of gravity is supposed to be on the height of the road, and no roll or pitch movement can be considered. As this assumption holds for a long range of lateral acceleration, the error of the model prediction is low. In this case, one has to include that the Roding is a sports car, and therefore its center of gravity is lower than the one of general vehicles. For a single track model, without consideration of pitch and roll movements, the static wheel load is calculated as follows in equation 2.66 and 2.67. The second part of the equations is a result of the aerodynamic down force. As the Roding has no additional wings or spoilers, the aerodynamic lift coefficient $c_l A$ is assumed to be close to zero. Therefore, the aerodynamic part of the equations can be neglected.

$$F_{z,F} = \frac{l_R}{2l}\left(mg + \frac{1}{2}\rho c_l A v^2\right) \tag{2.66}$$

$$F_{z,R} = \frac{l_F}{2l}\left(mg + \frac{1}{2}\rho c_l A v^2\right) \tag{2.67}$$

For better accuracy at lateral accelerations higher than $6\,\mathrm{m/s^2}$, a dynamic tire load model is developed, according to [5]. With the dynamic tire load model, the dependency of the lateral tire force from the tire load, described in chapter 3, can be considered.

For an easier derivation of the dynamic wheel load shift, two virtual pivot bearings were introduced on the front and rear axis of the vehicle, shown in figure 2.9. The virtual pivot bearings are on the height of the roll center h_R. The following derivation of the dynamic wheel load shift is a simplified variation, as it does not consider eventual spring or damper force dynamics. Furthermore, the height of the CoG (h_{CoG}) and the roll center (h_R) are assumed to be equal. The front and rear wheel track are assumed to be equal (s_A). Based on the shown forces and moments in figure 2.9, the following equations from (2.68) to (2.74) can be written.

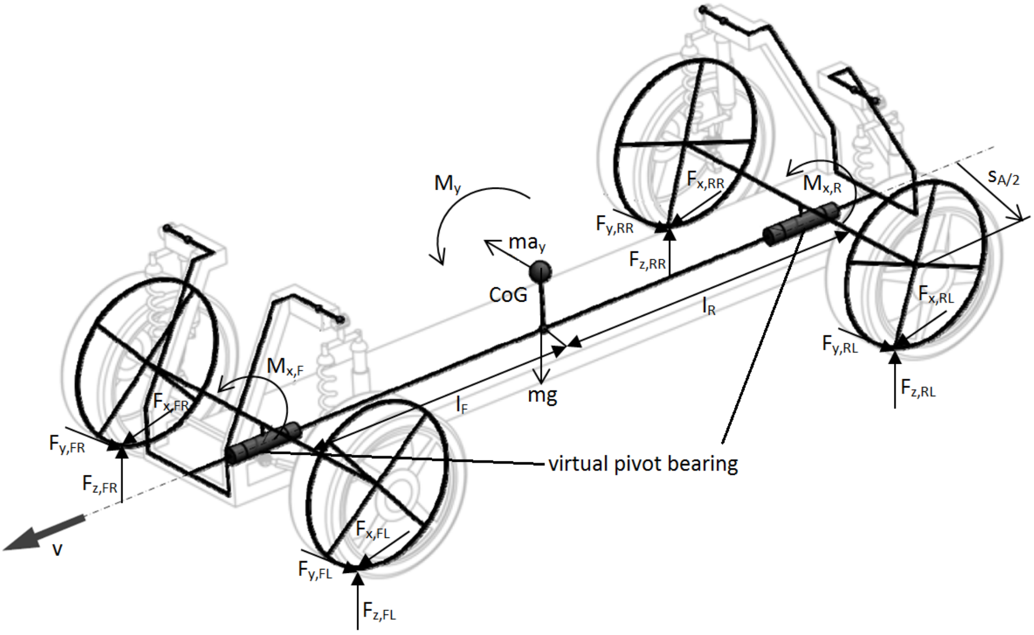

Figure 2.9: Linear roll model with forces and moments [5].

From the vertical force equilibrium the following equation (2.68) can be written:

$$mg = F_{z,FL} + F_{z,FR} + F_{z,RL} + F_{z,RR}. \tag{2.68}$$

From the moment around the y-axis the following equation (2.69) can be derived:

$$M_y = -h_R(F_{x,F} + F_{x,R}) - (F_{z,FL} + F_{z,FR})l_F + (F_{z,RL} + F_{z,RR})l_R. \tag{2.69}$$

From the moment around the x-axis of the virtual pivot bearing of the front axis, the following equation (2.70) is derived:

$$M_{x,F} = h_R(F_{y,FL} + F_{y,FR}) - \frac{s_A}{2}(F_{z,FL} - F_{z,FR}). \tag{2.70}$$

Equation (2.71) can be written from the moment around the x-axis of the virtual pivot bearing of the rear axis:

$$M_{x,R} = h_R(F_{y,FL} + F_{y,FR}) - \frac{s_A}{2}(F_{z,RL} - F_{z,RR}). \tag{2.71}$$

From the lateral force equilibrium on the front axis, the following equation (2.72) can be written:

$$F_{y,FL} + F_{y,FR} = \frac{l_R}{l} m a_y. \tag{2.72}$$

l...wheelbase

From the lateral force equilibrium on the rear axis, the following equation (2.73) is derived:

$$F_{y,RL} + F_{y,RR} = \frac{l_F}{l} m a_y. \tag{2.73}$$

From the longitudinal force equilibrium, yields in the following equation (2.74):

$$m a_x = F_{x,R} + F_{x,F}. \tag{2.74}$$

At equilibrium conditions ($M_{x,R} \equiv M_{x,F} \equiv M_y \overset{!}{=} 0$) the equations, can be solved for every F_z. This results in the equations for the "simplified dynamic tire load model".

$$F_{z,FL} = \frac{l_R}{2l} mg - \frac{l_R}{l}\frac{h_R}{s_A} a_y m - \frac{h_R}{2l} a_x m \tag{2.75}$$

$$F_{z,FR} = \frac{l_R}{2l} mg + \frac{l_R}{l}\frac{h_R}{s_A} a_y m - \frac{h_R}{2l} a_x m \tag{2.76}$$

$$F_{z,RL} = \frac{l_F}{2l} mg - \frac{l_F}{l}\frac{h_R}{s_A} a_y m + \frac{h_R}{2l} a_x m \tag{2.77}$$

$$F_{z,RR} = \frac{l_F}{2l} mg + \frac{l_F}{l}\frac{h_R}{s_A} a_y m + \frac{h_R}{2l} a_x m \tag{2.78}$$

In the simulation model, the dynamic and static tire load model was introduced to compare the results of the simulated yaw rate and lateral acceleration. To see a difference between the simulation result of the model with static and dynamic wheel load, a measurement maneuver with high lateral acceleration has to be done. Therefore, a slalom drive with a maximum lateral acceleration of $10\,\mathrm{m/s^2}$ was performed.

In figure 2.10, the measured yaw rate and lateral acceleration are compared to the model result with static and dynamic wheel load. As it can be seen, the difference becomes clear only at very high lateral accelerations. In the simulation with static wheel load, the vehicle seems to react faster to steering wheel angle changes. This fact is traceable because, when cornering with high lateral accelerations, the wheel load on the outer wheels of the curve is much higher than on the inner side. Due to the fact that the lateral tire force increases degressively in relation to an increasing wheel load, the vehicle reacts slower to steering wheel input changes. Another factor which is responsible for the slower reaction of the true vehicle is the slip angle of the front outer tire. In a curve, this one is smaller, than the one on the inner side because of the ackermann steering geometry, described in chapter 2.6. A smaller slip angle means a smaller lateral tire force and therefore slower yaw rate changes as well. In summary, it can be concluded, that the dynamic wheel load model leads into more accuracy of the simulation result. A clear difference to the result with static wheel load can only be seen at higher lateral accelerations.

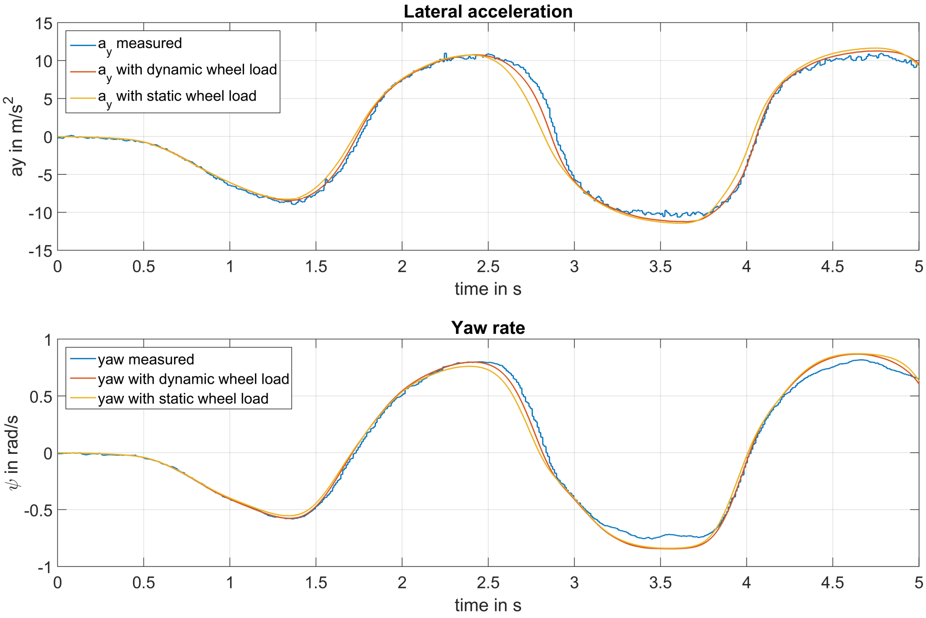

Figure 2.10: Comparison of lateral acceleration and yaw rate between simulation with and without dynamic wheel load model.

2.6 Ackerman Steering Geometry

Since the first development of motor driven vehicles, different mechanical steering constructions have been designed and tested. The most common steering geometry of actual vehicles is the so called ”Ackermann Steering”. This steering geometry follows out of the consideration that the inner and outer wheel of a vehicle at a certain cornering maneuver have to be orientated in a different angle. These angles are different because the outer wheel follows a larger circle than the inner, and the wheels have to be orientated tangentially to this circles [18]. This yields in the so called ”ackermann equations” (2.79):

$$\arctan \delta_{o,A} = \arctan \delta_{i,A} + \frac{j}{l} \tag{2.79}$$

$\delta_{o,A}, \delta_{i,A}$...ackermann wheel angles
l...wheelbase
$j = b_F - 2r_0$
b_F...track
r_0...offset steering

The parameters of the Ackermann steering are shown in figure 2.11. As it can be seen out of this figure, the front wheels are orientated tangentially to a radius, which has his center point in M. This ideal center point lies in axis to the rear tire. This assumption holds only for low cornering speeds or low lateral acceleration. For higher lateral acceleration, the point of center M moves toward the front axis.

The Ackermann steering geometry is a theoretical approach to the ideal movement of both tires at cornering. In reality, the Ackermann steering geometry is approximated and modified at certain working areas. At higher speeds where the steering angle is small, the dynamic wheel load shift has strong influence on the vehicle behavior. In this case, the outer wheel has applied a higher wheel load then the inner one. But according to the ackermann steering geometry, the outer slip angle is lower than the slip angle of the inner wheel, which means that less tire force can be brought up. Therefore, the steering geometry is designed properly to reduce the angle difference of inner and outer wheel at low steering angles. For racing vehicles it is common to design the steering to have a higher steering angle on the outer wheel for lower steering angles, to get a more dynamic behavior at cornering[7].

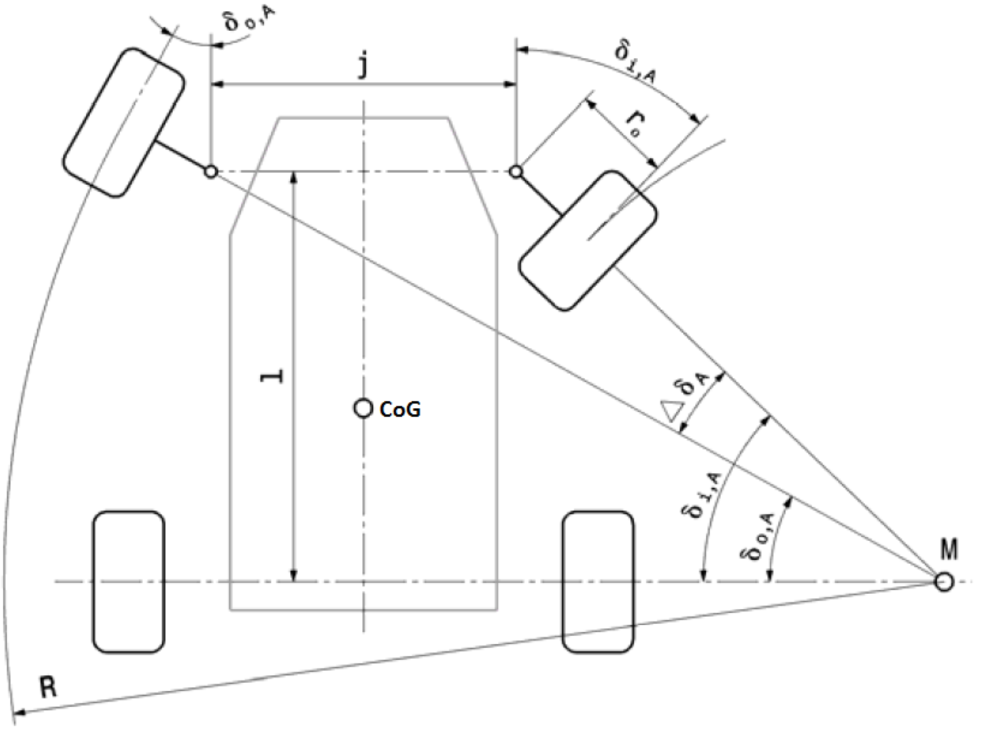

Figure 2.11: Depiction of Ackermann Steering geometry of [18].

2.7 Steering Geometry Measurement

The modeling of the steering system is an important part of the whole vehicle model, because it has strong influence on the simulation result. Therefore it is important to know the transmission between steering wheel angle and the wheel angle. Generally, you only have the angle position of the steering wheel as measurement data. As the steer-by-wire car has no direct mechanical connection between steering wheel and rack, it has an additional angle sensor, mounted on the input shaft of the rack. This second angle sensor is among others necessary for the feedback loop of the steering controller. All of this sensor signals are collected in the Autobox and can be used for further calculations and simulations. The angle of the input shaft can be used as input signal for the simulation of the vehicle model.

As the transmission between the rack angle and wheel angle δ is unknown, it has to be measured. To measure this transmission in an easy and accurate way, two string potentiometer are used. The position of the string potentiometer is shown in figure 2.12. The measurement strings were mounted at the wheel rims in a horizontal line with the center point of the wheel. To determine the wheel steering angle, equation (2.80) was derived, according to figure 2.12.

$$\delta = \arcsin\left(\frac{l_{Rght} - l_{Lft}}{d}\right) \tag{2.80}$$

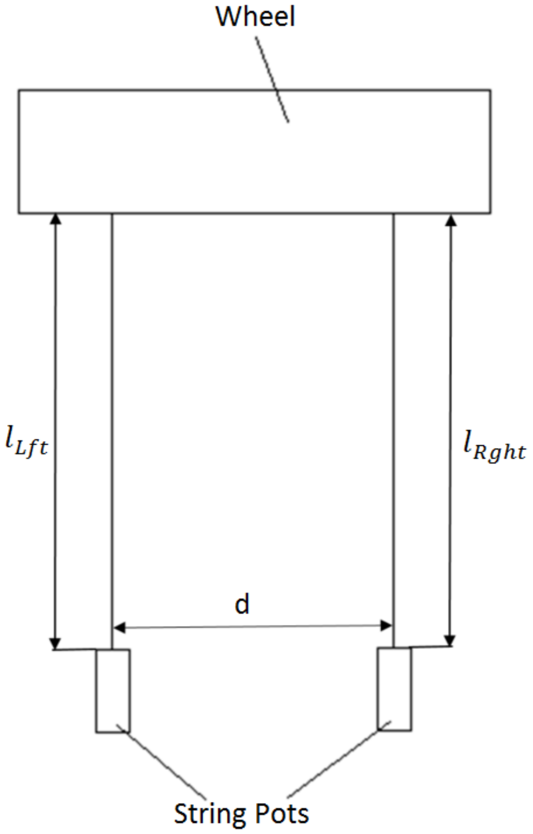

Figure 2.12: Figure of wheel angle measurement benchmark.

At a detailed view of equation (2.80), it becomes clear that the error of the calculated wheel angle becomes higher for higher steering angles because the strings of the string potentiometers are not parallel anymore. Another error is introduced by the skew and the steering radius of the steering axle. Therefore, the wheel is not rotating around the vertical axis of the contact point between wheel and road as it is assumed of the measurement. As the error is very small for lower wheel angle ($\delta < 15\,°$), the result is acceptable also because the higher wheel angle can also be reached at very low speeds, for example at parking. For this situation, a lower accuracy of the calculated wheel angle is acceptable.

In figure 2.13, the resulting wheel angle over the rack angle is plotted. The measurement was done for the left wheel, where a positive rack angle corresponds to a left cornering drive. As it can be seen of figure 2.13, for positive rack angles the wheel angle increases faster than for negative ones. This is an indication for a design close to the ackermann geometry.

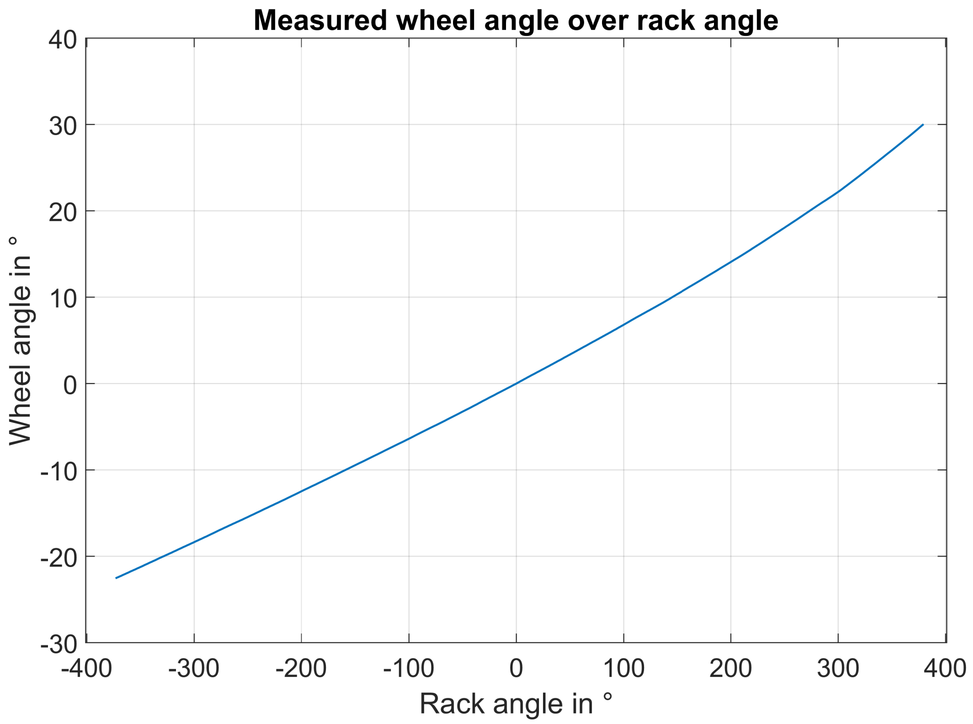

Figure 2.13: Measured wheel angle over Rack angle.

To compare the ideal ackermann geometry for this vehicle, with the real design the steering angle difference of the ideal Ackermann geometry and the real angle difference is calculated [18].

The ackermann angle was calculated according to equation (2.79) with the geometrical dimensions of table 2.1.

Parameter	Value	Unit
b_f	1.62	m
r_0	0.11	m
l	2.495	m

Table 2.1: Geometrical steering dimensions.

In figure 2.14, the ideal ackermann angle is depicted in contrast to the wheel angle of the inner wheel on cornering.

The equation for the calculation of the wheel angle difference is shown in equation (2.81) and equation (2.82).

$$\Delta\delta_F = \delta_i - \delta_o \tag{2.81}$$

$$\Delta\delta_A = \delta_{i,A} - \delta_{o,A} \tag{2.82}$$

δ_i, δ_o... inner and outer measured wheel angle
$\delta_{i,A}, \delta_{o,A}$...inner and outer ackerman wheel angle

As it can be seen, the real steering of the Roding is close to the ideal ackermann geometry. This means that the inner wheel at cornering is always applied with a higher wheel angle than the outer one. The measured wheel angle difference differs from the ideal ackermann steering only at higher wheel angles.

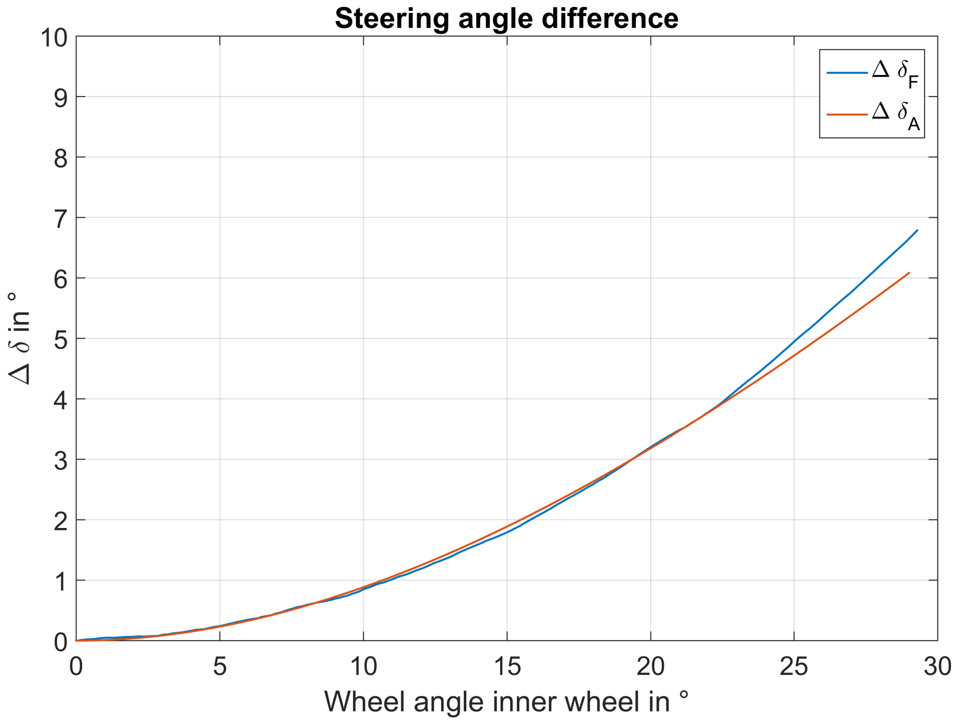

Figure 2.14: Steering difference angle.

For the vehicle model, the steering transmission was implemented as a look-up table with the values plotted in figure 2.13. This is a simple way to implement a steering model but accurate enough for this use case.

2.8 Parameter Identification

For a correct and accurate simulation of the vehicle model, a list of parameters has to be defined properly. As the vehicle is a mechanical system, most of the parameters can be measured in an easy way. A list of the known parameters is given in Table 2.2.

Parameter	Value	Unit
l_{FA}	1.4665	m
l_{RA}	1.0285	m
l	2.495	m
h_{CoG}	0.415	m
s_R	1.61	m
s_F	1.62	m
m	1259	kg

Table 2.2: Vehicle parameters.

The vehicle inertia around the z-axis J_z is a parameter which can only be measured with special measurement equipment. As this equipment was not available, an identification algorithm had to be introduced to identify it out of a measurement run. As equation (2.37) shows, the inertia has the biggest influence at the vehicle yaw rate. Therefore, the measured yaw rate was used as reference for the identification problem. As identification method, a greybox modeling method was used in matlab/Simulink. This method has the advantage that you can define known and unknown parameters of the model separately, and so you can solve an optimization problem in dependence of the unknown parameter. Another advantage is the minor effort of this identification method because of the possibility to use the model equations without any modifications. For the identification, the linear model equations for the vehicle model were used to reduce the optimization time. The identification could also be done with the nonlinear model equations. Matlab/Simulink provides efficient identification algorithms with which a fast solution is provided. As the linear vehicle model is valid up to a lateral acceleration of $5\,\mathrm{m/s^2}$, the identification is done with a slalom maneuver which doesn't exceed this value for lateral acceleration. As optimization method, the prediction error estimation algorithm was used. This kind of algorithm minimizes the error between measured and predicted output value. The cost function which is minimized is described in equation (2.83). The Parameter $e[n]$ is the error between measured and predicted model output.

$$J = \sum_{n=1}^{N} e^2[n] \tag{2.83}$$

Because of the simplifications of the linear model, a varying yaw inertia has to be expected for different reference driving maneuver. Another disadvantage of the use of the linear model system identification is that the vehicle velocity is supposed to be constant. If you want to take the vehicle speed as an input, the model becomes nonlinear and the identification becomes more complex.

To minimize the influence of measurement noise of the reference data, filtering has to be done. As forward filtering introduces a phase delay which influences the later inertia identification heavily, a special form of filtering has to be done. For the identification problem, the filtering can be done offline with the called forward-backward filtering. With this method, the signal gets filtered in the forward direction, then the filtered sequence gets reversed and filtered again with the same filter. Thanks to this method, no phase delay is introduced to the signal. The final transfer function corresponds to the squared magnitude of the original filter. An example for the raw yaw rate signal and the filtred signal is shown in figure 2.15.

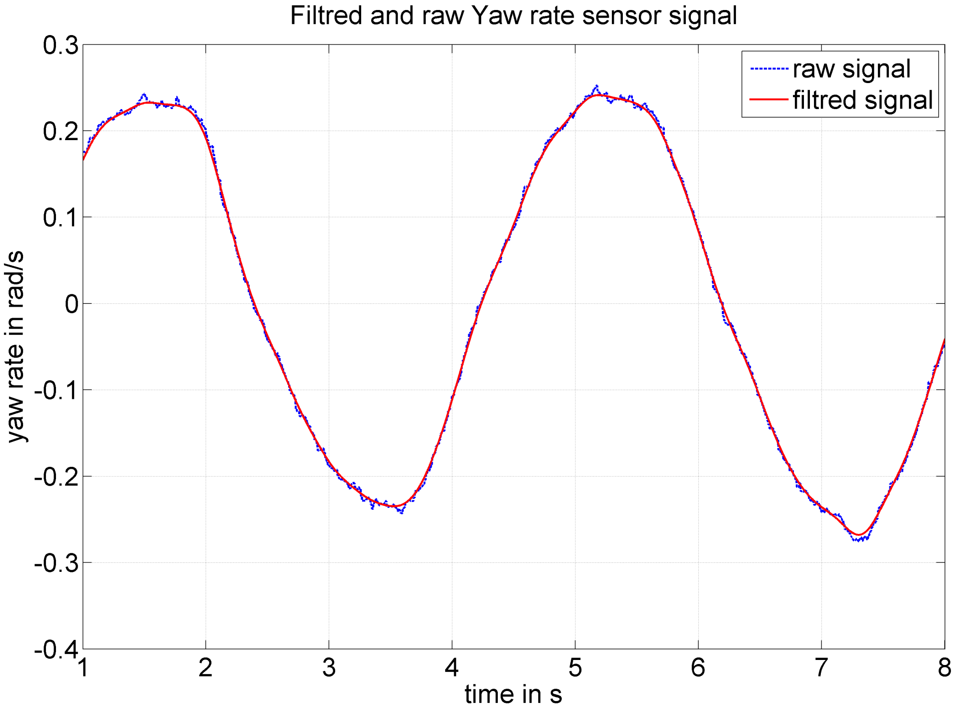

Figure 2.15: Filtred and raw sensor signal of yaw rate sensor.

The identification was done with different slalom maneuvers at different vehicle speeds. Out of this set, a certain inertia that fits best within other driving maneuvers has to be selected. The received parameter sets are listed in Table 2.3.

A possible way to assess the yaw inertia of a vehicle is the use of formula (2.84) with data from [8], where c is a parameter which depends on the form of the vehicle.

v	J_z	f	$a_{y,max}$
m/s^2	kgm^2	Hz	m/s^2
50	2099	0.3	7
60	1737	0.3	7
70	1685	0.26	5

Table 2.3: Identified yaw inertia for different velocities.

$$J_z = cm\frac{l^2}{2},\ \mathrm{c} = \mathrm{const} \in [0.6, ..., 1] \tag{2.84}$$

For the in the model used yaw inertia of the Roding, the mean value of the different identified values of table 2.3 was calculated. The resulting value for the inertia is $J = 1840\,\mathrm{kgm}^2$. The simulation of the whole vehicle model was done with the different identified yaw inertia, and it turned out that the calculated mean value suits best with this model. It is also in the nearest range of the values from equation (2.84).

As it can be seen in table 2.3, the frequency of the performed sinus maneuver is low with $f = 0.3\,\mathrm{Hz}$. This low frequency has the aim to minimize the influence of transient tire behavior of the vehicle. As the inertia has the biggest influence on the phase shift of the yaw signal, which is also influenced by the transient tire behavior, a proper maneuver has to be done. As the time constant of the transient tire behavior is in a range of $10 - 30\,\mathrm{ms}$, the influence at lower yaw rate frequencies is low in relation of the influence of a varying yaw inertia.

Due to the different identification results for the yaw inertia it is a challenge to get a correct parameter set. The identification result is always affected by irregularities, and the risk is high to generate an over trained model, which means that the simulation result fits well with the reference simulation data, but the accuracy is low for other simulation data. The decision for the final used value has been made on the base of the average value of the estimated parameters also because the result of (2.84) was close.

2.9 Implementation environment

The Roding Roadster is build up as a prototype for a steer-by-wire vehicle. For the realization of the steer by wire system, lots of additional sensors and an additional computing unit has to installed. This additional processing unit is a so called "dSpace Autobox", a rapid prototyping hardware. The Autobox is a modular device which consists of the powerful processing unit $DS1005$ and is extended with a Flexray and Can interface as well as a multi channel I/O board [6]. Additionally, two incremental encoder for the installed angle sensors are integrated. All sensors and bus data converge at the Autobox and get processed there.

The main advantage of the dSpace Autobox is the compatibility with Matlab/Simulink. Due to this, the whole steer by wire software is implemented as a Simulink model. Therefore, also the vehicle model developed in this master thesis is implemented as a Simulink model, which reduces the simulation effort a lot. For the real time simulation on the Autobox, the vehicle model gets integrated in the steer by wire model and compiled to C-Code. The final software gets loaded on the Autobox in the vehicle and can be executed immediately. The high level compatibility of Matlab/Simulink and Autobox reduces the implementation effort and provides useful features for the real time simulation.

Once loaded the software on the Autobox, the dSpace software on an external Computer can be used to stream and record signals. Different dSpace layouts can be configured to modify simulation Parameters in real time, without any rework on the Simulink model. The provided functions of the dSpace software is also a useful instrument for a rapid prototyping.

Due to the previous described advantages of the dSpace Autobox in combination with Matlab/Simulink, the main focus of this master thesis can be directed on the model development and simulation because the software implementation is less time consuming. Also the input signal conditioning of the sensor signals, which generally is labor intensive, is already done. Nevertheless, to guarantee the real time capability, it has to be kept in mind not to build up the model in a too complex way. This has to be done because the sampling frequency of the Autobox is set to $F_s = 1\,\text{kHz}$. This sampling rate is necessary to guarantee the stability of the rack position controller and can not be reduced in this development phase.

The angles of the steering wheel and rack input shaft are measured with different angle sensor implementations, like a relative and absolute angle sensor, to have a redundant measurement system. To measure the vehicle velocity in an accurate way, an optical velocity sensor is mounted on the assistant driver door. For the measurement of the accelerations in all three axis of the coordinate system and the rotation around this axis, a Racelogic measurement box is mounted in the center of gravity of the vehicle. The high level sensor system integrated in the Roding is the base for a good simulation result.

3 Tire Model

The main part of a well working vehicle model is a correct tire model of the mounted tires. Getting measurement data of a certain tire is very difficult and expensive. Therefore, a proper tire measurement has to be done on a tire measurement testbench. Out of the measurement data, a tire model has to be selected and optimized. In the following chapter, the tire measurement and model generation for the tires mounted on the Roding Roadster is described.

3.1 Tire Measurement testbench

To gain tire measurement data which describe the dependence of the lateral and longitudinal tire force of the vertical wheel load, complex measurement testbenches have to be build up. In general, two different concepts for testbenches exist [20]:

- fixed measurement testbench
- mobile measurement testbench

The fixed tire measurement testbench consists of a drum roll or flat track, whereon the measurement tire is moved. The biggest advantage of a fixed tire testbench is the accurate reproducibility of the different measurement cycles. A disadvantage is the lack of possibility to generate a real road surface, which you get only on the general road.

The tire measurements of the Roding Roadster where done with a mobile measurement testbench in cooperation with the University of Applied Science Biel. The so called "Mobile Tire Testing Laboratory" is depicted in figure 3.1.

The university has build up the mobile tire measurement truck step by step within student projects. The base of the truck is a Mercedes Benz Actros 1853 with a weight of 14 tons. Tires for measurement can be mounted on the truck on the left and right side, so you can measure two tires at one run. Four piezo force sensors in one wheel hub measure the forces in x-, y- and z- direction as well as the moments around this axis. With the measurement truck, the lateral and the longitudinal tire force characteristics can be determined. A hydraulic motor is built in as a secondary power unit for the acceleration and deceleration of the wheel.

To get a clean zero crossing of the measurement data, the measurement wheel has always been moved in the opposite direction at the beginning of the measurement; e.g. if the

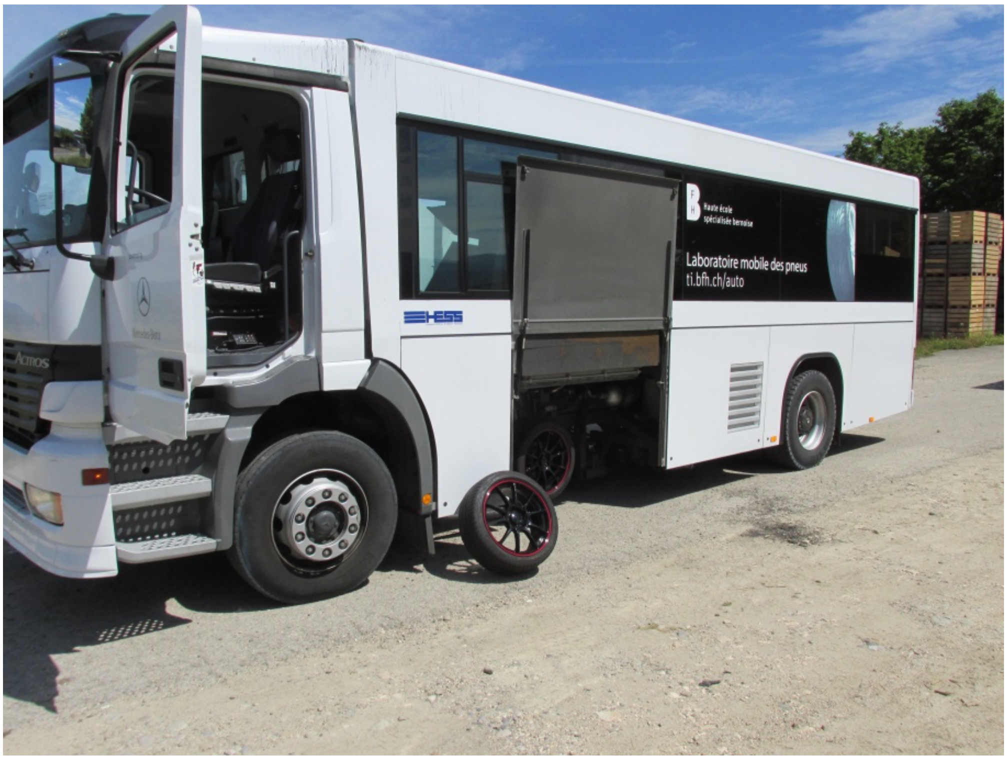
Haute école spécialisée bernoise
Laboratoire mobile des pneus
ti.bfh.ch/auto
HESS

Figure 3.1: Mobile Tire Testing Laboratory

braking slip is measured, the measurement wheel is first accelerated at a speed higher than the vehicle speed and braked down afterwards.

The wheel load can be changed continuously from 0 kN to 5 kN with the hydro-pneumatic adjustable suspension of the measurement wheels. A big disadvantage of the measurement truck is that the wheel load is not controlled. This means that the wheel load is set to the desired value when the truck stands still. During the running of the measurement, the wheel load is not adjusted anymore; therefore, the wheel load changes in a range between ±10 % of the initial set value. This happens for example at roll movements of the whole truck or because of the unevenness of the road. This fact introduces a lot of inaccuracy, described in the following chapters.

The measurement truck is also able to wet the road with water to simulate low friction between road and tire. Therefor a water pipe and a water tank with a volume of 2000 l is mounted. A detailed view at the measurement testbench is depicted in figure 3.2.

On the Roding Roadster, the following tires are mounted:

- Front tire: Michelin $225/40ZR18$
- Rear tire: Michelin $265/35ZR18$

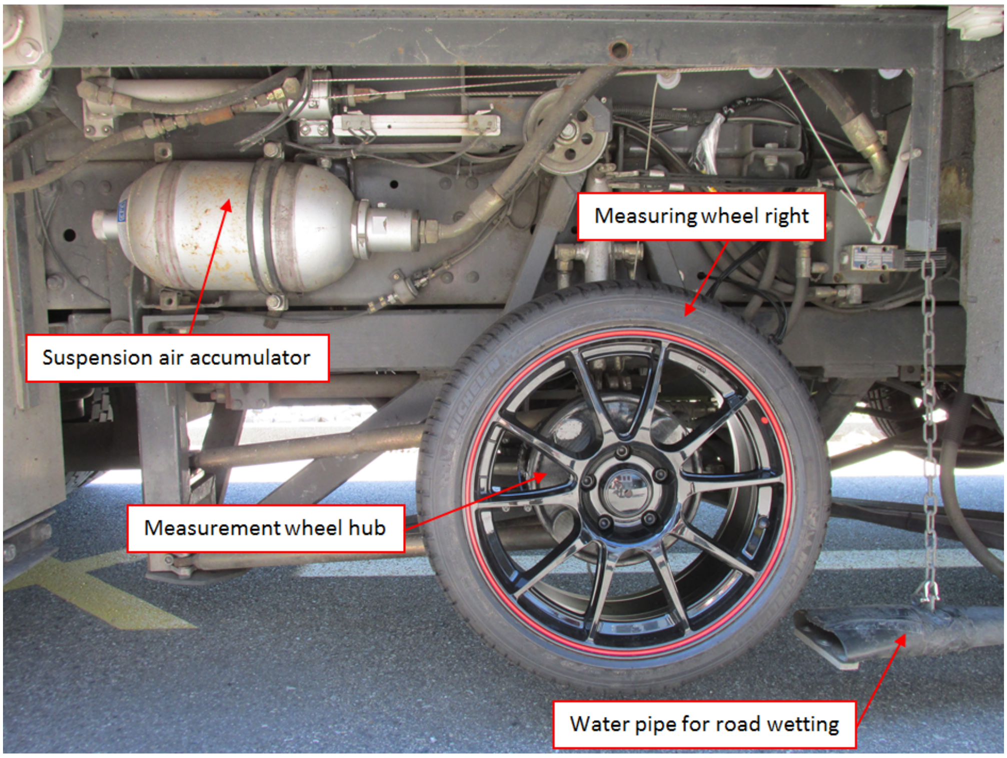

Figure 3.2: Detailed view of the mobile measurement testbench with descriptions

3.2 Measurement Process

The tire measurement truck has a license to drive on public roads; therefore, the measurements were done on a long straight road section. The advantage of this is that you can do a series of $15-20$ measurements at one drive. If you want to do this high number of measurements on a test track of the University of Biel, you need much more time because they do not have such a long straight road section. The disadvantage of the measurements on the public road is the unevenness of the road, which introduces measurement noise.

First of all, a measurement plan has to be prepared. The most important part of the measurement is the selection of the right wheel load forces for the tires. To generate a tire model afterwards, a measurement with the stationary wheel load for every wheel of the Roding has to be done at least. To consider the variation of the wheel load in the tire model, a second measurement on the double stationary wheel load is necessary. To have a third measurement set for the validation of the model, a measurement on the half stationary wheel load should also be done.

To estimate the maximal possible wheel load, due to the dynamic wheel load transfer, the equations (2.75), (2.76), (2.77) and (2.78) can be evaluated for the maximum possible lateral and longitudinal acceleration. The equations with the geometrical dimensions of the vehicle yield in the following equations (3.1) to (3.4).

$$F_{z,FL} = \frac{1.0285\,\mathrm{m}}{2\cdot 2.495\,\mathrm{m}} mg - \frac{1.0285\,\mathrm{m}}{2.495\,\mathrm{m}} \frac{0.415\,\mathrm{m}}{1.62\,\mathrm{m}} a_y m - \frac{0.415\,\mathrm{m}}{2\cdot 2.495\,\mathrm{m}} a_x m \tag{3.1}$$

$$F_{z,FR} = \frac{1.0285\,\mathrm{m}}{2\cdot 2.495\,\mathrm{m}} mg + \frac{1.0285\,\mathrm{m}}{2.495\,\mathrm{m}} \frac{0.415\,\mathrm{m}}{1.62\,\mathrm{m}} a_y m - \frac{0.415\,\mathrm{m}}{2\cdot 2.495\,\mathrm{m}} a_x m \tag{3.2}$$

$$F_{z,RL} = \frac{1.4655\,\mathrm{m}}{2\cdot 2.495\,\mathrm{m}} mg - \frac{1.4655\,\mathrm{m}}{2.495\,\mathrm{m}} \frac{0.415\,\mathrm{m}}{1.62\,\mathrm{m}} a_y m + \frac{0.415\,\mathrm{m}}{2\cdot 2.495\,\mathrm{m}} a_x m \tag{3.3}$$

$$F_{z,RR} = \frac{1.4655\,\mathrm{m}}{2\cdot 2.495\,\mathrm{m}} mg + \frac{1.4655\,\mathrm{m}}{2.495\,\mathrm{m}} \frac{0.415\,\mathrm{m}}{1.62\,\mathrm{m}} a_y m + \frac{0.415\,\mathrm{m}}{2\cdot 2.495\,\mathrm{m}} a_x m \tag{3.4}$$

With the maximal lateral and longitudinal acceleration, the following values for the maximal and minimal wheel load can be calculated.

$$F_{z,FL_{max}}\Bigg|_{a_y=g,a_x=g} = \underbrace{0.2\cdot mg}_{F_{zF,nom}} + \left|-0.1\cdot mg\right| + \left|-0.08\cdot mg\right| \approx 1.9\cdot F_{zF,nom} = 4693N \tag{3.5}$$

$$F_{zF,nom} = 2470\,\mathrm{N} \tag{3.6}$$

$$F_{z,FR_{max}} = F_{z,FL_{max}} \tag{3.7}$$

$$F_{z,RL_{max}}\Bigg|_{a_y=g,a_x=g} = \underbrace{0.3\cdot mg}_{F_{zR,nom}} + \left|-0.15\cdot mg\right| + \left|0.08\cdot mg\right| \approx 1.76\cdot F_{zR,nom} = 6546N \tag{3.8}$$

$$F_{zR,nom} = 3705\,\mathrm{N} \tag{3.9}$$

$$F_{z,RR_{max}} = F_{z,RL_{max}} \tag{3.10}$$

With this estimation of maximal vertical tire force, the tire forces and options of tire measurement, as described in table 3.1 and 3.2, were chosen.

As it can be seen, the values are not exactly the stationary and double of the stationary wheel load because of the bounded maximal possible tire load of the measurement truck.

tire: 225/40ZR18		
tire force F_z	lateral force F_y	longitudinal force F_x
N	-	-
1500	✓	✓
2500	✓	✓
5000	✓	✓

Table 3.1: tire measurement plan for tire 225/40ZR18.

tire: 265/35ZR18		
tire force F_z	lateral force F_y	longitudinal force F_x
N	-	-
1500	✓	✓
3000	✓	✓
5000	✓	✓

Table 3.2: tire measurement plan for tire 265/35ZR18.

For the rear tires of the Roding, a measurement with $F_z = 3000\,\mathrm{N}$ is selected to be as near as possible at the stationary wheel load of the rear tire. On the other hand, it not selected to high, so that it is not too close to the maximum possible wheel load of $F_z = 5000\,\mathrm{N}$.

For the tire force measurement, the right tire is mounted with $-2\,^\circ$ of camber. This was done to get a second set of measurement data, depended on the camber. As the wheels on the Roding where mounted without camber at the straight ahead drive, the focus is upon the evaluation of the measurement data of the wheel without camber. For a more detailed vehicle model, the camber of the tire has to be considered as well. Because of the geometry of the steering suspension, the front tires changes their camber with the steering angle.

The measurement speed of the measurement vehicle was selected with 60 km/h. At every start of the measurement, a zero measurement was done to calculate the initial offset of the piezo force sensors. Another zero measurement was done at the end of one measurement run to calculate the offset drift of the piezo force sensors. Mostly the sensors for the lateral tire force are sensitive to shearing strain and drifts away.

The measurement truck can be configured to measure three different slip situations:

1. Lateral force: At the lateral force measurement, the wheels are moved from outside $-5\,^\circ$ to inside $15\,^\circ$. The time for this movement is set to 3 s. This time has to be on one hand fast enough to avoid an overheating of the tire and on the other hand slow enough to avoid the influence of the transient tire behavior to the measurement data. A detailed description of the transient tire behavior and the problems which occur at a so fast moving time is provided in further chapters. The rotation of the wheels for one slip configuration and wheel load is repeated 15 - 20 times to get enough data for the later evaluation.

2. Longitudinal force with acceleration slip: At the longitudinal force measurement with acceleration slip, the wheel gets braked to a velocity lower than the vehicle speed. Than the velocity gets increased up to a velocity 40 % higher than the vehicle velocity. In the end, you get a curve with a clear zero cross at a slip rate of 0 %.

3. Longitudinal force with braking slip: During a longitudinal force measurement with breaking slip, the wheel gets accelerated and braked down until it is blocked, so it yields in a curve up to a slip rate of 100 %.

After every run, the asphalt and tire temperature were measured and reported. The whole measurement data of one measurement run is saved in a file for the further evaluation.

3.3 Tire data evaluation

The evaluation of the tire data has to be done separately for every slip configuration and wheel load. In this chapter, the evaluation for the lateral tire force measurement of the rear tires of the Roding (Michelin $265/35ZR18$) at a wheel load of 5000 N is described. With this measurement, the highest load appears on the measurement truck and the measurement equipment. The general process for the other lateral tire force measurements is the same.

First of all, a coordinate system for a general force and moment description has to be defined. The coordinate system used is described in figure 2.3. This definition is very important for the later integration into the vehicle model. Another important convention is, in the SAE and also in the ISO coordinate system, that a positive slip angle leads to negative lateral tire force.

3.3.1 Lateral tire force characteristic

An essential part of the tire data evaluation is a correct filtering of the measured force data. Because of the high load of the whole measurement truck during the measurement drive, a lot of noise gets introduced into the measurement data. The main part of the noise is generated by the mechanical resonance frequencies. Another part of the introduced noise is due to the unevenness of the public roads [20]. To minimize the influence of the noise in the final tire data, a proper filtering has to be performed. As the data evaluation is done offline, the filtering becomes less challenging. The used filtering method is the same as described and used in chapter 2.8. As the noise in this case is much higher, the filter has to be selected carefully to extract the correct signal.

To identify the different frequency components of the measured signal, a Fourier transformation is done. A cutting of the frequency plot is depicted in figure 3.3. As it can be seen, the main frequency components lie in the range of 0 Hz to 7 Hz. Therefore, the cut off frequency was selected at $f_c = 7\,\text{Hz}$.

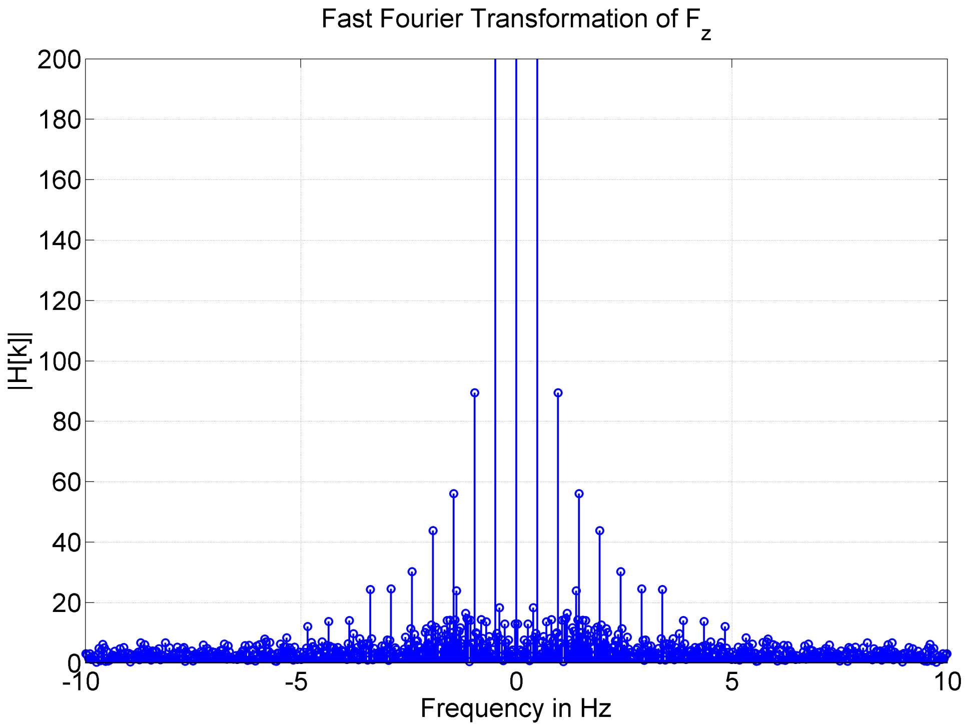

Figure 3.3: Cutting of the frequency domain plot of the measured wheel load F_z.

As filter type, a FIR-Filter, designed with a Hamming window function was selected [2]. The frequency response of the used filter is shown in figure 3.4. The phase of the used filter is less interesting, because the forward-backward filtering method is used to compensate the phase shift of the filter. For the filter design, it is important to select a filter type which has a flat pass band at a value of 0 dB, to prevent a damping for low frequent and constant signals. Because of the forward backward filtering method, an eventual ripple in the pass band increases. This happens, because the magnitude response of the resulting filter transfer function of the forward backward filtering is equal to the square of the original filter function.

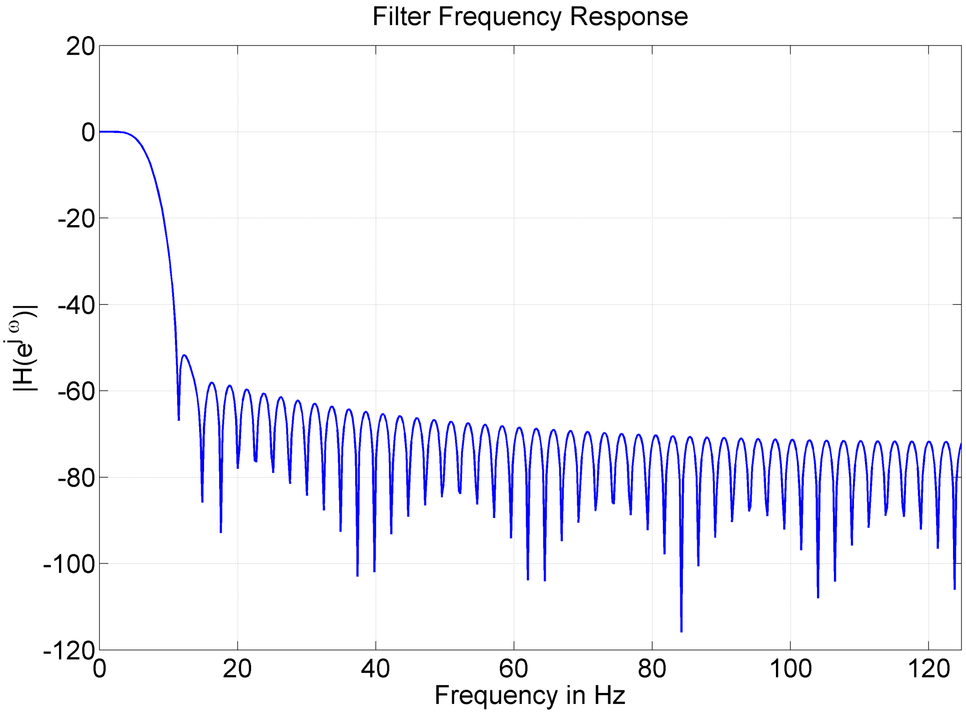

Figure 3.4: Frequency response of FIR-Filter.

An example for the raw measurement signal and the signal after filtering is depicted in figure 3.5. As it can be seen, the right selection of the cut off frequency is important. If the cut off frequency is selected too low, the risk of too much filtering is great. In this case, the initial slope of the lateral tire force is filtered too much. This slope is essential to determine the lateral tire stiffness, used in the linear vehicle model. As the time in which the wheel is been moved from outside to inside for the measurement is very fast, the change of the lateral tire force is fast as well. This fast change corresponds to a relative high frequency part, which has to lie lower than the cut off frequency. An estimation of the frequency part of the slope can be done with a simple measurement of the slope, which lies about $k = 26\,660\,\mathrm{N/s}$. The amplitude of the force value lies about $A = 5290\,\mathrm{N}$. With this parameter, the maximum signal frequency can be estimated with equation (3.11).

$$f_g = \frac{k}{2 \cdot \pi \cdot A} \tag{3.11}$$

This results in a frequency of about $f_g = 0.8\,\mathrm{Hz}$, which is lower than the cut of frequency of 3.9 Hz. A slower time for the measurement motion could reduce the influence of the filter to the slope of the lateral tire force. The filtering has to be done for every measured force.

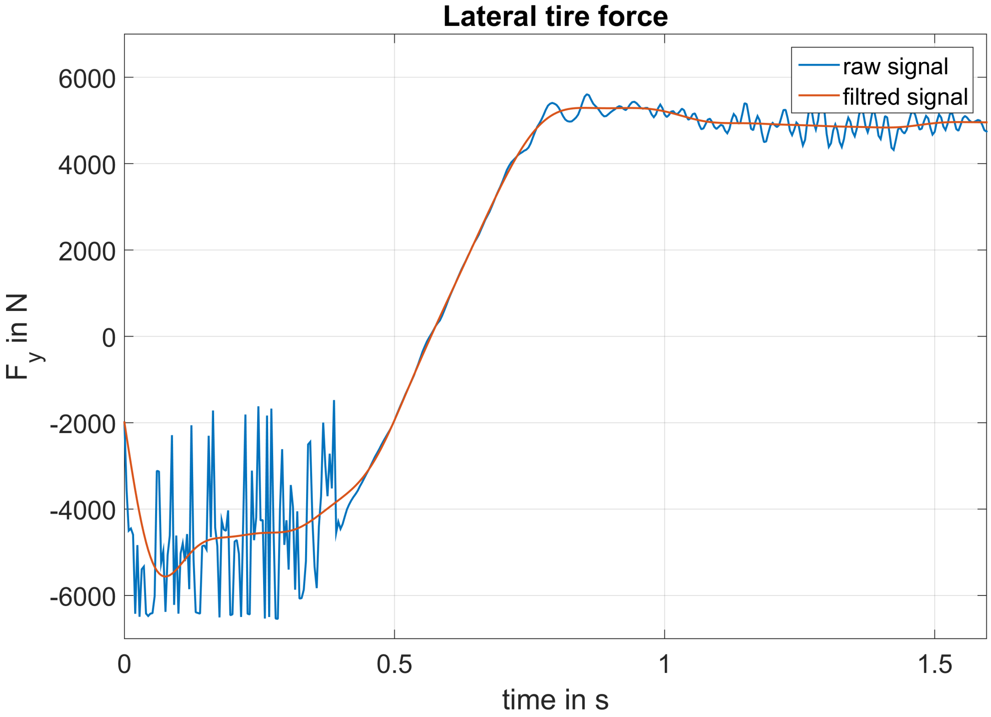

Figure 3.5: Raw- and filtered signal of lateral tire force F_y.

For the tire which is mounted with a camber, a coordinate transformation has to be done. The tire forces have to be transformed with the equation (2.2) from the C-coordinate system into the W-coordinate system. The two important transformation equations are (3.12) and (3.13) .

$$F_{y,trans} = F_y \cdot \cos(\gamma) + F_z \sin(\gamma) \tag{3.12}$$

$$F_{z,trans} = -F_y \cdot \sin(\gamma) + F_z \cos(\gamma) + m_w g \tag{3.13}$$

A disadvantage of the measurement truck is that the wheel load is not controlled. This means that the applied wheel load varies a lot during the measurement. One of the causes of the variation of the vertical force is the roll movement of the whole measurement truck in case of a rough road. For a measurement truck with about 14 t of weight, this variation can be in a range of ±10 % of the first applied wheel load. The second cause of the variation are the moments around the x- and y- axis of the wheel, depended from the applied slip angle. If the contact point between road and tire is not exactly in a line to the vertical axis of the measurement wheel hub, a high force variation can be seen. This becomes clear if you look at figure 3.6, where the wheel load over the slip angle is depicted. For the shown measurement run, a wheel load of 5000 N was adjusted when the truck is stopped.

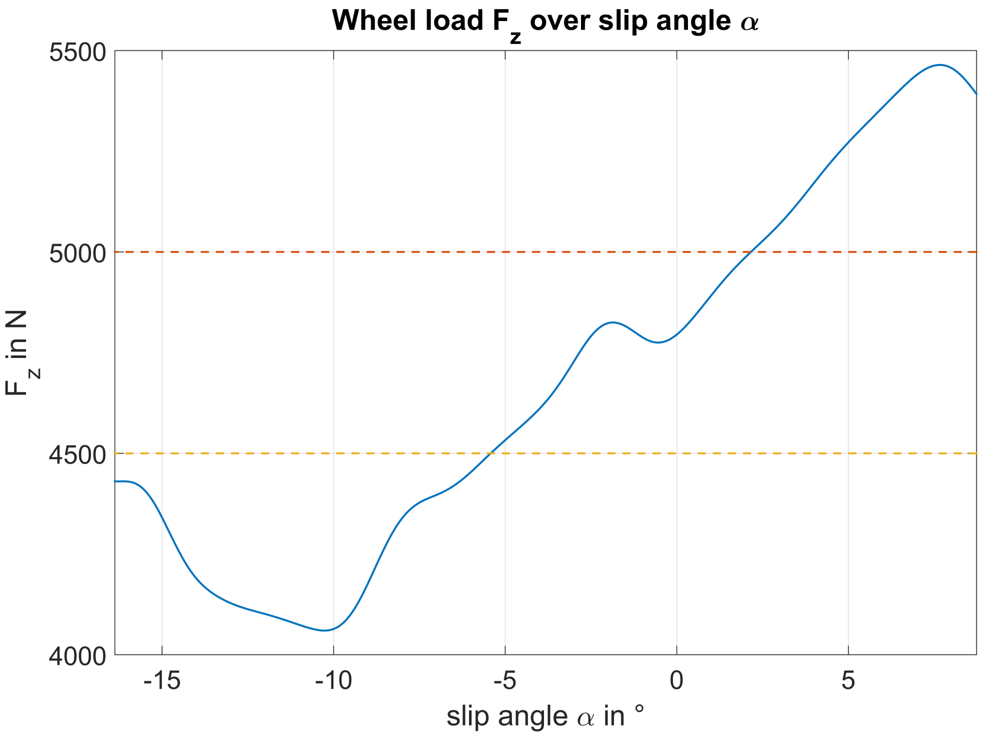

Figure 3.6: Wheel load F_z over slip angle α.

The wheel load changes from a value of about 5100 N to a force of 4000 N, and, at the same time, the slip angle is changing from negative to positive values. This means that the measured wheel load is dependent from the measured lateral tire force and reverse. Another interesting notice can be seen in figure 3.6 at a slip angle lower than $\alpha = -10\,°$. At this point, the wheel load increases again. As it can be seen later in the lateral tire force curve (figure 3.9 and 3.10), at this point of the slip angle, the lateral tire force reaches its saturation. This shows again the dependency of lateral tire force and wheel load.

As the different lateral tire force curves has to be generated for constant wheel loads, the measured lateral tire forces has to be scaled with the measured wheel load. This happens with a simple linear equation 3.14.

$$F_{y,scale} = F_{y,filt} \cdot \frac{F_{z,nom}}{F_{z,filt}} \tag{3.14}$$

As mentioned before, the wheel load was set at 5000 N for this measurement run. In figure 3.14, it can be seen that this force is not reached for the important range between 0 ° to 15 °. Therefore, the wheel load for the scaling was reduced to a value of $F_{z,nom} = 4500\,\mathrm{N}$, to reduce the influence of the scaling.

In figure 3.7, a comparison between the measured force after filtering and the scaled lateral force is shown. As it can be seen, there is less influence at the envelope of the lateral tire force. The biggest influence occures when the slip angles are higher than 5 ° at the saturation of the tire force. In this range, the difference between scaled and not scaled force is in a range of 10 %. This shows with how much carefulness the scaling has to be handled to generate reliable tire data. With this figure, the disadvantage of the non controlled wheel load becomes clear. With the big variation of the wheel load, a high inaccuracy of the tire data, almost in the part where the tires reach their saturation, gets introduced.

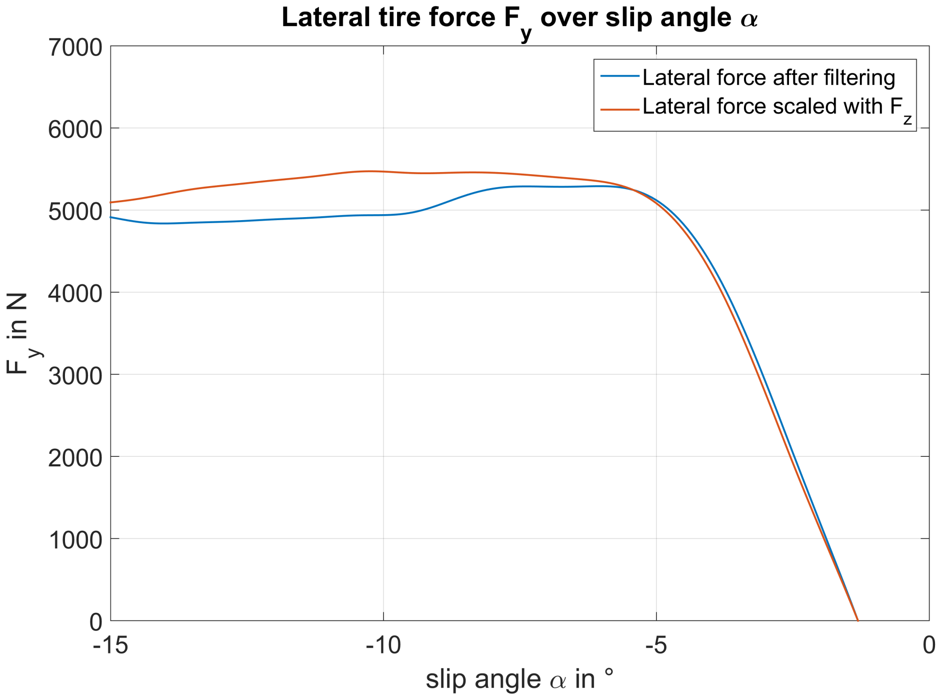

Figure 3.7: Lateral tire force F_y over slip angle α.

In one measurement run, between 17-20 measurements were done for one wheel load setting. With this series of measurement data, random measurement errors can be reduced. An easy way to do this is to average over the different curves. In figure 3.8, the set of lateral tire force curves are plotted in blue. The red curve is the average plot of the different curves.

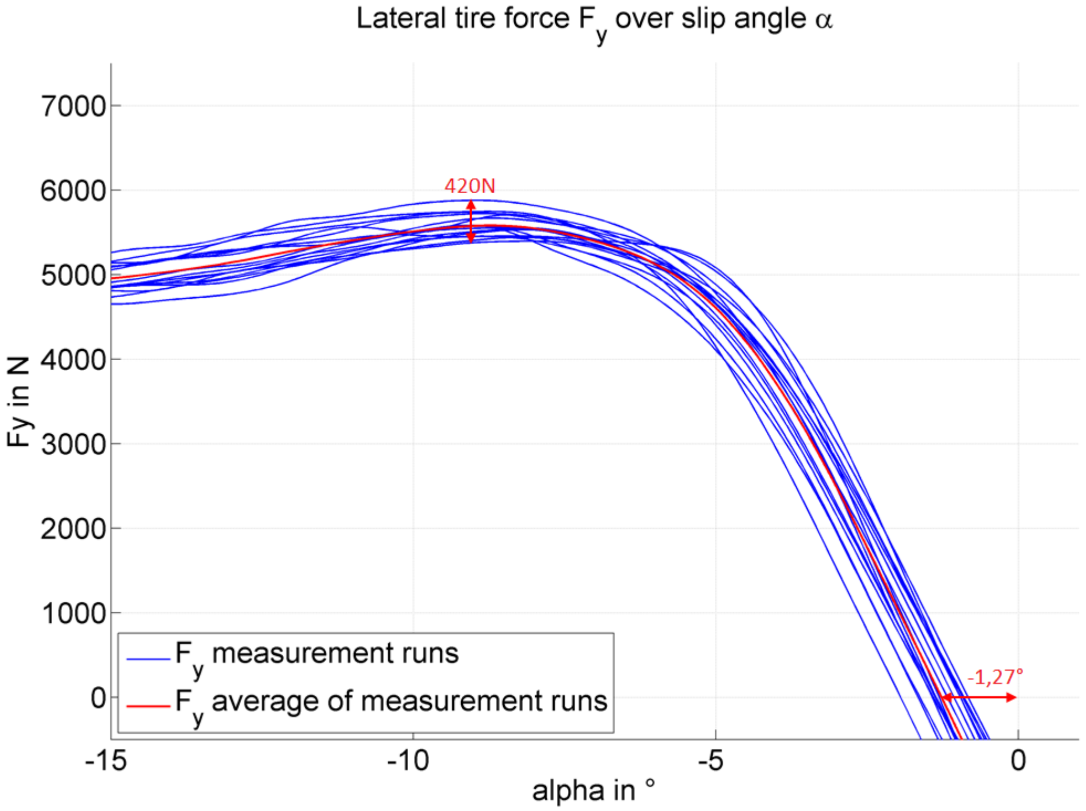

Figure 3.8: Lateral tire force F_y of different measurements and average value over slip angle α.

As it can be seen at the saturation sections of the tire force curves, the lateral tire forces varies in a range of 420 N. This is about 10 % of the applied wheel load. To minimize this variation error, an average curve is calculated.
Another error, which is of a more systematically nature, can be seen at the zero cross point of the lateral tire force. Theoretically, the lateral tire force of a tire with 0 ° of camber should cross the coordinate origin [16]. In this case, the mean value of the different curves has an offset of $-1.27\,°$. This offset error has two different reasons. One reason is the so called ”transient tire behavior”. The second reason is a measurement error of the slip angle sensor. An accurate allocation of the two different effects is difficult,

but an estimation of influences can be done. A detailed description of the transient tire behavior is provided in chapter 3.4.

Generally it can be said, that the lateral tire force behaves like a first order dynamic system with a time constant in a range of 10 ms to 30 ms at a speed of 60 km/h [19]. During the measurement run, the tire gets moved with an angular velocity of 16 °/s from outside to inside. If we assume that the tires have a first order time constant of 25 ms, it corresponds to an angle movement of 0.4 °. This should show the influence of the moving velocity of the wheel to the resulting measured forces. With a slower motion of the wheel, the effect of the transient tire behavior would become insignificant. In our case, a compromise has to be found to correct the offset angle. To compensate the influence of the transient tire behavior, the measured wheel angle gets shifted about 25 ms to the right on the time axis. This is a very rough method to compensate the first order dynamics, but the accuracy is high enough in relation to the whole measurement errors. This compensation yields in a remaining angle offset error of 0.87 °. This error gets compensated with a constant offset correction of the angle.

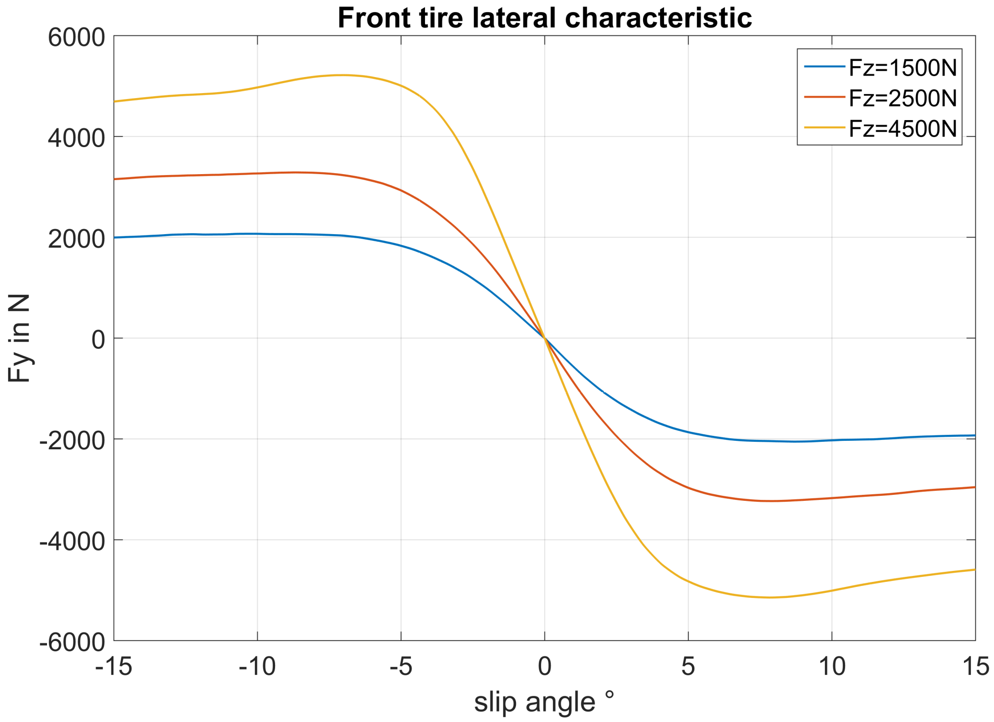

Figure 3.9: Lateral tire force F_y of the front tires at different wheel loads F_z.

The evaluation of the tire data with different wheel loads yields in the lateral tire force characteristic shown in figure 3.9 and 3.10. As described before, the evaluation of the tire data is challenging because of different measurement errors, which can only be reduced with some assumptions but not completely avoided. Due to this fact, it has to be always kept in mind that the resulting tire characteristic of figure 3.9 and 3.10 can vary in practice.

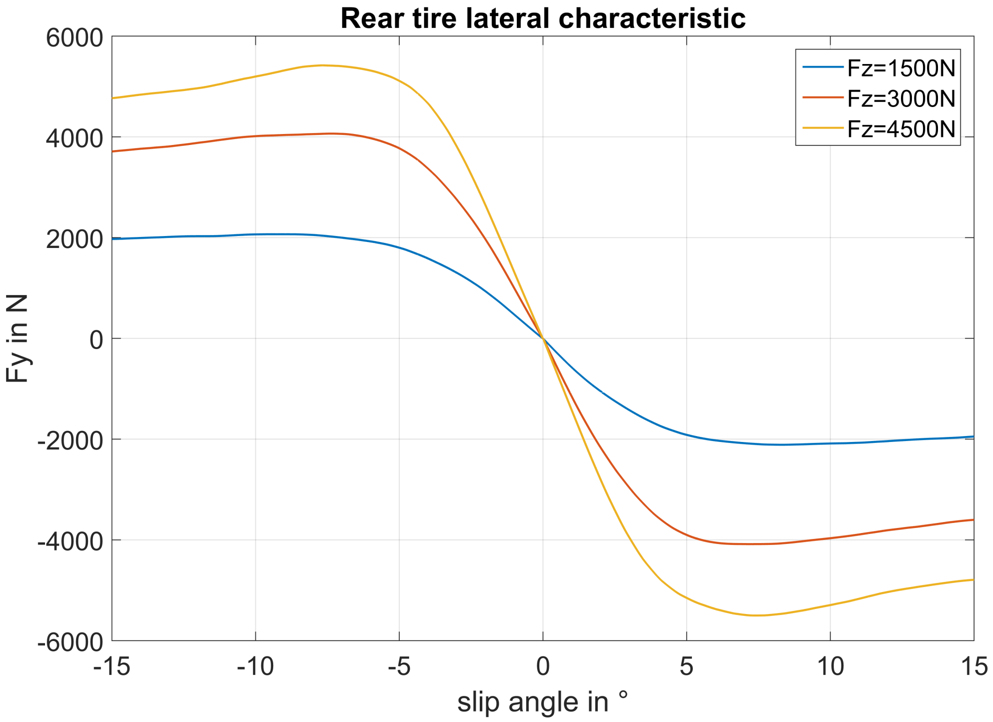

Figure 3.10: Lateral tire force F_y of the rear tires at different wheel loads F_z

To illustrate the degressive behavior of the lateral tire force F_y in relation to the wheel load F_z [12], the lateral tire characteristic is normed with the wheel load. The result for the front is depicted in figure 3.11. The y-axis of the figure is the friction coefficient $\mu(\alpha)$. As it can be seen, the maximum of the friction coefficient lies in a range of the slip angle α between $5\,^\circ$ and $8\,^\circ$. For the wheel load of 1500 N, the maximum friction coefficient is about $\mu_{max} = 1.4$. The higher the wheel load F_z gets, the lower the maximum of the friction coefficient becomes. For the highest wheel load of 4500 N, the maximum friction coefficient is $\mu_{max} = 1.15$.

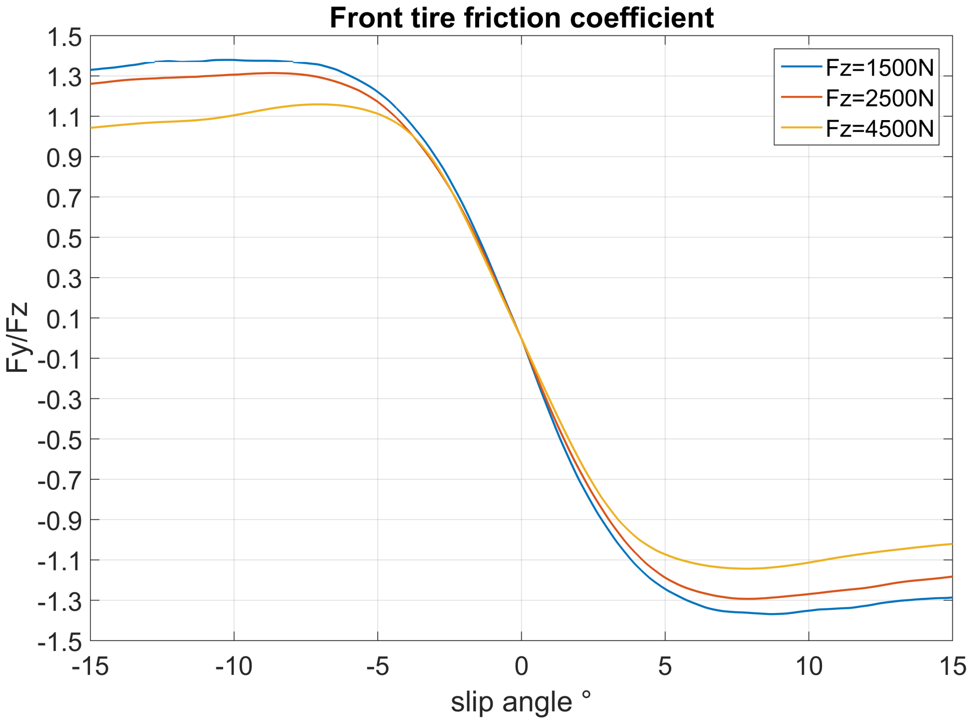

Figure 3.11: Lateral friction coefficient $\mu(\alpha)$ of the front tire.

The previous described evaluation was done for the tires which were mounted without camber γ. As this is the case for the Roding, this data is most important for the vehicle model. Nevertheless, also the measured data for the wheels which were mounted with $\gamma = -2\,^\circ$ of camber where evaluated. As mentioned before, for tires with $\gamma = 0\,^\circ$ of camber the lateral tire force characteristic is zero, for a slip angle $\alpha = 0\,^\circ$. For tires with camber, this is not true anymore [13]. For tires with negative camber, a positive shift along the y-axis of the lateral tire force is expected. As this offset shift is not known, the evaluation is much more challenging than the evaluation of the tire characteristic without camber as there is one unknown variable more. To estimate this offset value, the difference between the maximum force values of the tire forces with camber $\gamma = 0\,^\circ$

and $\gamma = -2\,^\circ$ has been taken. Afterwords, the lateral tire force curves get shifted along the x-axis to set the estimated offset value at the slip angle of $0\,^\circ$. This is a less accurate method to generate tire data for tires mounted with camber but it is sufficient to have a comparison with tire data without camber. The resulting lateral tire force characteristic with $\gamma = 0\,^\circ$ and $\gamma = -2\,^\circ$ are depicted in figure 3.12 and 3.13.

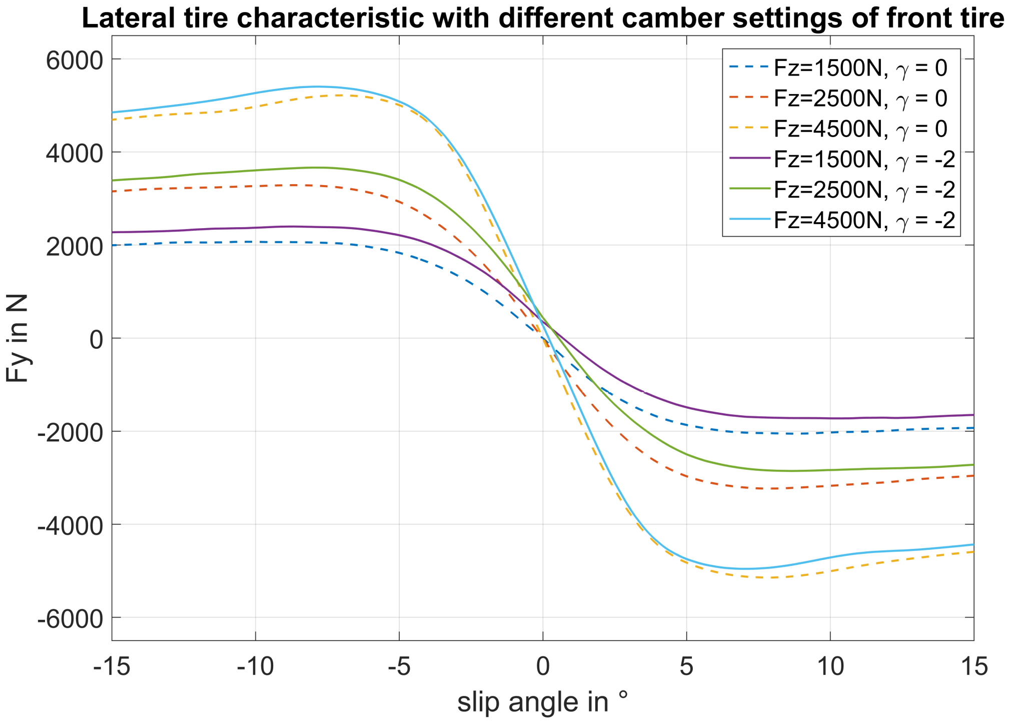

Figure 3.12: Lateral tire characteristic for different camber settings of the front tires.

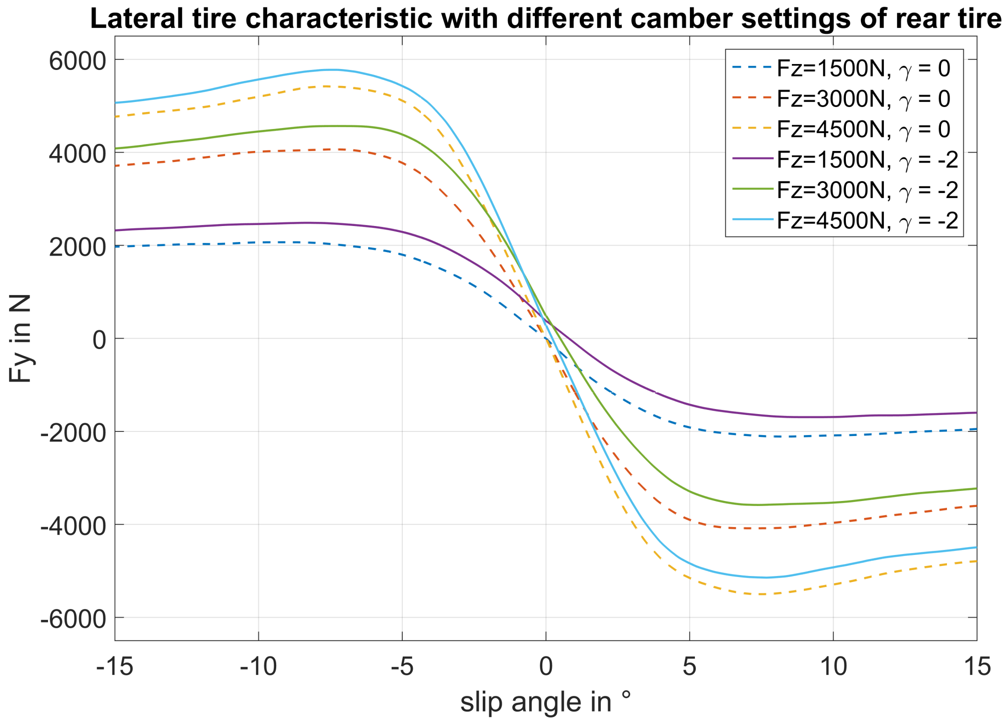

Figure 3.13: Lateral tire characteristic for different camber settings of the rear tires.

The statement that the camber setting of the Roding is equal to $\gamma = 0\,^{\circ}$ is only valid when no steering angle is applied to the wheels. Primary, the front wheels changes their camber angle in relation to the applied steering angle. The different wheel loads have influence to the camber settings of the vehicle as well. Tire models to consider this change of the camber, which can be parametrized with the tire data depicted in figure 3.12 and 3.13, exist. For the vehicle models described in chapter 2, a detailed modeling of the steering and the vehicle body is necessary to consider the wheel camber. This can be done in a further work to refine the vehicle model.

3.3.2 Longitudinal tire force characteristic

Also the evaluation of the measurement data of the longitudinal tire characteristic is done. This is made in prospect for the extension of the lateral vehicle model with a longitudinal model of the vehicle. In the actual vehicle model implementation, the longitudinal vehicle motion is neglected.

The longitudinal tire force characteristic is, like the lateral tire force, a nonlinear function of the wheel slip rate. The slip rate is the difference between the rotation speed of the wheel and the velocity of the vehicle. It is divided between the acceleration slip rate and the braking slip rate. The different definitions from [13] are described in equation (3.15) and (3.16). As it can be seen, the slip rate is positive at acceleration but negative at braking.

$$s_{acc} = \frac{w \cdot r_e - v_x}{|\omega| \cdot r_e} \tag{3.15}$$

$$s_{brake} = \frac{w \cdot r_e - v_x}{|v_x|} \tag{3.16}$$

ω...wheel speed
r_e...effective radius of the wheel
v_x...longitudinal velocity of the vehicle

The main evaluation of the longitudinal measurement data is the same as for the lateral force data, but it is not described in detail in this chapter. The only difference is the calculation of the slip rate out of the wheel speed and the vehicle speed. Also the longitudinal tire characterisic was measured for a tire with $0\,°$ and $-2\,°$ of camber. The resulting tire data for the front and rear tire is depicted in 3.14 and 3.15. As it can be seen, the camber has less influence on the longitudinal than the the lateral force characteristic. Another notice is the different tire force maximum for acceleration and brake slip, described in [13, pag. 23]. For the acceleration slip the maximum is higher than for the brake slip. The maximum longitudinal tire force is in a slip range of 10 %.

At the measurement for a brake slip at a wheel load of 5000 N of the rear tires, the secondary hydraulic motor has not enough power to brake down both wheels. Therefore, the measurement works only for the left wheel; the right wheel is not braked down. Because of this, no measurement data for the left wheel without camber is provided. As the influence of the camber is insignificant, the curve of the right wheel can be taken also for the left wheel. The evaluated tire data can be used to generate a tire model for the longitudinal tire characteristic.

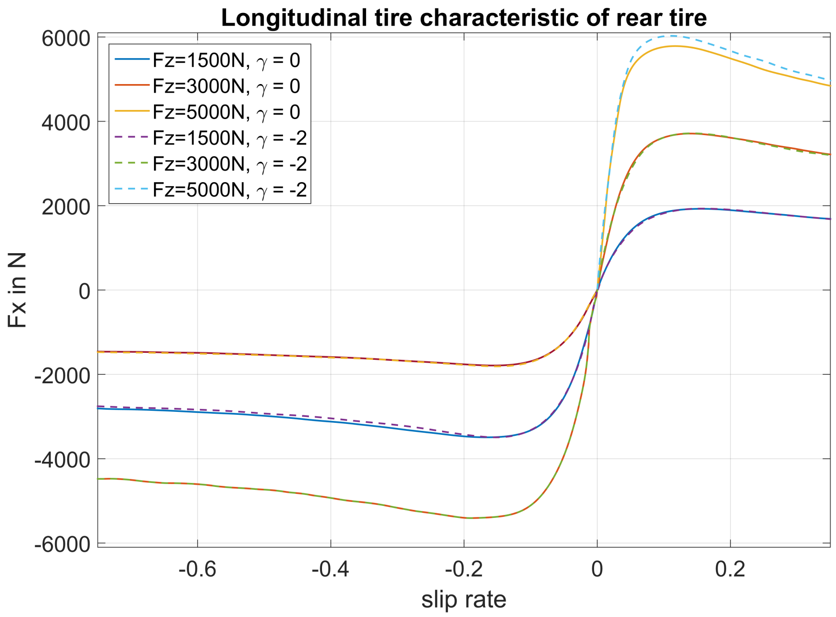

Figure 3.14: Longitudinal tire characteristic for different camber settings.

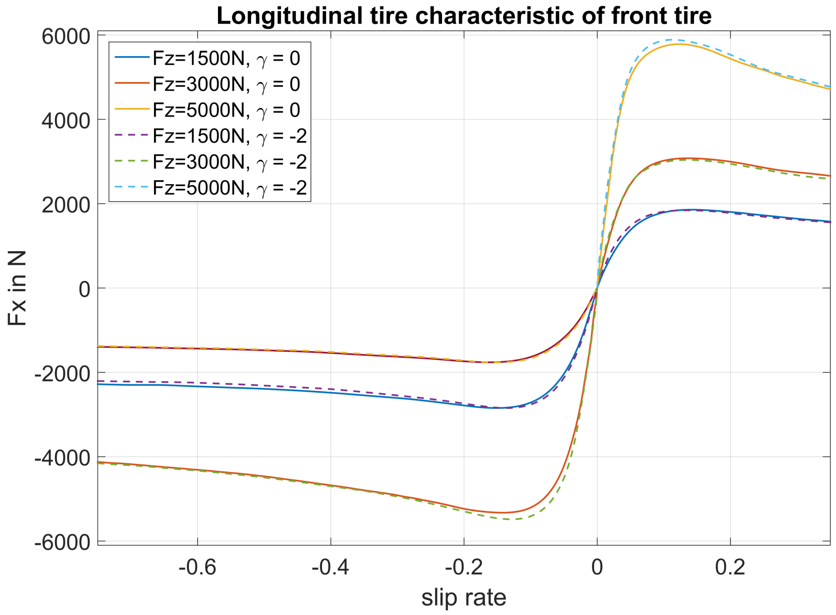

Figure 3.15: Longitudinal tire characteristic for different camber settings.

3.4 Transient tire behavior

The tire is a complex, nonlinear mechanical system with different transfer functions in all directions of the different applied forces. In this chapter, the dynamic behavior of the lateral force is described.

Tire forces are generated by local deformation of the rubber. As a result of this, longitudinal and lateral tire forces have a transient behavior, which means that the lateral tire force F_y follows the slip angle α after a certain time [20]. The modeling of this effect is important for the dynamic description of the vehicle because a delayed tire force generation yields in a delayed reaction of the vehicle.

The common method to the physical description of the transient tire behavior is based on the theory of the stretchable band. [3] shows an abstract of the different approaches to the transient tire behavior based on the theory of the stretchable band. There the approaches of SCHLIPPE and DIETRICH [21, 22], SEGEL[23] and PACEJKA [17] are described.

In this work, the approach of BÖHM [4] is considered. He describes the transient tire behavior as a first order system with the following equation (3.17)

$$\frac{c_\alpha}{c_y \cdot v} \cdot \dot{F}_y + F_y = c_\alpha \cdot \alpha \tag{3.17}$$

The Laplace transformation yields in equation (3.18)

$$G(s) = \frac{1}{1 + sT_e} \tag{3.18}$$

The parameter T_e is a time constant dependent from the wheel speed. A first approximation of the parameter T_e can be done with the following equation [18]:

$$T_e = \frac{c_\alpha}{c_y \cdot v} \tag{3.19}$$

c_α is the linear tire stiffness and c_y the lateral spring stiffness of the tire. Whereas the lateral tire stiffness is known from the tire measurement, the spring stiffness is unknown but in a range of $c_{y\alpha} = 200\,\frac{\mathrm{N}}{\mathrm{mm}}$[18]. For further simulations, the spring stiffness has to be refined with different driving maneuvers.

The time constant T_e, used in the simulation model, lies in a range between 15 ms and 40 ms, depending on the actual vehicle speed. This time constants seems to be small compared to the maximal vehicle frequency of about 4 Hz. The influence of the transient tire behavior becomes clear in dynamic maneuvers, like a step input.

To show the difference between the vehicle model with and without tire dynamics, a step input with a maximum lateral acceleration of about $5\,\mathrm{m/s^2}$ was done. The difference of the simulation of a model with static and transient tire behavior is depicted in figure 3.16.

As it can be seen in figure 3.16, the simulation with the transient tire behavior follows the measured yaw rate very well, almost in the initial phase where the highest steering wheel change is done. The simulation with the static tire behavior has a clear phase difference to the measured yaw rate. This phase difference can become a problem for the under steering detection because the difference of the measured and estimated yaw rate is high. Another difference between the model with static and transient tire behavior can be seen at the overshoot of the estimated yaw rates. The simulation with a static tire force model has a small overshoot and yields fast in the final yaw rate value. However, the model with transient tire behavior has a higher overshoot, almost the same as the measured yaw rate. This deviation in the overshoots can yield in a wrong over steering detection, because the difference between the model with static tire force and the measured yaw rate is high. To avoid these problems and to have a higher model accuracy, the dynamic tire force model was introduced for the linear- as well as for the nonlinear single track model.

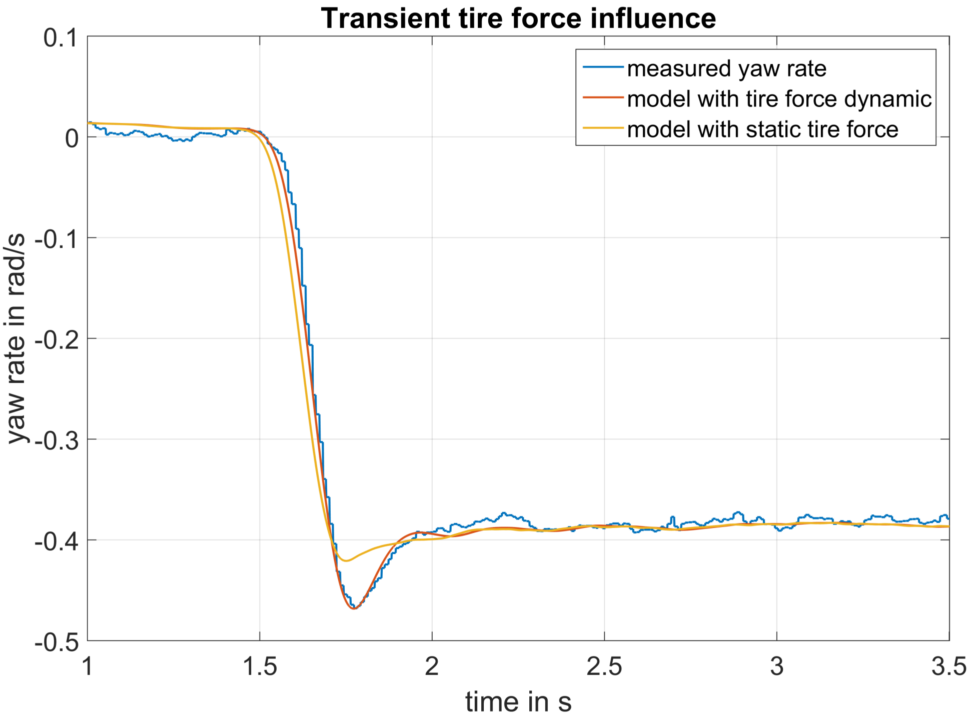

Figure 3.16: Comparison of yaw rate with transient and static tire force behavior.

3.5 Tire Model selection

In the chapter before, the tire data has been evaluated out of different measurement runs. For an accurate vehicle model, a tire model has to be generated out of the evaluated tire curves. As these models are the only connection between the vehicle and the road, an accurate tire model is the most important part of a vehicle model. The challenging part of the tire model is the modeling of the nonlinear part of the tire characteristic.

A lot of different tire modeling methods exist, which can be primary divided in three different categories:

- mathematical models
- semi-physical models
- physical models

The exact classification of each tire model is not always fully clear. A detailed description and classification of the different tire models is provided in [20]. In this work, the tire models MF-Tyre, Burckhardt Tire Model and the TM-Simple tire model are presented, which are also some of the most common used models in vehicle simulation.

3.5.1 Magic-Formula Tire Model (Pacejka Tire Model)

The Pacejka tire model [3], also called Magic Formula Model, is one of the most commonly used tire models. The original model is a mixture between physical and heuristic model approaches and consists of around 15 parameters. As the magic formula was presented decades ago, lots of derivations of this model exist. The basic equation of the Pacejka Tire model is shown in equation (3.20).

$$y(x) = D \cdot \sin[C \cdot \arctan\{B \cdot x - E \cdot (\cdot x - \arctan(B \cdot x))\}] \tag{3.20}$$

The four parameter B to E are supposed to be constant for a simple version of the Magic Formula model with four parameters. In the original version of the model, this parameters are also functions of parameters. The meaning of the four Parameters is as follows:

B...stiffness factor
C...shape factor
D...peak value
E...curvature factor

With two additional parameters, you can also provide a shift in horizontal and vertical direction to consider tire pressure or camber influence on the tire force. The equations therefore are provided in (3.21) and (3.22):

$$Y(X) = y(x) + S_V \tag{3.21}$$

$$x = X + S_H \tag{3.22}$$

A graphical description of the Magic formula parameters is provided in figure 3.17. For a more detailed description of the Parameters see [16].

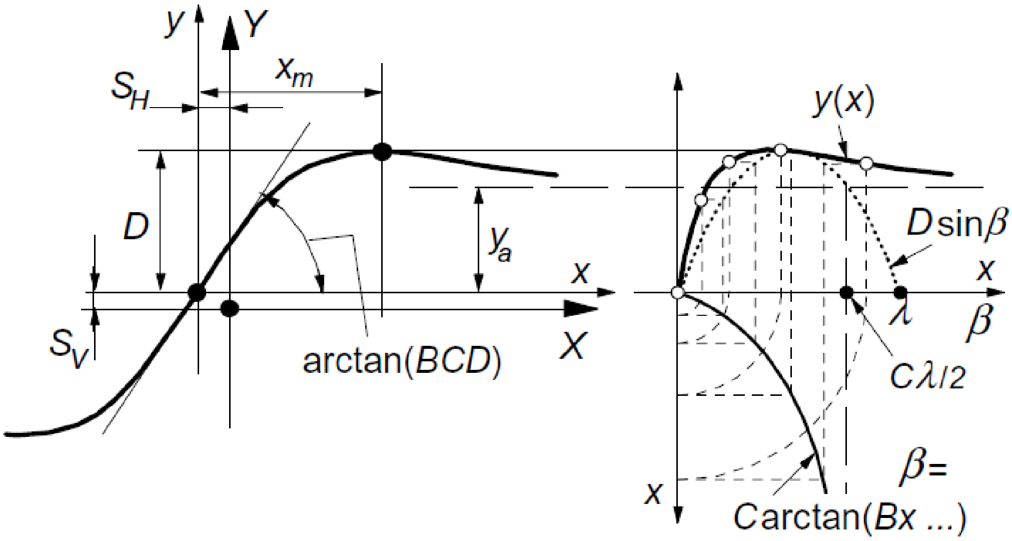

Figure 3.17: Graphical description of Magic Formula equation parameters from [16].

The main advantages of the Magic Formula model are:

- the qualitative characteristic tire force curve can be reproduced
- the curve is changeable within the four parameters, which comes with a small parametrization effort
- the single parameters describe a physical tire characteristic, which simplifies the parametrization
- a very accurate mapping of different input variables like wheel load, camber velocity and tire pressure is possible
- the function is continuous, which is important for simulation algorithms.
- the function is symmetric to central point, what is important for the simulation of positive and negative slip angles or slip rate.

The variation of the wheel load can be considered in the parameter D as a linear approach. This would be important for the vehicle model to consider the variation of the wheel load. This simple way has the disadvantage that the tire force is only linear dependent from the wheel load, which satisfies the reality only in a bounded range. For the use in the previous described vehicle model, the accuracy would be sufficient.

3.5.2 Burckhardt Tire Model

Another simple approach for a tire model is the Burckhardt tire model [10]. He describes the friction coefficient μ_{res} between wheel load F_z and tire force F. λ_{res} is the slip angle or slip rate of the tire, and v is the vehicle speed. The equation of the Burckhardt model is described in (3.23). The variation of the wheel load F_z is considered in the model of Burckhardt, in common with the parameter c_5. The dependency of the tire force from the tire velocity is considered with the velocity v and the parameter c_4.

$$\mu_{res} = (c_1 \cdot (1 - e^{-c_2 \cdot \lambda_{res}}) - c_3 \cdot \lambda_{res}) \cdot e^{-c_4 \cdot \lambda_{res} \cdot v} \cdot (1 - c_5 \cdot F_z^2) \tag{3.23}$$

For the parametrization of the Burckhardt tire model, the parameters c_1 to c_5 have to be selected properly. The parameters c_1 to c_3 have a physical meaning. c_1 affects to the maximum value of the tire force, c_2 shifts the maximum value along the horizontal axis and c_4 is the sliding coefficient. With this influence of the parameters, an easy parametrization is possible.

3.5.3 TM-Simple Tire Model

The TM-Simple Model [11] is a simple tire model for lateral and longitudinal tire characteristic. The model calculates the tire force in dependency of the slip rate or slip angle and the wheel load F_z. The road is defined to be even and camber influence is neglected. The main equation for the tire force is shown in equation (3.24).

$$Y = K \cdot \sin[B(1 - e^{\frac{-|X|}{A}})\mathrm{sign}X] \tag{3.24}$$

X corresponds to the slip quantity. Furthermore, in this model, the parameters K,B and A have physical influence on the model.

The Parameter K is the maximum force value of the corresponding tire force curve. It can also be written as in equation (3.25).

$$K = Y_{max} \tag{3.25}$$

The Parameter B is calculated out of the saturation value Y_∞ and the maximum value Y_{max}. The following equation (3.26) holds:

$$B = \pi - \arcsin \frac{Y_\infty}{Y_{max}} \tag{3.26}$$

The Parameter A is a combination of the previous described parameter K and B as well as the initial envelope of the tire characteristic. The following equation (3.27) holds:

$$A = \frac{1}{dY_0} \cdot K \cdot B \tag{3.27}$$

A graphical description of the TM-Simple tire parameters is provided in figure 3.18.

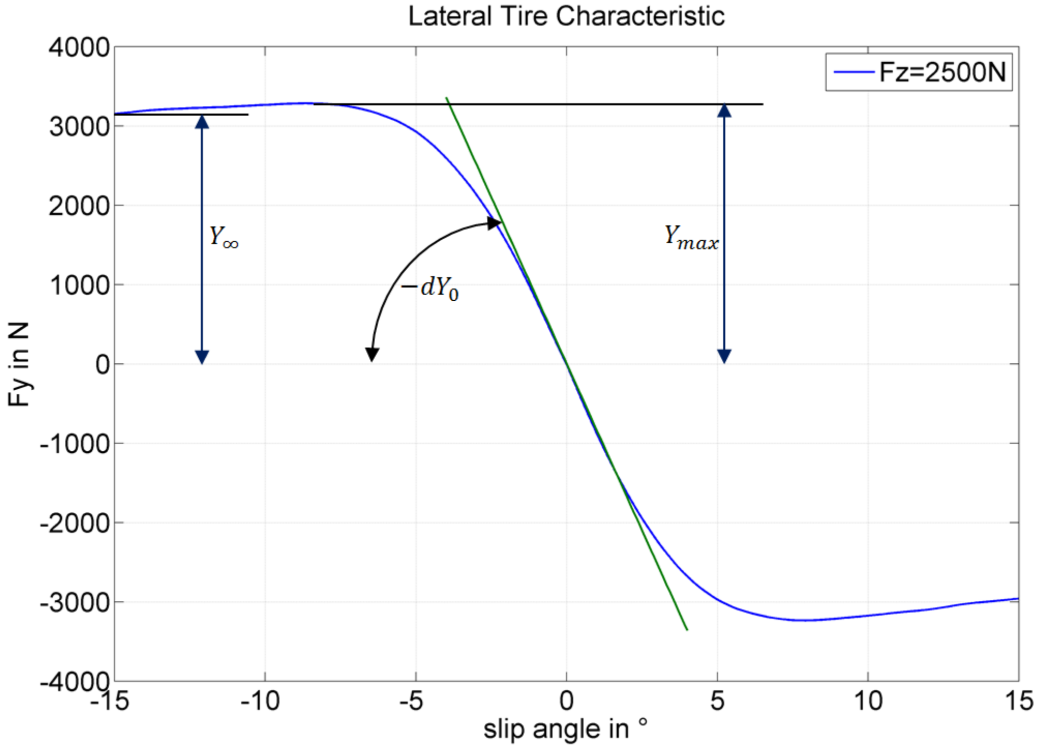

Figure 3.18: Graphical description of TM-Simple equation parameters.

To consider the influence of the wheel load F_z three new polynomials where introduced as follows (3.28), (3.29) and (3.30):

$$Y_{max}(F_z) = a_1 \frac{F_z}{F_{z,nom}} + a_2 \left(\frac{F_z}{F_{z,nom}}\right)^2 \tag{3.28}$$

$$dY_0(F_z) = b_1 \frac{F_z}{F_{z,nom}} + b_2 \left(\frac{F_z}{F_{z,nom}}\right)^2 \tag{3.29}$$

$$Y_\infty(F_z) = c_1 \frac{F_z}{F_{z,nom}} + c_2 \left(\frac{F_z}{F_{z,nom}}\right)^2 \tag{3.30}$$

For two measurements at different wheel loads, for example $F_z = F_{z,nom}$ and $F_z = 2 \cdot F_{z,nom}$, the coefficients a_n, b_n and c_n can be determined. Representatively, the equations for a_1 and a_2 are described in equation (3.31) and (3.31). Due to the nonlinearity of the equations (3.28), (3.29) and (3.30), the digressive influence of the wheel load F_z is taken into account.

$$a_1 = 2 \cdot Y_{1,max} - \frac{1}{2} Y_{2,max} \tag{3.31}$$

$$a_2 = \frac{1}{2} Y_{2,max} - Y_{1,max} \tag{3.32}$$

Another important feature of the TM-Simple model is the possibility of an easy combination of lateral and longitudinal tire forces. If at a driving maneuver like braking during cornering, longitudinal and lateral tire forces act on the tires, these forces are not independent from each other [12]. The lateral tire force gets reduced for a simultaneous acting longitudinal force and reverse. The graphical depiction yields in the so called traction circle. Generally, the potential for longitudinal forces is higher than for lateral forces; therefore it is more an ellipse than a circle. A principle figure for the traction circle is depicted in 3.19.

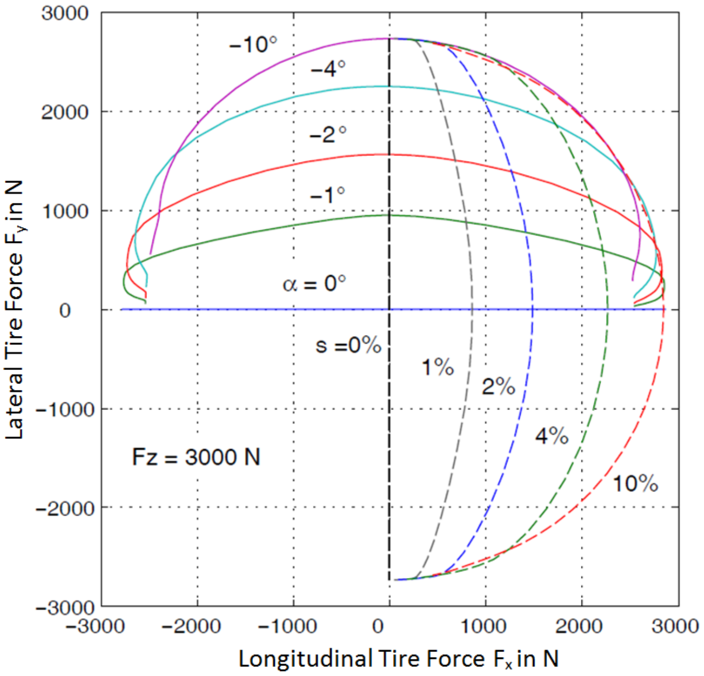

Figure 3.19: Principle depiction of traction circel from [12].

The slip angle α has to be transformed according to equation (3.33) and (3.34) in order to consider the previous described dependency of longitudinal and lateral tire force.

$$sl_y := \frac{\alpha}{G(F_z)} \tag{3.33}$$

$$G(F_z) := \frac{A_y}{A_x} \frac{K_x \cdot B_x}{K_y \cdot B_y} \tag{3.34}$$

The longitudinal slip sl_x rate remains in its origin and the vector s in equation (3.35) can be written. The vector includes the angle β.

$$\boldsymbol{s} := \begin{bmatrix} sl_x \\ sl_y \end{bmatrix} \tag{3.35}$$

Out of the new calculated vector $\boldsymbol{s}$, the magnitude of the resulting force Vector $\boldsymbol{F}$ can be interpolated as shown in equation (3.36). The forces F_x' and F_y' are the base values for the longitudinal and lateral tire force.

$$F = |\boldsymbol{F}| = \frac{1}{2}\left[Fx' + Fy' + (Fx' - Fy')\cos 2\beta\right] \tag{3.36}$$

The vector $\boldsymbol{F}$ can be splitted in its lateral and longitudinal components as follows (3.37):

$$\boldsymbol{F} := \begin{bmatrix} F_x \\ F_y \end{bmatrix} = F \begin{bmatrix} \cos\beta \\ \sin\beta \end{bmatrix} \tag{3.37}$$

These previous equations can be implemented in a simple and efficient way which ensures the real time condition of the model. As at this moment no usable signals of the wheel speed sensors are available, the combination of longitudinal and lateral tire force is not needed. Nevertheless, the goal in further works is to extend the model with longitudinal vehicle characteristic to generate a higher accuracy.

In the previous description, three commonly used tire models where presented and described. All three tire models are easily implementable and provide real time capability. For the simulation in the vehicle model, the TM-Simple tire model is been selected. This selection has been done for different reasons. First of all, the TM-Simple model is the one that has the smallest number of parameters to optimize. This makes it simple to generate an accurate tire model. Another reason is the possibility to consider the digressive wheel load influence to the tire force, which is important for driving maneuvers at high lateral acceleration over $a_y = 5\,\mathrm{m/s^2}$. The last reason for the selection of the TM-Simple model has been done in prospect of the further extension of the model. As the combination of longitudinal and lateral tire force is possible with least effort in modeling, the TM-Simple model has been choosen.

3.6 Tire Model parametrization

In the previous chapter, several reasons for the selection of the TM-Simple tire model have been shown. One further reason is the simple parameter identification. This allows all the parameters of the TM-Simple formula (3.24) to be selected out of the measured tire characteristic as described in figure 3.18.

For the parameter identification of the TM-Simple model a Matlab script was made to automatize this progress. To generate a high accuracy between the measured tire characteristic and the tire model, the Matlab function ”fminsearch” is been used. For the initial values, a algorithm has been developed to determine the TM-Simple parameters out of the measured tire characteristic. For the cost function of the optimization the least squares error function, which is defined as follows (3.38), was selected.

$$J = \sum_{n=1}^{N} (Y_{meas}[n] - Y_{TM}[n])^2 \tag{3.38}$$

Y_{meas}...measured tire force
Y_{TM}...tire force calculated with tire model

The optimization algorithm was executed for two different tire forces, which were 1500 N and 4500 N. With this resulting parameter sets, the Parameters a_n, b_n and c_n can be calculated to consider the influence of the different wheel loads. In table 3.3 the resulting tire parameters are shown.

Parameter	Front Tire	Rear Tire
a_1	2224.3	2258.8
a_2	-168.63	-142.3
b_1	38980	37807
b_2	-2285.2	-1488.9
c_1	1832.7	17581.1
c_2	-218.1	-223.582
$F_{z,nom}$	1500 N	1500 N

Table 3.3: Tire Model Parameters.

To validate the generated tire parameters, the measured tire data for the tire load of both the front tire (2500 N) and the rear tire (3000 N) have been used. The TM-simple formula has been evaluated for the three different wheel loads of the tire measurement to compare the difference between the model and the real measured data. In figure 3.20 and 3.21 the different tire characteristic for the front and rear tire is depicted. As it can be seen, for the front tire in figure 3.20, the tire model and the real tire measurement data is very accurate for all three wheel loads. On contrary, for the rear tire in figure 3.21, the accuracy for the validation tire data with a wheel load of 3000 N is lower. This lower accuracy is a disadvantage of the TM-Simple tire model. The tire model was generated with different wheel load combinations for the optimization, to compare the accuracy for the validation data. The accuracy of the model showed no clear improvement; therefore the tire model parameter of table 3.3 where used. The decision for this parameters was also done in regard to the simulation of the vehicle model.

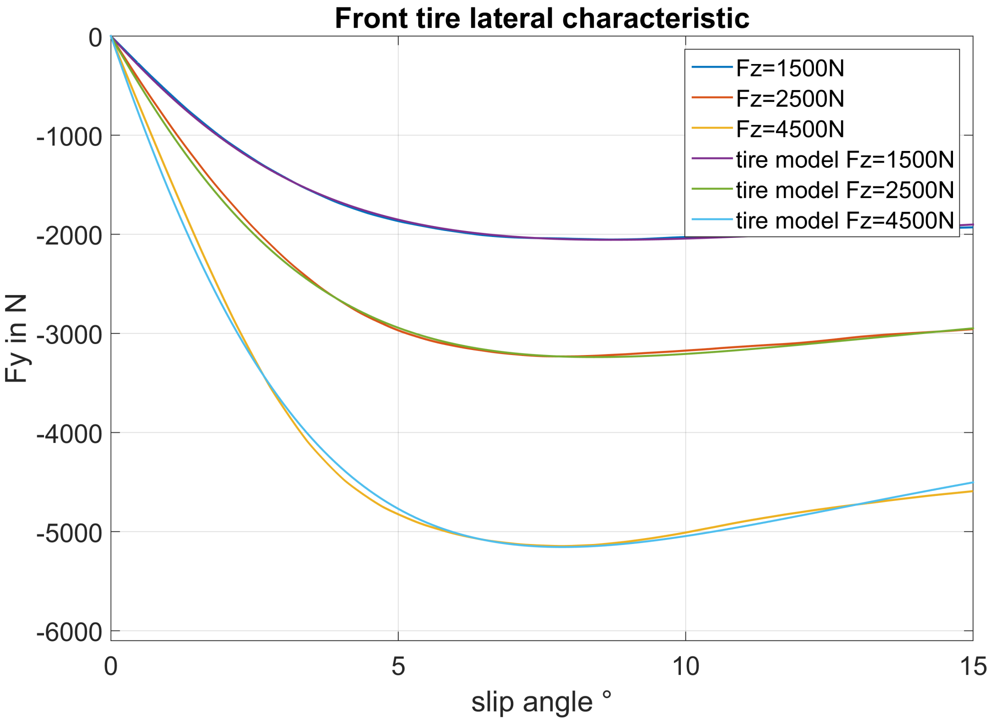

Figure 3.20: Comparison of TM-Simple model with real tire measurement data of front tire.

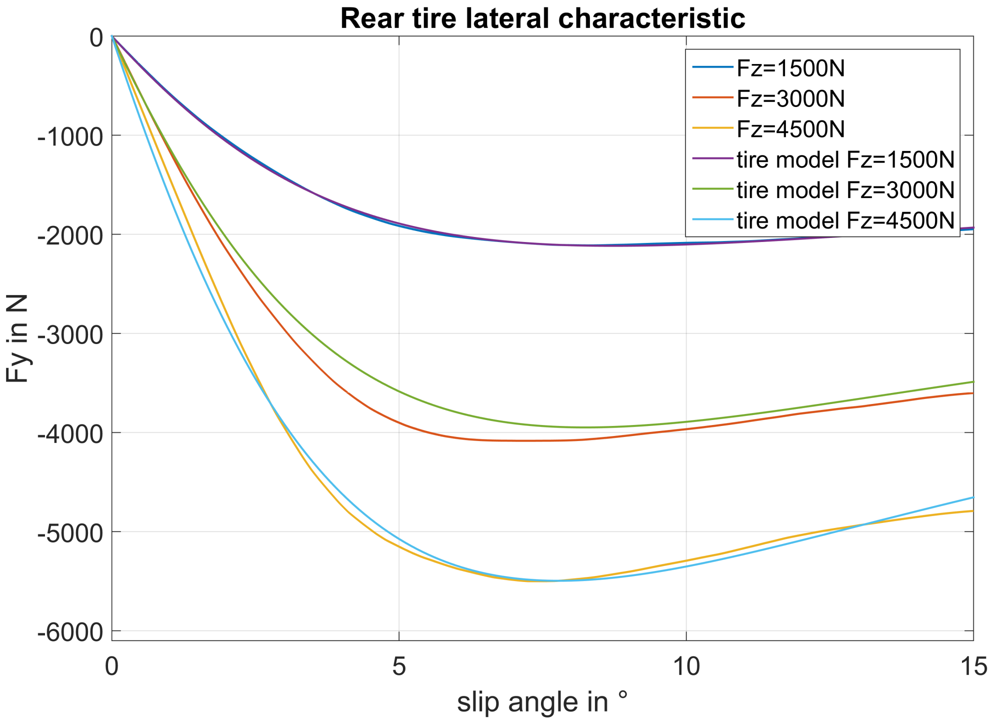

Figure 3.21: Comparison of TM-Simple model with real tire measurement data of rear tire.

Out of figure 3.20 and 3.21 can be seen how challenging the generation of an accurate TM-Simple tire model can be. The single TM-Simple tire curve can be easily optimized to suit the measured data, but because of the dependency of the wheel load, the accuracy is lower. Also in this case, the decision for the model parameters has to be done after a simulation of the whole vehicle model. To have two more degrees of freedom to refine the vehicle model result, two separate gains for the front and rear tire have been introduced to scale the tire force. The scaling factor lies in a range of $\pm 3\,\%$ of the tire force. This scaling factor is acceptable in relation to the measurement errors of the whole tire force measurement and tire model generation. When using the tire model, it has always to be kept in mind that the accuracy is limited due to the different measurement errors, described in this chapter.

NO model has been generated yet for the longitudinal tire characteristic. For a further extension with a longitudinal vehicle model, the algorithm which was previously shown can be used to generate a tire model for the longitudinal tire characteristic.

4 Model Validation

The vehicle model validation and improvement is a very complex process which requires certain maneuvers, thus because of space requirements and safety the necessary test drives can not be done on public roads. Therefore, the validation maneuvers were done on the test track in Idiada within three test weeks, in which the model was refined step-by-step. The necessary validation maneuvers have to be selected properly to cover a wide spectrum of driving situations. Therefore, the following standard maneuvers were selected:

- Constant radius
- Sinusoidal steering input
- Frequency response
- Step input
- Swept steer input

The main refining process of the vehicle model was done manually without any optimization algorithm. This method is very time consuming but necessary because of the high number of parameters and the strong dependency of each other. Before every variation of a parameter, the influence of the parameter on the actual driving maneuver has to be estimated. Otherwise there is a high risk to modify a wrong parameter too much and this has low influence on the simulation result. Another challenge of the parameter optimization is the consideration of the dependency of the different parameters on each other. For this master thesis, the main aspect lies on an accurate estimation of the vehicle yaw rate. Therefore, the simulation results were optimized in view of the yaw rate. Deviations of the simulated lateral acceleration a_y or the slip angle β from the measurement are accepted up to a certain range. The validation of the simulated slip angle β is challenging because of its complex measurement. The slip angle β can't be measured directly, but it has to be calculated out of the measured longitudinal an lateral acceleration of the optical velocity sensor with the equation (4.1).

$$\beta_{meas} = \arctan\left(\frac{v_y}{v_x}\right) \tag{4.1}$$

As the measured lateral velocity v_y is very low for normal driving maneuvers with a lateral acceleration lower than $5\,\mathrm{m/s^2}$, measurement noise has a strong influence on the measurement of v_y and also on β. Because of this, the lateral acceleration a_y is used as a second validation variable, which is measured directly with the Racelogic box and gets influenced by the first order derivation of the slip angle β, due to equation (4.2). As the variables $\dot{\psi}$ and $\dot{\beta}$ are calculated in the simulation, $a_{y,meas}$ can be determined with low effort.

$$a_{y,meas} = v \cdot (\dot{\psi} + \dot{\beta}) \tag{4.2}$$

The measurement data for the model validation gets filtered with a FIR-Filter, as described in chapter 2.8. There filtering is only done for the offline model validation. The input data for the real time model on the Autobox is not filtered because the measurement noise is low and to avoid time delays due to the filtering.

4.1 Constant Radius

The constant radius driving maneuver is used to evaluate the steady state behavior of the vehicle and the vehicle model. During this maneuver, the vehicle gets driven on a circle with constant radius. The velocity is slowly increased in order to have a too high longitudinal acceleration. For this maneuver, the dynamic of the system can be neglected, and the equations (2.44) and (2.45) holds. As it can be seen in these equations, the wheel angle δ_{stat} has a big influence on this maneuver. Therefore, it is used to refine the look-up table for the rack angle to wheel angle relation of chapter 2.7.

In figure 4.1, the lateral acceleration and yaw rate of a constant radius maneuver is shown. This driving maneuver shows the main difference between the linear and the nonlinear vehicle model. The yaw rate follows the measured yaw rate up to a lateral acceleration between $4 - 5\,\mathrm{m/s^2}$. At higher lateral accelerations, the yaw rate calculated with the linear model increases very fast because of the expected linear tire behavior. In the range where the linear calculated yaw rate is much higher than the measured yaw rate, understeering can be detected very clearly. The yaw rate which is calculated with the nonlinear vehicle model follows the measured yaw rate up to a lateral acceleration of $10\,\mathrm{m/s^2}$. The main reason for this is the nonlinear tire model which is implemented and also the wheel load shift at this high lateral accelerations.

As it can be seen in figure 4.1, there remains a small error between the measured and the simulated nonlinear and linear yaw rate. This error arises from the simplifications which where done of the steering model with a look-up table. To compensate this error, the look-up table could be refined more, but this would result in a inferior result for other driving maneuvers. As the error is in an acceptable range, the rack to wheel angle look-up table was used as determined in chapter 2.7. Another reason for the error is the unsymmetrical design of the Roding. The Roding is generating a lower lateral acceleration and yaw rate in the left direction than in the right direction for the same steering input angle. This phenomena was detected just at the first driving tests with the Roding.

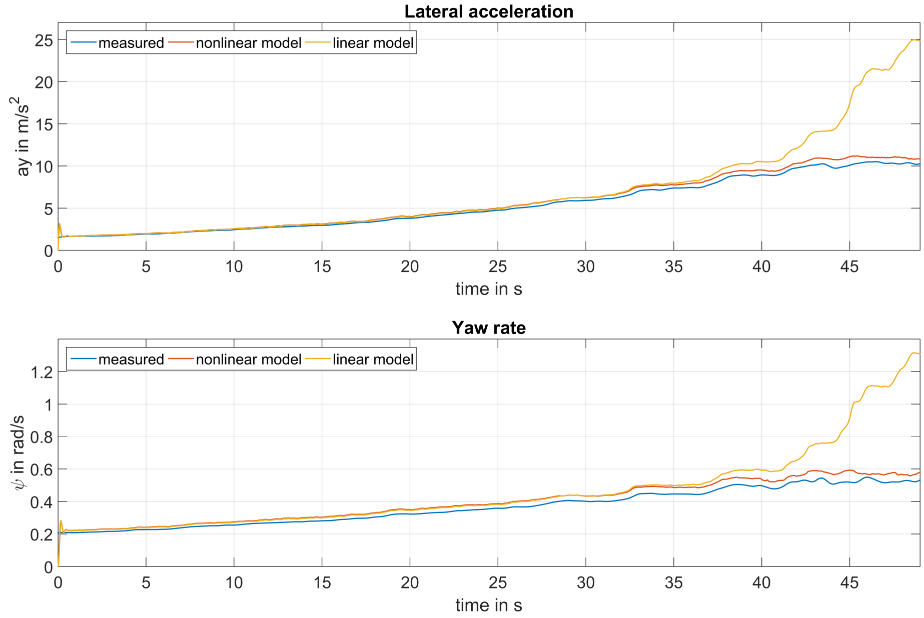

Figure 4.1: Constant radius of 18 m driving maneuver with slow increasing velocity

4.2 Sine input

To evaluate the dynamic behavior of the vehicle model, slalom maneuvers where done at different speeds with different maximum values of lateral acceleration. The main aspect of the simulation model is that it is well validated at dynamic maneuvers up to a lateral accelerations between $4 - 5\,\mathrm{m/s^2}$. Therefore, most of the slalom drives where done with this as a maximal lateral acceleration. Also, the frequency of the slalom maneuver has influence on the simulation result and has to be selected properly. Statistical investigations described in [18] have shown that a normal driver performs driving maneuvers with a steering frequency lower than 0.5 Hz. Therefore, also the selected frequency for the input steering angle is selected lower than this frequency. As the driving maneuvers were done by a person and not by a steering robot, the frequency varies, and the form of the input curve is not exactly a sinusoidal signal, but these deviations are not important for the model validation.

For the slalom maneuvers, the yaw inertia, determined in chapter 2.8, is an important parameter which has a strong influence on the phase shift between measured and simulated yaw inertia and lateral acceleration as well. The transient tire force behavior, described in chapter 3.4, determines the phase shift. As the time constant of the transient tire behavior is lower than 40 ms, which is small in relation to a maximal signal frequency of 0.5 Hz, the main view is directed on the yaw inertia.

The tire model can also be validated with the slalom maneuver and its parameter can be refined. For the optimization of the tire model, it has to be kept in mind that the different slalom maneuvers cover only a small ranges of slip angles. This makes it challenging, to optimize a tire model parameter because of the consequences to other maneuvers with differing slip angles. Due to that, a variation of the in chapter 3 determined tire model parameters has been done carefully. The best solution for the adjustment of the tire model was the introduction of a constant gain, to scale the tire force in a very small range between ±3 %.

In the following figures 4.2 to 4.5, different slalom maneuvers at different vehicle speeds are shown. Because the vehicle speed is an input of the model as well, it has to be validated at different vehicle speeds. The maneuvers where also done with different maximal lateral accelerations from $2\,\mathrm{m/s^2}$ to $10\,\mathrm{m/s^2}$.

In figure 4.2, a sine maneuver at a vehicle speed of 50 km/h and maximal lateral acceleration of $6\,\mathrm{m/s^2}$ is shown. The steering frequency lies about 0.3 Hz. As it can be seen, the accuracy of the simulation and the measurement is very high for the yaw rate and for the lateral acceleration. The relative error is lower than 3 %. In figure 4.2, it can also be seen that the difference between the linear and nonlinear model is low, which also applies in case of lateral accelerations of about $6\,\mathrm{m/s^2}$. This means that the vehicle has linear behavior in a long range.

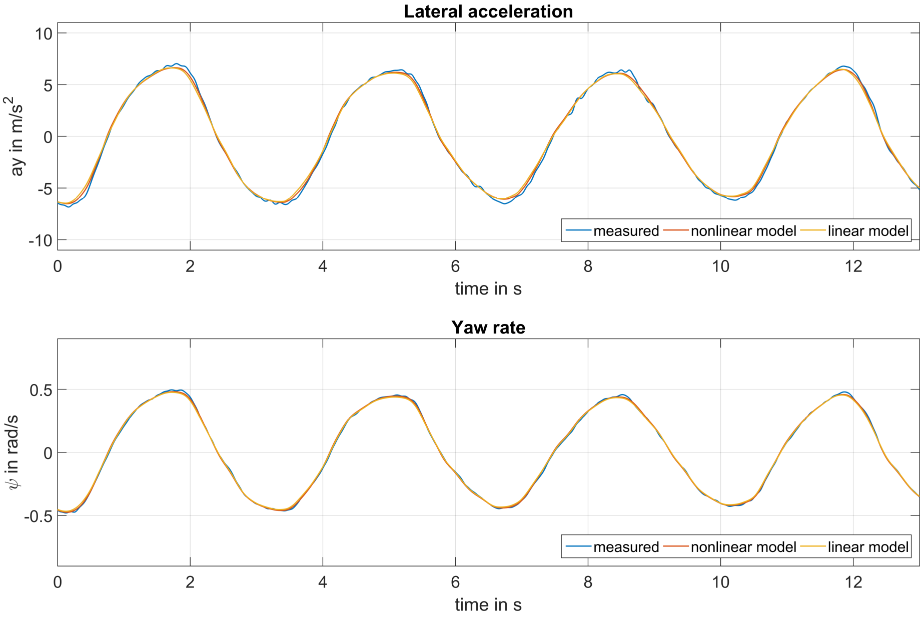

Figure 4.2: Sine input with a velocity of 50 km/h and maximal lateral acceleration of $6\,\mathrm{m/s^2}$.

In figure 4.3, the velocity of the vehicle gets increased to 60 km/h to evaluate the influence of the vehicle speed to the simulation result. The steering frequency and maximal lateral acceleration is not changed much. As it can be seen, the simulation result is again very good, and no clear differences between simulated and measured values are visible. Also the phase shift is very low.

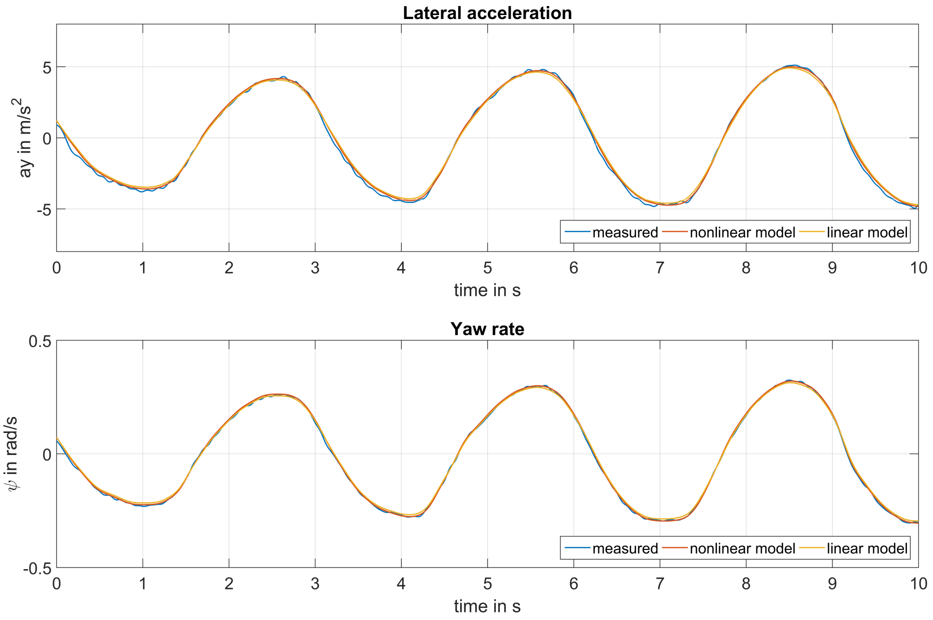

Figure 4.3: Sine input with a velocity of 60 km/h and maximal lateral acceleration of 5 m/s^2.

In figure 4.4 a sine maneuver with a velocity of 70 km/h and a maximal lateral acceleration of 2 m/s^2 are shown. This maneuver was done to evaluate the model behavior at lower lateral accelerations. Furthermore, you get a good result with this simulation. A small offset error between simulated and measured signals. This error happens because of an offset error of the Racelogic measurement box, which is corrected with a constant parameter. This offset error is not constant at all; therefore, it can not be completely prevented. This offset error is only visible during low accelerations and yaw rates and has no major importance.

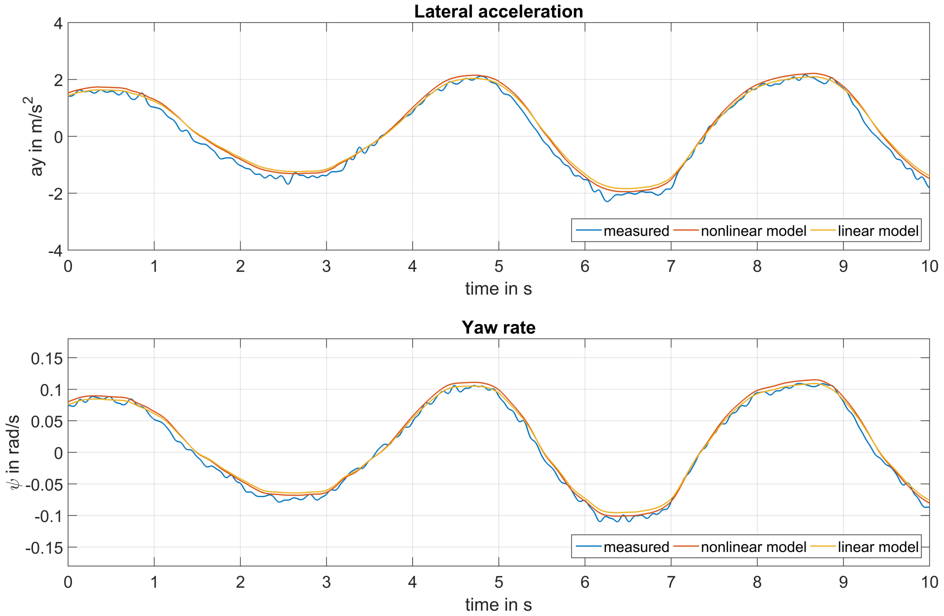

Figure 4.4: Sine input with a velocity of 70 km/h and maximal lateral acceleration of 2 m/s^2.

To evaluate the simulation result for maneuvers at the driving limits, a slalom maneuver with a velocity of 60 km/h is done. Figure 4.5 shows this slalom maneuver at a very high lateral acceleration up to 11 m/s^2, which a general driver should reach on normal driving. In this figure, the difference between the linear and nonlinear simulation model can be seen very clearly. The linear simulation model exceeds the measured values mostly on the maximum values of the lateral acceleration, whereas the nonlinear model shows a good behavior and follows the measured values. This behavior is to be expected because of the nonlinear tire model, which shows his affect almost in the range of tire slip angles higher than 3 °. In this range lies the maximum tire slip angle of this maneuver. But it can also seen that the accuracy of the nonlinear simulation model is not so high as in maneuvers with lower lateral accelerations. Reason therefore is the higher complexity of the vehicle behavior at the values of higher lateral accelerations. There are some more physical effects that take influence on the vehicle behavior, but they are not considered within this model.

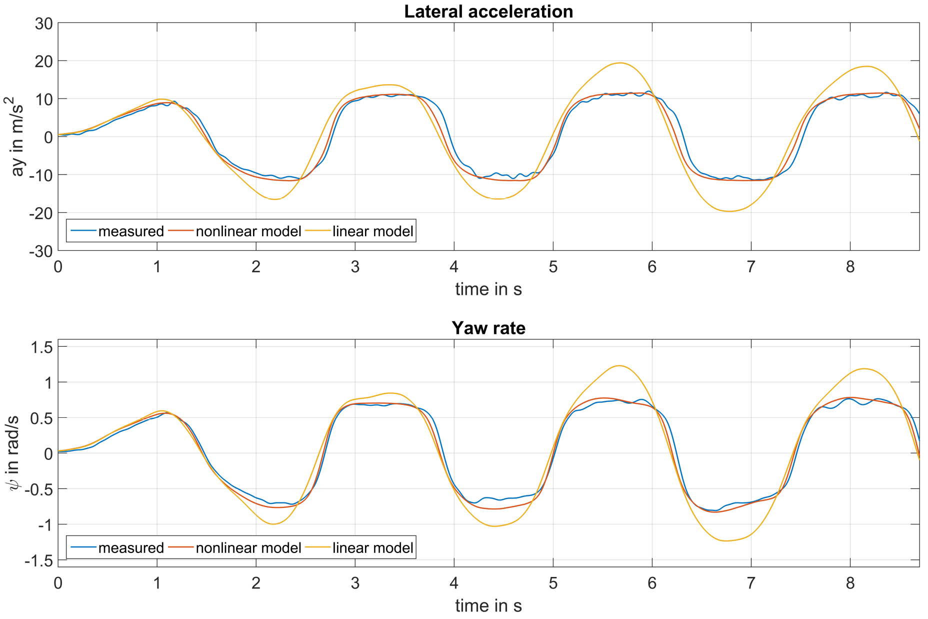

Figure 4.5: Sine input with a velocity of 60 km/h and maximal lateral acceleration of 10 m/s^2.

In figure 4.6 and 4.7, two frequency response maneuvers were done to evaluate the simulation result for different input frequencies. The maneuvers were done again at different vehicle speeds of 50 km/h and 70 km/h. The input frequency varies from 0.4 Hz to 4 Hz. As it can be seen in figure 4.6 and 4.7, the simulation result for the yaw rate is very accurate up to a frequency of 1 Hz. For higher frequencies, the damping of the model is higher than this of the real vehicle. Therefor, the difference of the measured and simulated yaw rate is clearly visible, but always in an acceptable range under 10 %. For the simulation result of the lateral acceleration, the error for frequencies higher than 1 Hz increases faster. The phase shift becomes clearly visible as well. As the simulation for the yaw rate works good for this measured frequency range, the model gets not refined more to increase the accuracy of the lateral acceleration simulation. The result for the simulation of the lateral acceleration is acceptable because the steering frequency range higher than 1 Hz is not reached in normal driving situations. The reason for the different damping of model and real vehicle could be the simplified dynamic tire load model, which considers no damping and spring influence on the vehicle body.

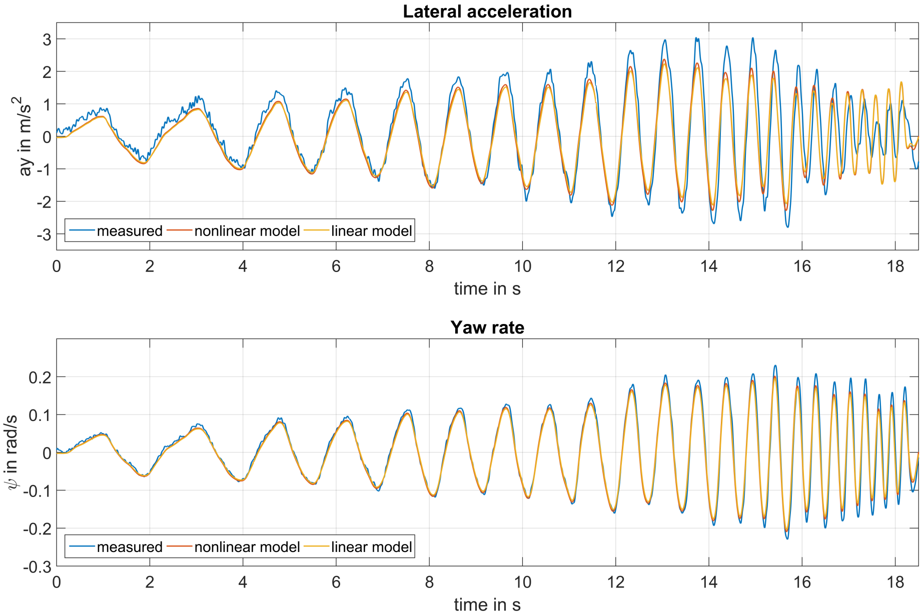

Figure 4.6: Frequency response at a velocity of 50 km/h.

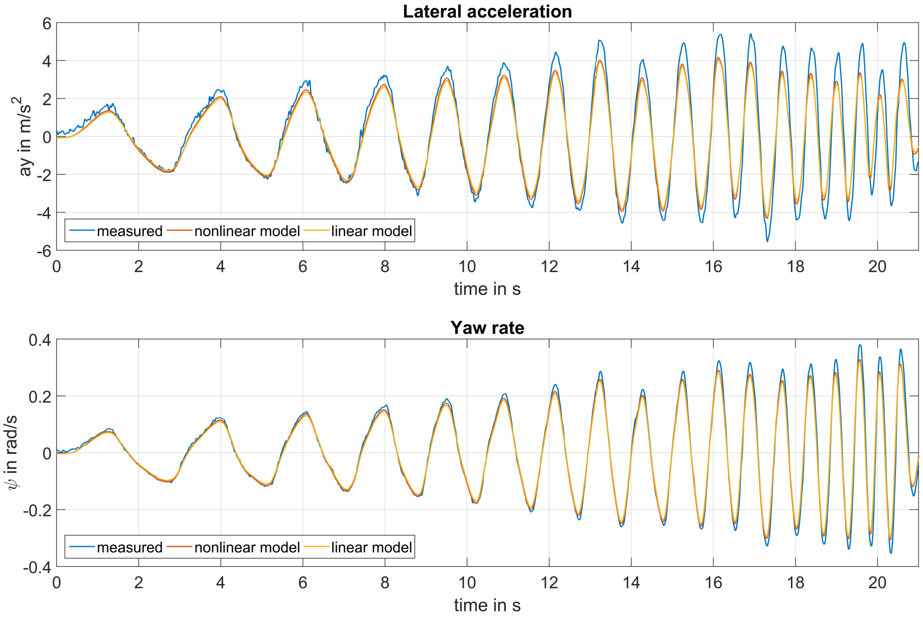

Figure 4.7: Frequency response at a velocity of 70 km/h.

4.3 Swept steer input

Figure 4.8 and figure 4.9 show a maneuver in which the steering wheel angle was slowly increased up to a point where the vehicle understeers. The steering wheel angle in both maneuvers was increased with different velocities. As it can see in figure 4.8 where the steering wheel angle was increased slowly, the yaw rate and the lateral acceleration follows the measured yaw rate very accurate. At this maneuver, the state variables reach their stationary value, because of the slow maneuver.

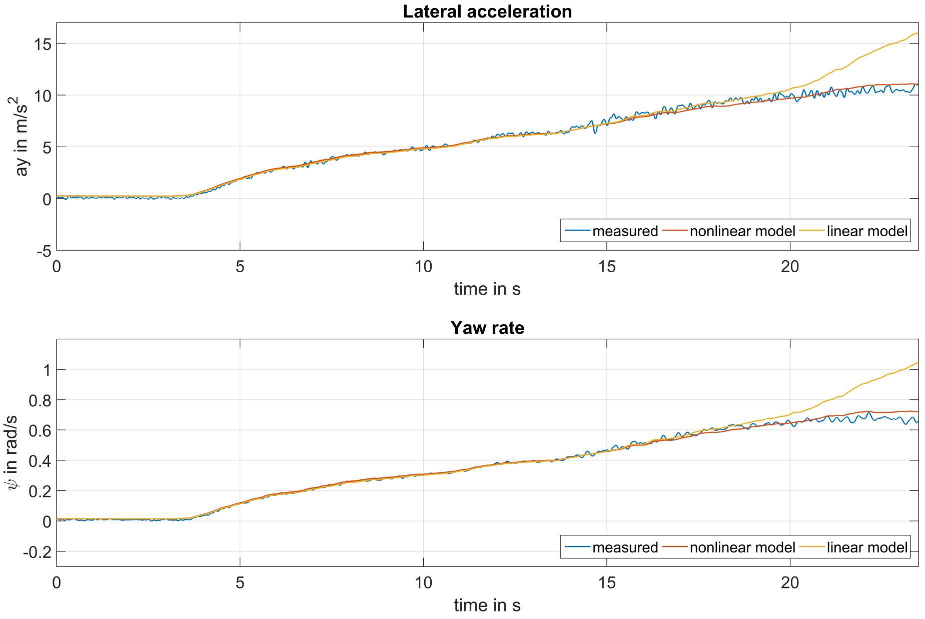

Figure 4.8: Swept steer input with a velocity of 60 km/h.

A difference to the stationary drive in figure 4.8 can be seen in figure 4.9. In this maneuver, steering angle was increased faster, so the state variables does not reach stationary values, and therefore the maneuver is more dynamic. This can be seen at the initial rise of the yaw rate: the model yaw rate rises faster than the measured yaw rate. Furthermore, a small phase shift can be seen, but the value of the phase shift is in the limits that allow to detect under- and oversteering.

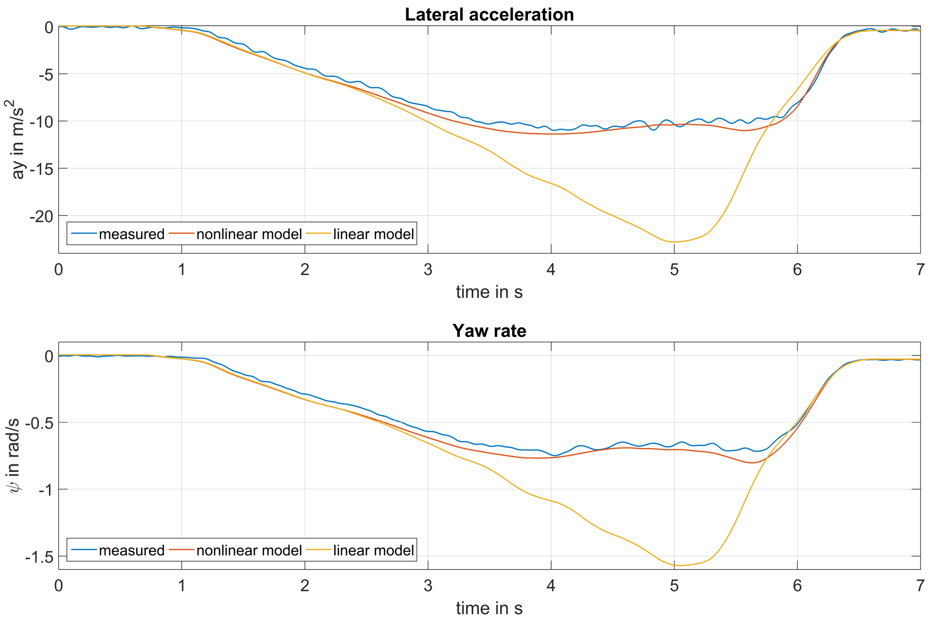

Figure 4.9: Swept steer input with a velocity of 40 km/h.

In the figures 4.8 and 4.9, the different behavior of the linear and nonlinear model on lateral accelerations higher than 6 m/s^2 can be seen. The linear yaw rate rises fast, whereas the nonlinear yaw rate follows the measured yaw rate very well. In this case, understeering can be detected.

4.4 Step input

Figure 4.10 shows a driving maneuver, in which step inputs were done in every direction. The maximum lateral acceleration is about 4 m/s^2. The simulation result is very accurate in comparison to the measured values. With the step input maneuver, the dynamic of the model can be analyzed very well. The dynamic at the point with the step from zero degrees of steering wheel angle to the final value shows a very good performance. The dynamic tire behavior, which has been considered with a first order low pass filter and a time constant in a range of $30 - 40$ ms, has the highest influence on this accuracy. Also, the overshoot can be reproduced and tuned with the time constant of this low pass filter.

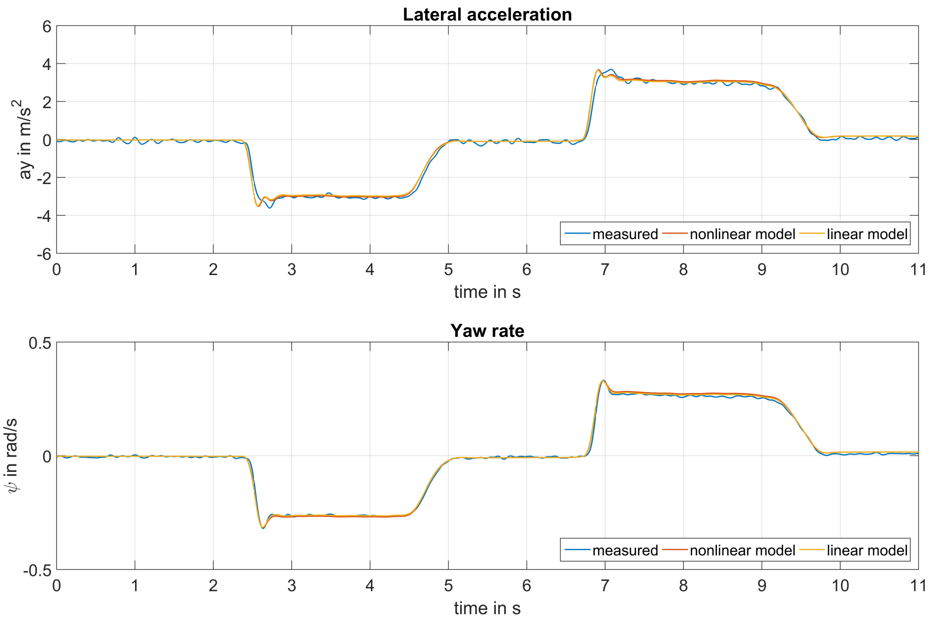

Figure 4.10: Step input with a velocity of 40 km/h and maximal lateral acceleration of 4 m/s^2.

4.5 Conclusion

As it was shown in this chapter, the performance and accuracy of the vehicle model simulation, for a wide range of different velocities and input frequencies is very good. The result is satisfying also because the model is kept simple. For a correct model validation, it is always better to have different measured signals to compare with the simulation. In this case it was the yaw rate and the lateral acceleration. The refining process of the model is always a compromise between the accuracy of the yaw rate and the accuracy of the lateral acceleration. As the main function of this model in the later use is the detection of under- and oversteering on the basis of the yaw rate, the primary task was to optimize the simulation result for the yaw rate.

5 Understeering/Oversteering detection

The real time vehicle model is mainly used for the detection of critical driving situations like under- and oversteering. A detection of critical situations in real time is very useful, primary for safety functions of a vehicle. For example, if an oversteering situation is detected, an active counter steering function can be implemented to stabilize the vehicle. But this is only one possible application for the under- and oversteering detection.

For the steer by wire vehicle, the generation of a correct steering wheel feedback is one of the most challenging parts. As at the steer by wire systems the mechanical connection between steering wheel and rack is not available, the steering feel has to be produced with a separate feedback actuator. One part of the feedback generation is the steering feel at critical driving situations. If for example the vehicle is driving on a surface with low friction coefficient and the vehicle understeers, the torque on the steering wheel has to be increased to generate a road feedback for the driver. Therefore, a correct detection of understeering is necessary.

5.1 Algorithm Structure

To detect under- and oversteering situations, the estimated yaw rate of the linear and nonlinear vehicle model is compared with the measured yaw rate. The difference between the measured and estimated yaw rate is calculated in detail. If this difference exceeds a constant threshold, under- and oversteering situations are detected.

For the understeering detection, the estimated linear yaw rate is used. Due to the expected linear tire behavior in the linear model, the estimated yaw rate rises linearly to the input steering angle. In reality, the adhesion limit of the tires is reached with lateral accelerations higher than $5\,\mathrm{m/s^2}$, and the vehicle yaw rate increases more slowly than the estimated yaw rate in untersteering situations. Therefore, a clear difference of the measured and estimated yaw rate is detectable, and a threshold can be set. The use of the estimated nonlinear yaw rate for the understeering detection is limited. Due to the nonlinear tire model implementation, the estimated nonlinear yaw rate follows the measured yaw rate in understeering situations as well, and the difference for the understeering detection is smaller.

On the other hand, the estimated nonlinear yaw rate is used for the oversteering detection. In this situation, the measured yaw rate increases faster than the estimated yaw rate, and again a threshold can be set at a certain value of the measured and estimated yaw rate. The use of the estimated nonlinear yaw rate was done because it follows the true yaw rate up to high lateral accelerations of about 10 m/s^2. If oversteering occurs in this situation, the measured yaw rate exceeds the estimated nonlinear yaw rate much faster than the estimated linear yaw rate. For this reason, oversteering can be detected very fast with the nonlinear vehicle model. For oversteering situations at lateral accelerations lower than 5 m/s^2, oversteering can be detected with the linear vehicle model too.

The under- and oversteering detection was implemented as a stateflow chart in Simulink. This implementation method provides a clear representation of different if- branches and the corresponding driving states.

For the understeering detection, the condition (5.1) has to be fulfilled. The threshold Us was set to 0.11 rad/s.

$$|\dot{\psi}_{lin}| - |\dot{\psi}_{meas}| > Us \tag{5.1}$$

For the oversteering detection, the condition (5.2) has to be fulfilled. The threshold Os was set to 0.06 rad/s.

$$|\dot{\psi}_{meas}| - |\dot{\psi}_{nonlin}| > Os \tag{5.2}$$

As the threshold for oversteering detection is too small to detect this situations very fast, some additional conditions where introduced to avoid wrong detections in case of model errors or measurement noise. Condition (5.3) guarantees an oversteering detection only for increasing yaw rates. Due to condition (5.4), oversteering is only detected when the measured and estimated yaw rate diverges.

$$\mathrm{sign}(\ddot{\psi}_{meas}) = \mathrm{sign}(\dot{\psi}_{meas}) \tag{5.3}$$

$$\mathrm{sign}(\ddot{\psi}_{meas}) = \mathrm{sign}(\ddot{\psi}_{nonlin}) \tag{5.4}$$

5.2 Algorithm validation

The determination of the different thresholds for the detection of critical driving situations was done on the normal asphalt surface within different under- and oversteering maneuvers.

The validation of the thresholds was done afterwords on surfaces with lower friction coefficients. These surfaces were wet asphalt, wet cobblestone and a wet ceramic surface.

In figure 5.1 an understeering maneuver on dry asphalt is shown. As it can be seen, the lateral acceleration during the understeering period is of about 10 m/s^2. The difference between the linear and the measured yaw rate is high in the understeering phase, and the understeering flag is set properly. In figure 5.1 it can also be seen that there is a difference between the nonlinear and the measured yaw rate during the untersteering period. This difference is much smaller than the one between the linear yaw rate and the measured yaw rate. The reason for the nonlinear model error is the higher complexity of the vehicle behavior on lateral accelerations of 10 m/s^2, which is not considered in this nonlinear vehicle model.

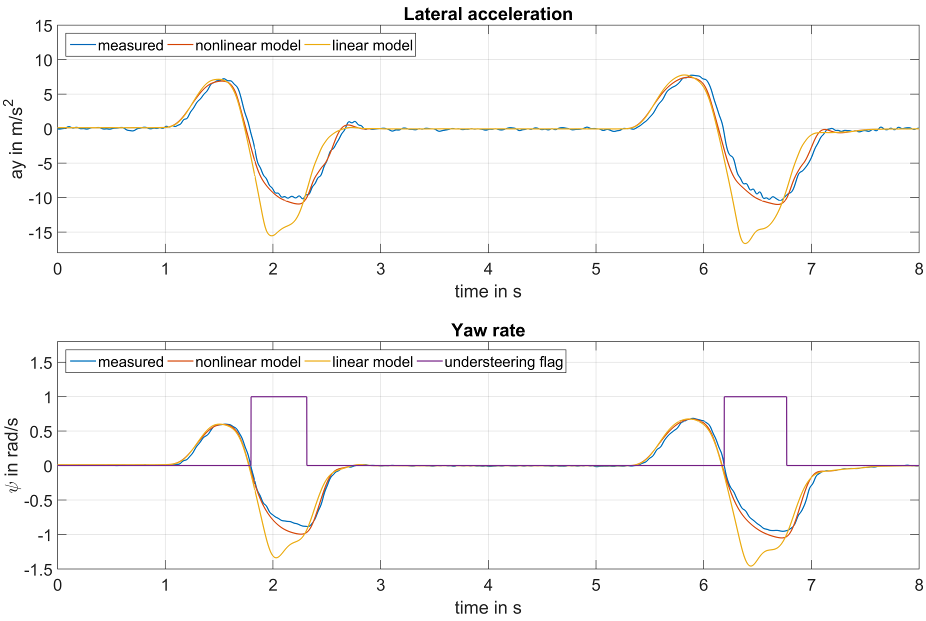

Figure 5.1: Understeering maneuver on dry asphalt.

In figure 5.2, an oversteering maneuver on dry asphalt was done. The oversteering was caused by an acceleration during the cornering. As the Roding Roadster is a rear wheel driven vehicle, it tends to oversteer on acceleration. In figure 5.2 it can be seen clearly how the measured yaw rate drifts away from the estimated yaw rate. Oversteering can be detected very fast, at about 200 ms before the driver is able to react and countersteer. As it can be seen, an oversteering detection is possible also with the linear vehicle model, but this would work not as fast as with the nonlinear model.

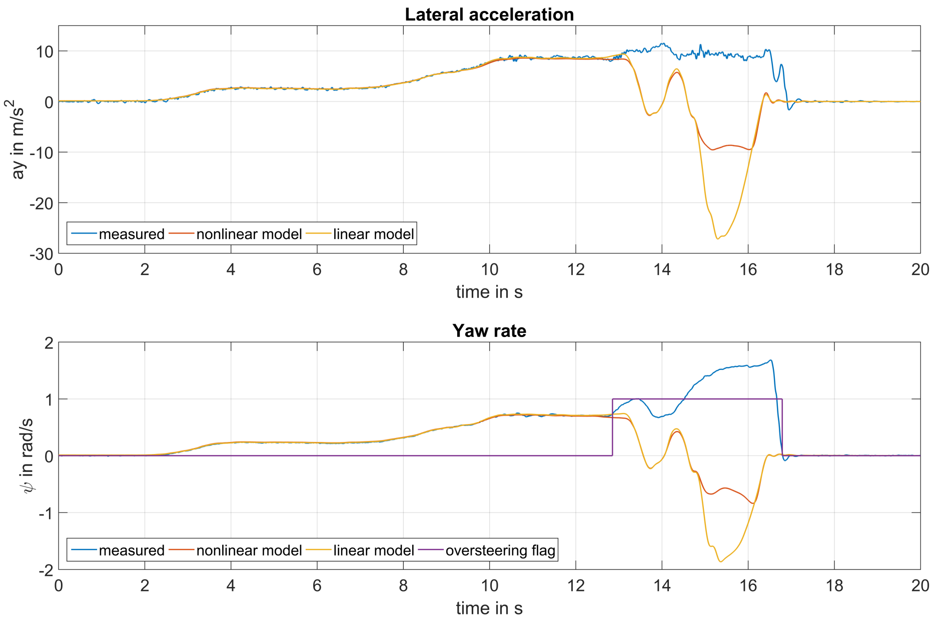

Figure 5.2: Oversteering maneuver on dry asphalt.

To validate the refined thresholds of the under- and oversteering detection, different additional maneuvers were done on wet asphalt. At these conditions, under- and oversteering can be done very easily because the friction coefficient on wet asphalt is lower than on dry one. The validation was done in real time with the dSpace software. On the software layout, the under- and oversteering flag were implemented with a blinking light to have an indication when the flags were set. The thresholds were refined in consideration of the subjective under- and oversteering feeling of the driver and assistant driver.

In figure 5.3, an understeering maneuver, done within a step inputs to the left and right direction, is shown. It can be seen that the linear yaw rate increases fast and exceeds the measured yaw rate. The understeering flag is set and reset correctly in the right time span. Furthermore, there is also a difference between the nonlinear model yaw rate and the measured yaw rate in the understeering phase. This occurs because of the reduced friction coefficient of wet asphalt, which is not considered in the vehicle model.

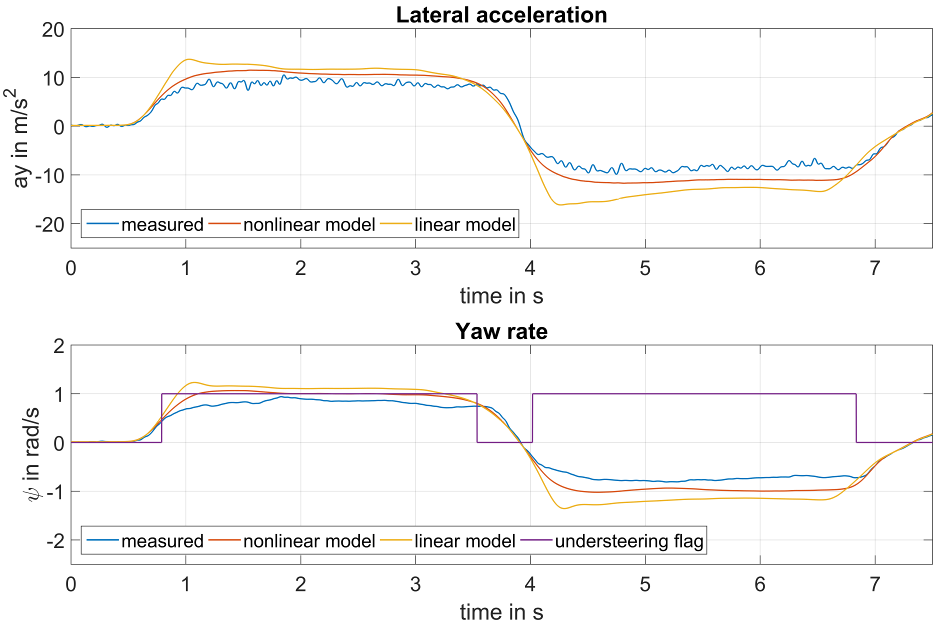

Figure 5.3: Understeering maneuver on wet asphalt.

In figure 5.4, an oversteering maneuver is shown. The oversteering situation was performed with a steering wheel input in combination with an increasing longitudinal acceleration. As it can be seen in figure 5.4, the situation is clearly identified and the oversteering flag is set. In this case, also the linear model yaw rate would work for the oversteering detection because the lateral acceleration is lower than $6\,\mathrm{m/s^2}$.

To validate the algorithm for a more complex driving situation too, a maneuver was performed on different surfaces. In detail, a surface change during cornering is performed. The cornering is started on a wet ceramic surface with a very low friction coefficient. In this situation, the vehicle understeers because the front wheels have too low adhesion. During the cornering maneuver, the surface is changed to wet asphalt, which has a higher friction coefficient than wet ceramic. The adhesion of the front wheels increases abruptly, and the rear end of the vehicle skids: the vehicle starts to oversteer. In figure 5.5, the yaw rate, the lateral acceleration for the described maneuver and the under- and oversteering flags are shown. As it can be seen, the flags are set in the correct order and time span.

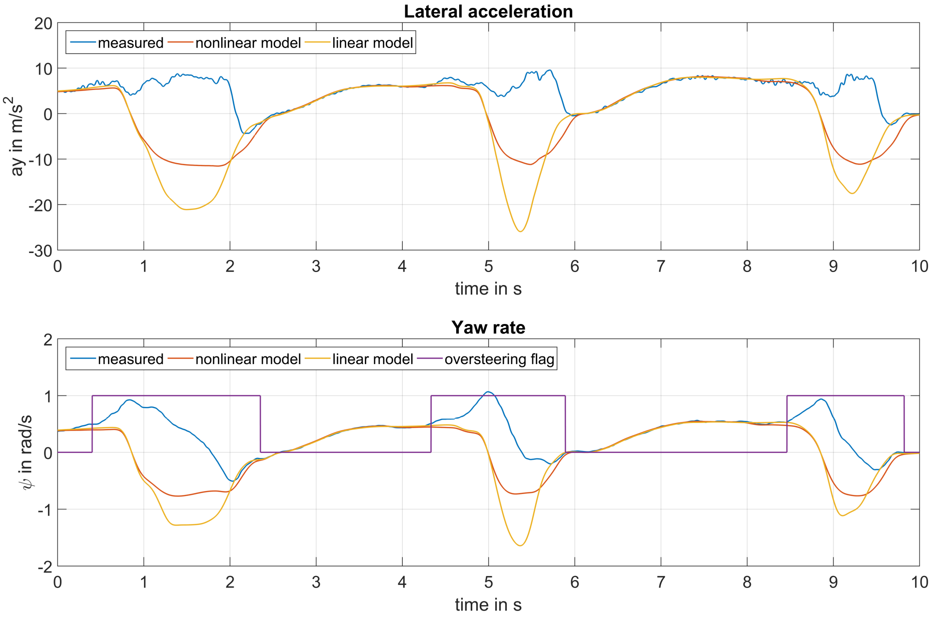

Figure 5.4: Oversteering maneuver on wet asphalt.

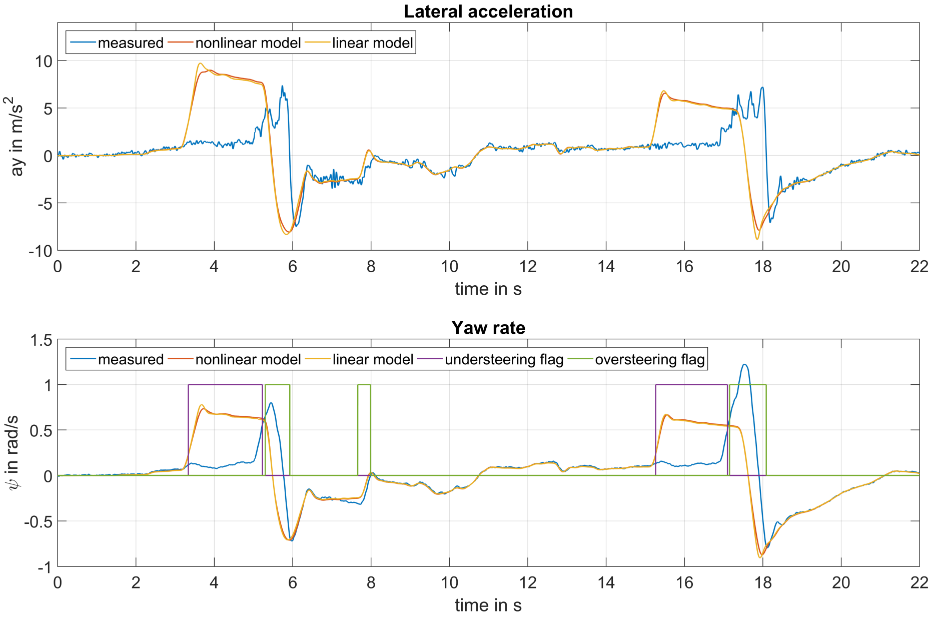

Figure 5.5: Driving maneuver on different surfaces.

6 Conclusion and next steps

As indicated in the previous chapter, the generation and validation of a vehicle model is a complex process. In chapter 2, a detailed derivation of a linear and nonlinear single track model is described. Additional model extensions like the dynamic wheel load chapter 2.5 and the steering model chapter 2.6 are described. Also the parameter identification chapter 2.8 and the implementation environment chapter 2.9 is described. After this theoretical description, a first model implementation was done in Matlab/Simulink. The result was compared with available measurement data of the Roding to have a first overview of the simulation result accuracy.

The second part of the master thesis is the tire measurement and tire model generation described in chapter 3. In this chapter, a detailed description of the measurement process with the appeared problems is described. Also, a theoretical insight to different tire models is given in chapter 3.5. The final generated tire model in chapter 3.6 was validated with the tire data of different wheel loads. The resulting model gives a good accuracy for this use case, but can be refined with a more complex tire model. A longitudinal tire model was generated for further work, to extend the vehicle model with a simulation of the longitudinal vehicle characteristic.

The vehicle model was extended with the nonlinear tire model. After this, the model implementation was ready for a first test on the dSpace Autobox under real driving conditions. The driving tests have been done on a special test track in Spain. During these test weeks, different driving maneuvers were performed, and the vehicle model was refined step by step. The model validation process is described in chapter 4. The whole validation process is very complex in view of the high number of different parameters, which have influence on the model behavior. The challenge is to generate a vehicle model which estimates an accurate yaw rate as well as an accurate lateral acceleration. The outcome of the simulation and validation process was a very accurate model, which works good in different driving maneuvers.

The main use case for this vehicle model was to be an extension to a correct detection of critical driving situations. This algorithm is describe in chapter 5. The detection was implemented with constant thresholds, which have to be found out in different driving maneuvers. The validation of the algorithm in chapter 5.2 shows very good results and a correct detection of under- and oversteering.

The vehicle model and the corresponding under- and oversteering detection is used for a correct adaption of the steering feel in critical situations. The implementation of this steering feel adaption is already implemented and tested. It shows good results and it is robust enough for different driving situations.

The further area of application for the vehicle model is very wide. A use for the estimation of the rack force is in plan. Another application could be the use of the vehicle model estimation for an active steering angle correction to support the driver in critical driving situations. Therefore, the implemented under- and oversteering detection can be very helpful.

The work on the vehicle model is not finished with this master thesis. The model can be refined with different extensions. An important extension is the implementation of a longitudinal vehicle model. As the problems with the wheel angle sensors of the test vehicle, that occurred during these thesis, are solved already, and a base for the longitudinal tire force model is provided within this work, this extension should be implementable with less effort. Another extension is a more detailed model of the steering system, which should improve the model accuracy for certain driving situations like cornering at lower speeds with a large steering input. The model for the dynamic wheel load shift can also be reworked and extended with the kinematics of spring and damper system. This should increase the model accuracy at lateral accelerations higher than $5\,\mathrm{m/s^2}$.

In conclusion, the accuracy and robustness of the developed vehicle model in this master thesis is high. In spite of the different simplifications in the derivation of the vehicle model equations, the simulation provides good results which were confirmed trough different driving maneuvers.

List of Figures

1.1 Roding Roadster prototype vehicle. 4

2.1 DIN 70000 coordinate system [13] 5
2.2 SAE J670e coordinate system [13] 5
2.3 ISO 8855 tire fixed coordinate system [13] 6
2.4 Figure with drawn vector orientation from [12] 10
2.5 Schematic depiction of lateral tire characteristic from [12]. 12
2.6 Vectors for the calculation of the front wheel force from [12]. 13
2.7 Graphical description of vehicle steering tendency from [12]. 17
2.8 Calculated and measured wheel angle to lateral acceleration on a constant radius drive with a radius of 36 m. 18
2.9 Linear roll model with forces and moments [5]. 23
2.10 Comparison of lateral acceleration and yaw rate between simulation with and without dynamic wheel load model. 25
2.11 Depiction of Ackermann Steering geometry of [18]. 27
2.12 Figure of wheel angle measurement benchmark. 28
2.13 Measured wheel angle over Rack angle. 29
2.14 Steering difference angle. 30
2.15 Filtred and raw sensor signal of yaw rate sensor. 32

3.1 Mobile Tire Testing Laboratory 36
3.2 Detailed view of the mobile measurement testbench with descriptions . . 37
3.3 Cutting of the frequency domain plot of the measured wheel load F_z. . . . 41
3.4 Frequency response of FIR-Filter. 42
3.5 Raw- and filtered signal of lateral tire force F_y. 43
3.6 Wheel load F_z over slip angle α. 44
3.7 Lateral tire force F_y over slip angle α. 45
3.8 Lateral tire force F_y of different measurements and average value over slip angle α. 46
3.9 Lateral tire force F_y of the front tires at different wheel loads F_z. 47
3.10 Lateral tire force F_y of the rear tires at different wheel loads F_z 48
3.11 Lateral friction coefficient $\mu(\alpha)$ of the front tire. 49
3.12 Lateral tire characteristic for different camber settings of the front tires. . 50
3.13 Lateral tire characteristic for different camber settings of the rear tires. . 51
3.14 Longitudinal tire characteristic for different camber settings. 53
3.15 Longitudinal tire characteristic for different camber settings. 53
3.16 Comparison of yaw rate with transient and static tire force behavior. . . . 55

3.17 Graphical description of Magic Formula equation parameters from [16]. . 58
3.18 Graphical description of TM-Simple equation parameters. 60
3.19 Principle depiction of traction circel from [12]. 61
3.20 Comparison of TM-Simple model with real tire measurement data of front tire. 64
3.21 Comparison of TM-Simple model with real tire measurement data of rear tire. 65

4.1 Constant radius of 18 m driving maneuver with slow increasing velocity . 69
4.2 Sine input with a velocity of 50 km/h and maximal lateral acceleration of 6 $\mathrm{m/s^2}$. 70
4.3 Sine input with a velocity of 60 km/h and maximal lateral acceleration of 5 $\mathrm{m/s^2}$. 71
4.4 Sine input with a velocity of 70 km/h and maximal lateral acceleration of 2 $\mathrm{m/s^2}$. 72
4.5 Sine input with a velocity of 60 km/h and maximal lateral acceleration of 10 $\mathrm{m/s^2}$. 73
4.6 Frequency response at a velocity of 50 km/h. 74
4.7 Frequency response at a velocity of 70 km/h. 74
4.8 Swept steer input with a velocity of 60 km/h. 75
4.9 Swept steer input with a velocity of 40 km/h. 76
4.10 Step input with a velocity of 40 km/h and maximal lateral acceleration of 4 $\mathrm{m/s^2}$. 77

5.1 Understeering maneuver on dry asphalt. 81
5.2 Oversteering maneuver on dry asphalt. 82
5.3 Understeering maneuver on wet asphalt. 83
5.4 Oversteering maneuver on wet asphalt. 84
5.5 Driving maneuver on different surfaces. 84

List of Tables

2.1 Geometrical steering dimensions. 29
2.2 Vehicle parameters. 31
2.3 Identified yaw inertia for different velocities. 33

3.1 tire measurement plan for tire 225/40ZR18. 39
3.2 tire measurement plan for tire 265/35ZR18. 39
3.3 Tire Model Parameters. 63

Bibliography

[1] ThyssenKrupp Presta AG. URL: `http://www.thyssenkrupp-presta.com/de/produkte/produkte.php` (visited on 11/12/2015).

[2] J.R. Buck A.V. Oppenheim R.W. Schafer. *Discrete-Time Signal Processing.* 2. Edition. Prentice-Hall, 1999. ISBN: 978-0137549207.

[3] I.J.M. BESSELINK. "Shimmy of Aircraft Main Landing Gears". Dissertation. Universityof Technology Delft, Netherlands, 2000.

[4] F. BÖHM. "Zur Mechanik des Luftreifens". Habilitation. Technische Hochschule Stuttgart, 1966.

[5] M.Hiller D. Schramm and R. Bardini. *Modellbildung und Simulation der Dynamik von Kraftfahrzeugen.* 1. Edition. Springer-Verlag, 2010. ISBN: 978-3-540-89313-4.

[6] dSpace. URL: `https://www.dspace.com/de/gmb/home/products/hw/modular_hardware_introduction/processor_boards/ds1005.cfm` (visited on 11/12/2015).

[7] William F. and Douglas L. Milliken. *Race Car Vehicle Dynamics.* 2. Edition. SAE International, 1995. ISBN: 978-1560915263.

[8] W. Garrott G. Heydinger R. Bixel and M. Pyne. *Measured vehicle inertial parameters-NHTSA's data through november 1998.* SAE International, 1999.

[9] Karl L. Haken. *Grundlagen der Kraftfahrzeugtechnik.* 4. Edition. Hanser, 2015. ISBN: 978-3-446-44216-0.

[10] C. Halfmann and H. Holzmann. *Adaptive Modelle für die Kraftfahrzeugdynamik.* 1. Edition. Springer, 2003. ISBN: 978-3-540-44278-3.

[11] W. Hirschberg. *TM_simple: A Simple to Use Tyre Model.* Technische Universität Graz. Mar 13, 2009.

[12] W. Hirschberg and H. M. Waser. *Lecture notes on: Fahrdynamik.* Institute of Automotive engineering, Graz university of technology, 2014.

[13] W. Hirschberg and H. M. Waser. *Lecture notes on: Kraftfahrzeugtechnik.* Institute of Automotive engineering, Graz university of technology, 2012.

[14] R. Isermann. *Fahrdynamik-Regelung.* 1. Edition. Vieweg, 2006. ISBN: 978-3-8348-0109-8.

[15] M. Mitschke and H. Wallentowitz. *Dynamik der Kraftfahrzeuge.* 4. Edition. Springer, 2004. ISBN: 3-540-42011-8.

[16] Hans B. Pacejka. *Tyre and Vehicle Dynamics.* 3. Edition. Butterworth-Heinemann, 2006. ISBN: 978-0-08-097016-5.

[17] H.B PACEJKA. “The wheel shimmy phenomenon - a theoretical and experimental investigation with particular reference to the nonlinear problem”. Dissertation. Delft University of Technology, December 1966.

[18] P. Pfeffer and M. Harrer. *Lenkungshandbuch.* 1. Edition. Springer-Verlag, 2011. ISBN: 978-3-8348-0751-9.

[19] Georg Rill. *FIRST ORDER TIRE DYNAMICS.* III European Conference on Computational Mechanics, Lisbon,Portugal. 2006.

[20] EINSLE S. and ENG M. “Analyse und Modellierung des Reifenübertragungsverhaltens bei transienten und extremen Fahrmanövern”. Dissertation. Technische Universität Dresden, December 2010.

[21] B. VON SCHLIPPE and R. DIETRICH. “Das Flattern eines bepneuten Rades”. In: *Bericht 140 der Lilienthal Gesellschaft für Luftfahrtforschung pp. 35-45, 63.66* (1941.).

[22] B. VON SCHLIPPE and R. DIETRICH. *Zur Mechanik des Luftreifens.* Tech. rep. Zentrale für wissenschaftliches Berichtwesen der Luftfahrtforschung des Generalluftfahrzeugmeisters(ZBW), Berlin Adlershof, 1942.

[23] L. Segel. “Force and Moment Response of Pneumatic Tires to Lateral Motion Inputs”. In: *ASME* (1966), pp. 37–44.